THE FACULTY OF ENGINEERING AND THE BUILT ENVIRONMENT
The Department of Mechanical Engineering

Numerical Investigation of the Convective Heat Transfer Coefficient of the Human Body Using a Representative Cylindrical Model

Prepared By: Daniel Eferemo Jr.

June 2017

A dissertation submitted to the Department of Mechanical Engineering, University of Cape Town in partial fulfilment of the requirements for the degree of Master of Science in Mechanical Engineering

Declaration

I, Daniel Eferemo know the meaning of plagiarism and declare that all the work in the document, save for that which is properly acknowledged, is my own. This thesis/dissertation has been submitted to the Turnitin module, and I confirm that my supervisor has seen my report and any concerns revealed by such have been resolved with my supervisor.

signature removed

Daniel Eferemo

Student Number: EFRDAN001

Date: 29th June 2017

ABSTRACT

Title:	Numerical Investigation of the Convective Heat Transfer Coefficient of a Human Body Using a Representative Cylindrical Model
Author:	Daniel Eferemo Jr. (EFRDAN001)
Supervisor:	Prof. Tunde Bello-Ochende
Co-Supervisor:	Prof. Arnaud Malan
University:	University of Cape Town
Department:	Mechanical Engineering
Degree:	Masters of Science in Mechanical Engineering (M.Sc. Mech. Eng.)

The principal objective of this study is to investigate, develop and verify a framework for determining the convective heat transfer co-efficient from a cylindrical model that can easily be adaptable to more complex geometry – more specifically the human body geometry. Analysis of the model under forced convection airflow conditions between the transition velocity of about 1m/s - calculated using the Reynolds number - up until 12m/s were carried out. The boundary condition, however, also included differences in turbulence intensities and cylinder orientation with respect to wind flow (seen as wind direction in some texts). A total of 90 Computational Fluid Dynamic (CFD) calculations from these variations were analysed for the model under forced convective flow. Similar analysis were carried out for the model under natural convection with air flow velocity of 0.1m/s. Here, the temperature difference between the model and its surrounding environments and the cylinder orientation with respect to wind flow were varied to allow for a total of 15 CFD analysis. From these analysis, for forced convection, strong dependence of the convective heat transfer coefficient on air velocity, cylinder orientation and turbulence intensity was confirmed. For natural convection, a dependence on the cylinder orientation and temperature difference between the model and its environment was confirmed. The results from the CFD simulations were then compared with those found in texts from literature. Formulas for the convective heat transfer coefficient for both forced and natural convection considering the respective dependent variables are also proposed. The resulting formulas and the step by step CFD process

described in this thesis provides a framework for the computation of the convective heat transfer coefficient of the human body via computer aided simulations.

This framework can easily be adaptable to the convective heat transfer coefficient calculations of the human body with some geometric modelling adjustments, thus resulting in similar representative equations for a human geometric model.

Keywords: Turbulent flow, laminar flow, computational fluid dynamics, computer simulated person.

ACKNOWLEDGEMENTS

Acknowledgement and thanks are given to my supervisor Prof. Tunde Bello-Ochende for suggesting the research area for this paper as well as his guidance and continuous encouragements throughout this project.

My sincere gratitude is expressed to my co-supervisor Prof. Arnaud Malan for his technical support especially through the theoretical introductions by means of workshops organized to help build a solid theoretical foundation for the computational fluid dynamics principles used in this paper.

Daniel Eferemo Jr.
2017

TABLE OF CONTENTS

Abstract ii

Acknowledgements iv

Table of Contents v

List of Figures ix

List of Tables xiii

Nomenclature xiv

1 Introduction 1

1.1 Background 1

1.2 Convection Heat Exchange Mechanism Overview 2

1.3 Dissertation Organization 3

2 Literature Review 5

2.1 Factors affecting the convective heat transfer coefficient of the human body 5

2.1.1 Convective heat transfer area of the human body 5

2.1.2 Posture 7

2.1.3 Effect of Body Motion 8

2.1.4 Wind speed 9

2.1.5 Wind direction 12

2.1.6 Temperature Gradient between the Body and the Environment 12

2.1.7 Effect of Radiative Heat Loss 14

2.2 Possible experimental approaches to determining the convective heat transfer coefficient of the human body 16

2.2.1 Use of heat flux sensors on the surface of the body/simple heat–emitting devices 16

2.2.2 Naphthalene Sublimation Technique 18

2.2.3 Technique of Heat Balance Investigation of the Human Body 20

2.2.4 Use of Thermal Manikins 24

2.2.5 Numerical Simulations 27

2.3 Problem Statement 28

2.4 Objective of the work in this paper 29

2.5 Scope and Focus of Study 30

3 Research Theory 31

3.1 Numerical Modelling 31

3.2 Numerical Modelling Procedure 32

3.2.1 Creation of Geometrical Models and Computational Domain 33

3.2.2 MESH Generation 33

3.2.3 Solution and Post-Processing 37

3.3 Governing Equations 37

3.3.1 Conservation of Mass 37

3.3.2 Conservation of Momentum 38

3.3.3 Energy EQuation 39

3.4 Finite Volume Method (FVM) 40

3.5 Pressure – Velocity Coupling 40

3.6 Modelling of Fluid Flow and Heat Transfer 42

3.7 Boundary Conditions 45

3.7.1 Inlet Boundary Conditions 45

3.7.2 Near wall treatment 45

3.7.3 Outflow Boundary Conditions 47
3.8 Mesh generator Analysis 48
3.8.1 The Diffusive Term 49
3.8.2 The Convective Term 50
4 Mesh Generator Analysis Report and Discussion 53
4.1 First Order Upwinding 53
4.1.1 Equispaced mesh 53
4.1.2 Stretched Mesh 56
4.1.3 Mesh Independence Study 59
4.1.4 Closure – First Order Upwind 61
4.2 Higher Order Upwinding 62
4.2.1 Equispaced mesh 62
4.2.2 Stretched Mesh 65
4.2.3 Mesh Independence Study 68
4.2.4 Closure – Higher Order Upwind 73
4.3 Decision of Upwinding Scheme 74
5 Numerical Simulation Methodology 75
5.1 Cylindrical Model and CFD Domain 75
5.2 Meshing the 3D Model 77
5.3 Numerical and Boundary Layer Conditions 78
5.4 Radiative heat flux analysis 79
5.5 Convective heat transfer coefficients analysis 80
6 Results and Discussions 81
6.1 Flow Field 81
6.2 Representative time plot 83

6.3 Results and Effects of Wind Velocity on $\boldsymbol{hconv}$ 84

6.4 Result and Effects of Turbulence Intensity on $\boldsymbol{hconv}$ 88

6.5 Proposed formula for determining the convective heat transfer coefficient as a function of wind velocity for turbulent flow 89

6.6 Results Validation for Turbulent Flow 91

6.7 Analysis of $\boldsymbol{hconv}$ of the Cylinder for Natural Convection 92

6.7.1 Effects of Temperature Difference on $\boldsymbol{hconv}$ for laminar flow 94

6.8 Proposed formula for determining the convective heat transfer coefficient as a function of wind velocity for laminar flow 97

6.9 Numerical Accuracy Assessment 100

7 Summary, Conclusion and Suggestions 102

7.1 Summary 102

7.2 Conclusion 103

7.3 Suggestions for Future Work 104

8 References 106

9 Appendix A0 – Convection Equation Descritization 109

10 Appendix A1 – MATLAB Code used for First Order Upwinding 112

11 Appendix A2 – MATLAB Code used for Higher Order Upwinding 123

12 Appendix B1 – Results of CFD Simulations for the Upright Cylinder – Turbulent Flow 129

13 Appendix B2 – Results of CFD Simulations for the Inclined Cylinder (45 degree to the vertical) – Turbulent Flow 131

14 Appendix B3 – Results of CFD Simulations for the Supine Cylinder – Turbulent Flow .. 133

15 Appendix C1 – Results of CFD Simulations for Laminar Flow 135

16 Ethics Form 136

LIST OF FIGURES

Figure 2.1 Heat transfer area ratios for calculating heat transfer coefficients (Kurazumi *et al*., 2008a) 7

Figure 2.2: Natural convective heat transfer coefficients for the nude thermal manikin in still air (V <0.10m/s) (de Dear *et al*., 1997) 11

Figure 2.3: Heat transfer area ratios for calculating heat transfer coefficients (Kurazumi *et al*., 2008a) 16

Figure 2.4: Calorimeter plates setup on the human head of one of the subjects for the experiment. (Clark & Toy, 1975) 17

Figure 2.5: Schematic diagram of a human model showing the locations of the naphthalene disk on the manikin (Chang, Arens & Gonzalez, 1998) 19

Figure 2.6: Locations of individual areas over the body surface which were tested and the division of the skin surface for weighting. (Hardy & Dubois, 1937) 21

Figure 2.7: Fields (body regions) used for air movements and skin temperature observations (Winslow, Herrington & Gagge, 1936) 23

Figure 2.8: Manikins segmentation and respective surface area, and illustration of postures investigated in study (de Dear *et al*., 1997) 25

Figure 2.9: Analytical domain with CSP as described in works of Cong Li *et al*. (Cong & Kazuhide, 2012) 27

Figure 3.1 Numerical Modelling Procedure using the ANSYS Software package 33

Figure 3.2: 3D Cell Types for Meshing (Ansys, 2009) 34

Figure 3.3: Smooth Transition Inflation 35

Figure 3.4: First Layer Thickness Inflation 35

Figure 3.5: Total Thickness Inflation 36

Figure 3.6: First Aspect Ratio Inflation....36

Figure 3.7: Last Aspect Ratio Inflation....37

Figure 3.8 The Simple Algorithm....41

Figure 3.9: Transport equation of the SST $\boldsymbol{k-\omega}$ model (Versteeg & Malalasekera, 2007)...44

Figure 3.10: Subdivision of Near Wall Region (ANSYS, 2003)....46

Figure 3.11: Depiction of Near Wall Treatments in Ansys (ANSYS, 2003)....47

Figure 3.12: Describing the tube split into N nodes with a stretching factor ß....49

Figure 3.13: Describing the tube split for higher order discretisation....51

Figure 4.1: Temperature Distribution along Pipe (N = 10, equi-spaced)....54

Figure 4.2: Temperature Distribution along Pipe (N = 100, equi-spaced)....54

Figure 4.3: Temperature Distribution along Pipe (N = 1000, equi-spaced)....55

Figure 4.4: Error Analysis (equi-spaced, N = 1000)....55

Figure 4.5: Temperature Distribution along Pipe (N = 10, stretched)....57

Figure 4.6: Temperature Distribution along Pipe (N = 50, stretched)....57

Figure 4.7: Temperature Distribution along Pipe (N = 100, stretched)....58

Figure 4.8: Error Analysis (stretched, N = 100)....58

Figure 4.9: Mesh Dependence Plot Equi-Spaced Mesh....59

Figure 4.10: Mesh Dependence Plot, Stretched Mesh....61

Figure 4.11: Showing slope of log-log graph of Error vs. Mesh spacing for low and high number of nodes....61

Figure 4.12: Temperature Distribution along Pipe (N = 7, ß = 1, kappa = 1/2)....63

Figure 4.13: Temperature Distribution along Pipe (N = 15, ß = 1, kappa = 1/2)....63

Figure 4.14: Temperature Distribution along Pipe (N = 6, ß = 1, kappa = 1/3)....64

Figure 4.15: Temperature Distribution along Pipe (N = 10, ß = 1, kappa = 1/3)....64

Figure 4.16: Error Analysis (equi-spaced, N = 10, kappa = 1/3)....65

Figure 4.17: Temperature Distribution along Pipe (N = 7, ß = 0.85, kappa = 1/2) 66

Figure 4.18: Temperature Distribution along Pipe (N = 6, ß = 0.85, kappa = 1/3) 67

Figure 4.19: Error Analysis (equi-spaced, N = 10, kappa = 1/3, ß = 0.85).....67

Figure 4.20: Mesh Dependence Plot Equi-Spaced Mesh (kappa = 1/3) 69

Figure 4.21: Mesh Dependence Plot Equi-Spaced Mesh (kappa = 1/2) 69

Figure 4.22: Mesh Dependence Plot Non Equi-Spaced Mesh (kappa = 1/3, ß = 0.85).....71

Figure 4.23: Mesh Dependence Plot Non Equi-Spaced Mesh (kappa = 1/2, ß = 0.85).....71

Figure 4.24: Mesh Dependence Plot Non Equi-Spaced Mesh (kappa = 1/2, ß = 0.85) for N = 3 - 30 73

Figure 5.1 CFD Analytical Domain as used in the CFD simulation 75

Figure 6.1 Contours of Velocity Magnitude for Inclined Cylinder 81

Figure 6.2 Contours of Velocity Magnitude for Upright Cylinder.....82

Figure 6.3 Contours of Velocity Magnitude for Supine Cylinder.....82

Figure 6.4 Time graph of the cylinder cooling in the upright position 84

Figure 6.5 Effect of wind velocity on convective heat transfer coefficient for upright cylinder 85

Figure 6.6 Effect of wind velocity on convective heat transfer coefficient for inclined cylinder 85

Figure 6.7 Effect of wind velocity on convective heat transfer coefficient for supine cylinder 86

Figure 6.8 Effect of cylinder position on convective heat transfer coefficient for cylinder in 3 different positions.....87

Figure 6.9 Effect of Turbulence Intensities on convective heat transfer coefficient for cylinder in 3 different positions.....88

Figure 6.10 Convective heat transfer coefficient plotted using the predictive formula for cylinder in different positions.....91

Figure 6.11 Comparison of results gathered from CFD simulations to results from predictive formula to results from literature for turbulent flow.....91

Figure 6.12 Effects of wind velocity on the convective heat transfer coefficient for an upright cylinder under laminar flow.....93

Figure 6.13 Effects of temperature difference on the convective heat transfer coefficient for different cylinder positions.....94

Figure 6.14 Trends of CHTC as seen in literature 96

Figure 6.15: Comparison of results gathered from CFD simulations results from literature for Laminar flow 97

Figure 6.16 Effects of temperature difference on the convective heat transfer coefficient for different cylinder positions using the proposed prediction formula 99

Figure 6.17: Comparison of results gathered from CFD simulations to results from predictive formula to result from literature for Laminar flow 99

LIST OF TABLES

Table 2.1 : Convective Heat Transfer Area Ratio for different Postures (Kurazumi *et al*., 2008a; Kurazumi *et al*., 2008b) 8

Table 2.2: Brief review of convective heat coefficients in literature (Virgilio *et al*., 2014) 14

Table 2.3: Comparison of convective and radiative heat coefficient for same wind velocity and temperature gradient 16

Table 4.1: Table showing Varying ß with Minimum Number of Nodes for 1% Error 56

Table 4.2: Showing slope of log-log graph of Error vs. Mesh spacing for low and high number of nodes 60

Table 4.3: Table showing Varying k values with Minimum Number of Nodes for 1% Error ... 62

Table 4.4: Table showing Varying ß with Minimum Number of Nodes for 1% Error for different Kappa values 65

Table 4.5: Showing slope of log-log graph of Error vs. Mesh spacing for QUICK and CUI upwinding 70

Table 4.6: Showing slope of log-log graph of Error vs. Mesh spacing for QUICK and CUI upwinding 72

Table 5.1 CFD Simulation Parameters for turbulent flow 76

Table 5.2 Numerical and Boundary Conditions 78

Table 6.1 Prediction Formula Co-efficient for turbulent flow 90

Table 6.2 Results for the effect of wind velocity of upright Cylinder under laminar flow 92

Table 6.3 CFD Simulation Parameters for laminar flow 93

Table 6.4 Prediction Formula Co-efficient for laminar flow 98

NOMENCLATURE

Symbols

h	Convective heat transfer co-efficient	$Wm^{-2}\,K^{-1}$
U	Velocity	ms
T	Temperature	K
ΔT	Change in temperature	K
Re	Reynolds Number	-
P	Pressure	Pa
ε	Emissivity	%
Q	Heat Flux	W/m^2
ρ	Density of fluid	kg/m^3
μ	Viscosity	kg/ms
A	Area	m^2
V	Volume	m^3
L	Length	m

Subscripts

conv	Convective
R	Radiative
air	Air
T	Total
skin	Skin

Abbreviations

CFD	Computational Fluid Dynamics
TI	Turbulence Intensity
CSP	Computer Simulated Person

Blank Page

1 INTRODUCTION

1.1 BACKGROUND

Over the years, the auto/transport industry and the heating, ventilation and air-conditioning (HVAC) industry have shown interest in the thermal exchange of energy between a body and its thermal environment as it can be seen in literature to be motivations for most of the work done in this area (de Dear *et al*., 1997). More recently however, the need for the development of more accurate investigation apparatus for the Justice industry has grown their interest in this area as well. One implementation could be the determination of the time of death of a human corpse which is one of the motivations for works to be carried out in this paper.

To accurately model such a problem, one needs to make efforts to accurately measure the rate of heat loss from a human body. The various avenues of heat loss coming into play in such a problem would include; radiation, convection and conduction. This presents a very complex problem as a number of additional variables come into play here. Is the human clothed, what material are his garments made from and how do they contribute to the heat exchange between the human corpse and the environment, contact with other surfaces, posture at the time of death, change of environmental conditions since time of death, effective heat exchange areas for the different modes of heat exchange with the environment etc.. The list does become very extensive as each different mode of heat exchange has its different individual variables. For works in this paper, we are to be focused on the convective heat exchange between the human body and the environment using a cylindrical model representative of the human total body surface area and average height.

For the convective heat exchange between the human body and its environment, several variables need to be determined as accurately as possible. These include; the convective heat transfer area of the human body, posture of the human body, effect of body motion, wind speed, wind direction and temperature gradient between the body and its environment. From literature, contradictory work is seen when it comes to the effects of body motion on the convective heat transfer coefficient of the human body. The convective heat transfer area is usually determined directly as described by Kurazumi *et al*. (Kurazumi *et al*., 2008b) where

the effect of posture was also investigated. The effect of temperature gradient, wind speed and direction on the convective heat transfer coefficient have been discussed in a number of works in literature and generally tend to convey the same message as described in the literature review in this paper.

With all the various factors taken into account, different approaches have been used at determining the convective heat transfer coefficient when analysing the convective heat exchange between a body and its environment. These can broadly be characterized into 5 parts;

- Use of heat flux sensors on the surface of the body/simple heat–emitting devices
- Naphthalene sublimation technique
- Use of thermal manikins
- Technique of heat balance investigation of the human body
- Numerical simulations

The above approaches at computation of the convective heat transfer coefficient are discussed in greater detail in Chapter 2.

1.2 CONVECTION HEAT EXCHANGE MECHANISM OVERVIEW

Convection is one of the different modes of heat exchange between the surface of a solid body and the surrounding fluid, be it liquid or gas.

$$\dot{Q}_{conv} = h_{conv} A_{conv} \Delta T \qquad 1.1$$

Where,

h_{conv} = Convective heat transfer coefficient between the surface of the solid and the surrounding fluid flow

A_{conv} = Convective heat transfer area

The rate of convective heat exchange can be expressed by Newton's law of cooling shown in equation 1.1 (Cengel, 2007). The Reynolds number (Re), a dimensionless number expresses the ratio of the inertia forces in the fluid to the viscous forces and is very instrumental to the works carried out in this thesis. It is given by;

$$Re = \frac{UL_x}{v} = \frac{\rho UL_x}{\mu} \quad 1.2$$

Where ρ = density of the fluid

U = velocity of the fluid with respect to the object (the cylinder as used in this thesis)

L = the characteristic length of the cylinder derived as $\frac{V}{A}$, where 'V' is the volume of the cylinder and 'A' is the surface area of the cylinder.

μ = dynamic viscosity of the fluid flowing around the cylinder.

The Reynolds number is very instrumental to the study of fluid flow in general as it is used in determining the range of velocities for laminar and turbulent flow as well as the transition velocity of the fluid from laminar to turbulence.

1.3 DISSERTATION ORGANIZATION

This paper is divided into 6 chapters excluding the current chapter which is the introductory chapter. Each chapter is subdivided into more sub sections for better understanding. The paper is thus organized as follows;

- Chapter 2: the contents of this chapter provides a review of relevant literature for the proposed works on convective heat exchange between a body and its thermal environment. Though works in this paper make use of a representative cylindrical model, it covers the literature for a human body and the environment as this is the basis for this research. This is in addition to the fact that works on convective heat transfer coefficient for plain cylindrical geometries are rarely seen in literature. It summarizes the various factors affecting the determination of the convective heat transfer coefficient as well as gives a brief of the different experimental approaches used in determining the convective heat transfer coefficient over time as seen in literature. The problem encountered with investigating the convective heat transfer coefficient of the human body are then presented, from which the objective and scope of works in this thesis are derived.
- Chapter 3: this chapter presents the theoretical background for the modelling of fluid flow and heat transfer. The governing equations and boundary conditions are presented here as it applies to the work at hand. Various turbulence models are described here and an informed decision is made as to which to use for works in this paper. In addition,

discussions of the accuracy of discretization schemes applicable to works in this paper are started here and further elaborated on in the chapter to follow (Chapter 4).

- Chapter 4: in this chapter, we zoom in to take a closer look at the different schemes available for the discretization of the governing equations presented in chapter 3. Here, a stretched mesh and an equispaced mesh in 1-D are used for the analysis. The accuracy of the various schemes are confirmed by running MATLAB simulations for the different schemes for the exemplary 1-D case of a steady inviscid Newtonian flow in a straight channel (tube) with unit depth and height. It is then followed by a mesh dependency study for both the stretched and equispaced mesh for both first and higher order upwind schemes. This is also conducted in MATLAB. Based on this, conclusions are drawn for this chapter informing our decision on what schemes to employ during the simulations using the ANSYS/FLUENT simulations software package.
- Chapter 5: this chapter leads us into the core works to be carried out in this paper. Here, we present visuals of the domain and cylindrical model to be used for the computational simulations with supporting arguments. Analysis of the effects of the radiative flux in our work is described followed by a description of how the convective heat transfer coefficient is to be obtained from the simulations.
- Chapter 6: all the decisions made in previous chapters haven been implemented in the simulation software ANSYS/FLUENT are used in simulating the fluid flow for both turbulent and laminar. The results from the simulations are presented here with detailed discussions and observations for both the turbulent and laminar fluid flow simulations. The results are then compared to works seen in literature.
- Chapter 7: this brings the paper to an end with a summary on the work carried out in retrospect. Conclusions are drawn and the chapter is brought to an end with recommendations for future works.

2 LITERATURE REVIEW

In this chapter, we present a summary of the available works in literature with regards to the determinations of the convective heat transfer coefficient. The chapter is started with a discussion of the various factors affecting the convective heat transfer coefficient of the human body. It is then followed by the various approaches used in the determination of the convective heat transfer coefficient.

2.1 FACTORS AFFECTING THE CONVECTIVE HEAT TRANSFER COEFFICIENT OF THE HUMAN BODY

2.1.1 CONVECTIVE HEAT TRANSFER AREA OF THE HUMAN BODY

By the definition of convection as a pathway for heat transfer to and from the human body, the total human body surface area, and the respective portion involved in convective heat transfer of the human body needs to be known to determine the convective heat transfer coefficient.

An attempt at measuring convective heat loss from the human body by Hardy (Hardy & Dubois, 1937) makes use of a method described by Dubois (Du Bois & Du Bois, 1916) to determine the total surface area of the human body. Here, a linear height – weight formula proposed by Du Bois (Du Bois & Du Bois, 1916) is used to calculate the total surface area of the human body. Their experiment was conducted with the subject in the lying flat on the back, legs close together and arms close to the body position. For this position, they adopted a standard of 0.78 for the total surface area involved in radiative heat transfer from the human body. With the radiative heat component determined, the convective heat component of the subject was then determined by difference by subtracting the radiative component from the total heat loss from the body (Hardy & Dubois, 1937), thus avoiding the need to measure the convective heat transfer area of the human body directly. This experiment was conducted with a direct calorimetry method using real human subjects in the supine position alone. The calorimetry method used is explained further in section 2.2.3.

In other studies, attempts have been made to directly measure the heat transfer area involved in the convective heat exchange for the human body. One of which is an approach taken by Kurazumi (Kurazumi *et al*., 2003). Here, the human body (using real human subjects) is first entirely covered in surgical tape. Then, with the use of an air brush, an aqueous solution coloured with acrylic paint in a grained texture was sprayed onto the human body surface from all directions. It was then assumed that the area of the body surface not covered by the solution was the non-convective area of the human body. The total tape area used is calculated to give the effective total surface area of the human body, while the total area of tape not covered with the aqueous solution is used to derive the total non-convective heat transfer area of the human body. The areas of the tape to be measured were done using a digitizer (Kurazumi *et al*., 2004).

Body surface areas not covered by the aqueous solution but in contact with other surface – for example the back in contact with the backrest of a chair for a subject in the sitting position, or the feet in contact with the floor, or an entire section in contact with the floor due to the human body lying flat on the floor In the supine position – and thus not involved In convective heat transfer from the body were identified separately by Kurazumi (Kurazumi *et al*., 1997). This was done by the use of a transparent film for the contact between the body surface and the floor. Other areas like the surface area of the human body in contact with the backrest were measured with the above-mentioned method of using an aqueous solution, surgical tape and a digitizer.

In a research by Hardy (Hardy & Soderstrom, 1938), the heat transfer area of the human body was reported to be 0.75 for a body in the supine position. It was also proposed that the heat transfer area of the human body involved in convective heat exchange would vary for different positions, and is thus affected by posture, and needs to be determined for different postures (Hardy & Soderstrom, 1938).

A recent study by Kurazumi (Kurazumi *et al*., 2008a), however, supports this proposition of the effects of posture on convective heat transfer area of the human body by Hardy (Hardy & Soderstrom, 1938), stating that for radiative, conductive and convective heat transfer between the human body and the environment, the heat transfer area ratios differ for different postures using a thermal manikin in their study. From this study Kurazumi proposed

values – shown in Figure 2.1 – for the convective heat transfer area ratio (the ratios of the convective heat transfer area to the total body surface area).

Area ratio	Stnd-exp	Stnd-cod	Chair-exp	Chair-cod	Cross	Leg-out	Supine
Radiation	0.786	0.773	0.741	0.732	0.606	0.686	0.708
Convection	0.954	0.948	0.918	0.860	0.843	0.906	0.844

Radiative heat transfer area ratio [N.D.] is the radiative heat transfer area to the total body surface area of the human body. Convective heat transfer area ratio [N.D.] is the convective heat transfer area to the total body surface area of the human body.

Figure 2.1 Heat transfer area ratios for calculating heat transfer coefficients (Kurazumi *et al*., 2008a)

The effect of posture on the convective heat transfer coefficient cannot be overlooked if one is to obtain reasonably accurate results for the convective heat transfer coefficient of a body. Because convective heat exchange has typically been derived by difference (subtracting radiative and conductive heat loss in some cases form the total heat loss recorded form the body under the same conditions), the values proposed by Kurazumi (Kurazumi *et al*., 2008a) have little to no previous studies to be compared to. The value of 0.75 proposed by Hardy (Hardy & Soderstrom, 1938) for a body in the supine position doesn't lie too far off that from Kurazumi's results of 0.844 for a body in the supine position as shown in Table 2.1. If this is any indicator to go by, these values can be used to approximate the convective heat transfer area of a dead corpse once it's total body surface area is known. Another approach to this problem could be to use computer models, programming the models such that the total surface area of the models minus the surface area of the models that appose each other (or other surfaces) would equal the total convective heat transfer area for any given posture.

2.1.2 POSTURE

In literature, it is seldom found that a study on the convective heat transfer area of the human body is conducted with a single subject in different positions. This makes it quite difficult to establish standard mean values for the heat transfer area of the human body. One attempt at this was by Kurazumi who (Kurazumi *et al*., 2008b) used a single human subject in 8 different postures (standing, chair sitting, seiza sitting, cross-legged sitting, sideway sitting, both-knees-erect sitting, legs-out sitting, lateral and supine) in his experimental approach at determining the convective heat transfer area of the human body. The total and convective heat transfer surface area was determined directly as demonstrated by Kurazumi (Kurazumi *et al*., 2003) – using an aqueous solution, surgical tape and a digitizer – for the human subjects

for different postures described in previous paragraphs. Kurazumi proposed the following values from his study;

Table 2.1 : Convective Heat Transfer Area Ratio for different Postures (Kurazumi *et al*., 2008a; Kurazumi *et al*., 2008b)

Posture	Convective Heat Transfer Ratio
Standing	0.942
Chair Sitting	0.910
Seiza Sitting	0.853
Cross – Legged	0.843
Sideways Sitting	0.877
Knee Erect	0.865
Leg Out	0.878
Lateral	0.879
Supine	0.811

The difference in these values does present an indication of the importance of posture in calculating the convective heat transfer area and thus the convective heat transfer coefficient of the human body. However, these values differ from that proposed in a previous study by Kurazumi (Kurazumi *et al*., 2008b) as shown in Figure 2.1. The differences in values can be attributed to the fact that different methods were used for measuring the heat transfer area ratios. Taking a closer look at the values proposed in **Table 2.1**, we see that even in the standing position and chair sitting positions which are regarded as open body positions, 6-9% of the body surface still doesn't contribute to convective heat exchange between the body surface and the environment (Kurazumi *et al*., 2008b).

2.1.3 EFFECT OF BODY MOTION

When the human body is in motion (walking, running, etc.) with limbs swinging in relation to the body, Clark *et al*. (Clark *et al*., 1974) described this as the pendulum effect. The pendulum effect basically describes a scenario where the peripheral limbs of the moving body swing both with and against the general flow of air in quick successions. This thus translates into an increase and decrease in the relative air speed and corresponding convective heat losses from

the limbs in question. The interesting thing here however is that for the human running at a particular speed (x.m/s) in still air, Clark *et al*. proposes that this does not translate into and the human body stagnant in a stream of air with velocity equivalent to that of the running human (x.m/s). This is due to the pendulum effect. They proposed that the local convective heat transfer coefficient of the human body can be increased by a factor of 2 during motion (running) due to the pendulum effect (Clark *et al*., 1974).

On the contrary, Chang *et al*. (Chang, Arens & Gonzalez, 1998) proposed that pure convection is decreased by the pendulum effect when subjects are subjected to motion. By using an articulated thermal manikin and the naphthalene sublimation technique – explained further in section 2.2.2 – the thermal manikin was subject to constant temperature of 30° and wind speed (0.4 – 0.7 m/s: thus forced convection). The manikin was made to simulate 5 different walking patterns all between 0 – 0.9m/s walking speed. They showed through their experiments that there was a 5-7% decrease in the convective heat transfer coefficient of the human body in motion due to the "pendulum effect" with swinging peripheral body parts like the arms and the legs.

The difference in the works of Clark *et al* (Clark *et al*., 1974), and that of Chang *et al* (Chang, Arens & Gonzalez, 1998) could possibly be due to the fact that in the works of Clark *et al*, though stated that the pendulum effect would affect other heat exchange pathways from the body for example vaporization, the magnitude of the effect was not clearly separated for each pathway. The increase in the heat exchange coefficient could thus be due to increases in other heat exchange pathways, for example, through radiation or vaporization as stated by Chang *et al* (Chang, Arens & Gonzalez, 1998).

Asides these two contradictory works, the pendulum effects, though present is seldom discussed in recent literature. However, because this study has to do with corpses, the effect of body motion (or the pendulum effect) is of little concern in this study.

2.1.4 WIND SPEED

In a work by Dear *et al*. (de Dear *et al*., 1997), an articulated thermal manikin with 16 body parts is used in the analysis of both natural and forced convective heat transfer coefficients of the human body. By the use of a wind tunnel facing the thermal manikin at various azimuth

angles (to account for wind direction in the horizontal) with varying wind speeds, they were able to simulate microclimatic conditions from still air conditions with wind speed $V < 0.1m/s^2$, to forced convection where wind speeds v was varied between $0.2m/s^2$ and $0.5m/s^2$. For their experiments, 8 wind speeds were used ($0.1m/s^2 \leq v \leq 5m/s^2$) with wind speeds v of $0.2m/s^2$ considered as simulating forced convection. For every wind speed, the thermal manikin was reoriented to different azimuth angles starting from $0° - 180°$ (with 45° increments in the azimuth angles) to account for the effects of the wind direction on the convective heat transfer coefficients of the different body parts, as well as on the body as a whole. These were done in both the standing and seating postures.

For increasing wind speeds, Dear *et al*. (de Dear *et al*., 1997) proposed that for forced mode convection of the human body parts, at the highest wind speeds investigated (V = $5m/s^2$), the convective heat transfer coefficient of the core body segments (such as the chest, back and pelvis) were much lower than those of the hands and feet of the body with about 40 to 60% difference in favour of the hands and feet, and that the farther away the body part from the core body segments, the higher the convective heat transfer coefficient is, thus leaving the lower legs and feet to have much higher convective heat transfer coefficients for both forced and natural convective heat transfer (de Dear *et al*., 1997). For lower air speeds (V < 0.8m/s) – which is of most concern in this paper – typically of indoor conditions simulating natural convective heat transfer, this difference was seen to increase to above 60% with the lower legs and feet having higher convective heat transfer coefficients for both the seating and the standing position. Thus, though usually assumed in literature that convective heat exchange takes place uniformly across the whole body's surface at a uniform rate, these findings tell us otherwise. This variation in convective heat exchange co-efficient for different body parts is seen in the Figure 2.2.

Manikin segment	Seated natural convective h_c (W/m^2 per K)	Standing natural convective h_c (W/m^2 per K)
Foot (l and r)	4.2	5.1
Lower leg (l and r)	4.0	4.1
Thigh (l and r)	3.7	4.1
Pelvic region	2.8	3.4
Head	3.7	3.6
Hand (l and r)	4.5	4.1
Forearm (l and r)	3.8	3.7
Upper arm (l and r)	3.4	2.9
Chest	3.0	3.0
Back	2.6	2.9
Whole body	3.3	3.4

Figure 2.2: Natural convective heat transfer coefficients for the nude thermal manikin in still air (V <0.10m/s) (de Dear *et al.*, 1997)

In support to de Dear *et al*., (de Dear *et al*., 1997), are more recent research. One of such is a work by Virgilio *et al*. (Virgilio *et al*., 2012), where the effect of wind speed on the convective heat transfer coefficient on the human body by the use of an articulated human manikin is analysed. In their work, it can be seen that wind speed had very little to no effect on the convective heat transfer coefficient of the core body parts (chest, back, head and pelvic region). Their work does however demonstrates that the convective heat transfer coefficient of the human body is affected by wind speed as higher values of convective heat transfer coefficient correspond to higher wind speeds. This statement is also reinforced in a work by Chang *et al*., (Chang, Arens & Gonzalez, 1998) whereby it was noticed that the convective heat coefficient of a standstill manikin increases accordingly with increasing air velocity. This is interesting to note as the investigations by Chang *et al*., (Chang, Arens & Gonzalez, 1998) were done using a different approach (use of the naphthalene sublimation technique discussed in section 2.2.2) in analysing the convective heat transfer coefficient from that of de Dear *et al*., (de Dear *et al*., 1997) who used a thermal manikin.

Further works that support these propositions include works of Nielsen *et al* (Nielsen & Pedersen, 1952). In their works, they showed that for air velocities lower than 0.1m/s, the convective heat loss of the human body is independent of the air velocity in the surroundings and dependent solely on temperature difference between the body and air in the surrounding

environment. For air velocities 0.2 < v < 0.8m/s, de Dear however proposed a general equation to be used regardless of the posture, basically implying that for lower wind velocities, the heat loss by convection between different postures become negligible;

$$h_c = 10.3v^{0.6} W/m^2 perK \qquad 2.1$$

At wind velocities < 5m/s, convective heat exchange doesn't take place at a uniform rate across the body's surface with this difference exaggerated for lower wind velocities (de Dear *et al*., 1997). This is to be accounted for in the present study as most of the scenarios would ideally simulate natural convective cooling.

2.1.5 WIND DIRECTION

From the work of Dear *et al*. (de Dear *et al*., 1997) described in previous paragraphs (section 2.1.4), it was also proposed that the wind direction was an important factor in only a select few segments of the human body (typically the feet and lower legs) in determining the convective heat transfer co-efficient for both natural and forced convection in the human body. This was also depending on the azimuth orientation of the human body to the direction of the wind onto the body, and was generally less pronounced for the standing position (de Dear *et al*., 1997).

Another work that had a look at the effect of wind direction on convective heat transfer co-efficient 'h_c' was one by Cong *et al*. (Cong & Kazuhide, 2012). They proposed that h_c of the human body was approximately 9 to 19% higher for flow approach from the front (that is 0° azimuth angle as described by Dear *et al*. (de Dear *et al*., 1997)) as opposed to other wind directions. This was done for the subject in the standing position alone.

2.1.6 TEMPERATURE GRADIENT BETWEEN THE BODY AND THE ENVIRONMENT

The works of Nielsen *et al* (Nielsen & Pedersen, 1952) showed that for air velocities lower than 0.1m/s, the convective heat loss of the human body is independent of the air velocity in the surroundings and dependent solely on temperature difference between the body and air in the surrounding environment. In a study by Winslow *et al* on Partitional calorimetry (Winslow, Herrington & Gagge, 1936), the method of heat balance to determine the convective and radiative exchanges from the human body was used.

$$C = (A + BV)\Delta T \quad 2.2$$

$$C = A\sqrt{V}\Delta T \quad 2.3$$

Where;

C = Convective heat loss

V = Velocity of air

ΔT = difference between skin temperature and air temperature

A & B = arbitrary constants

In their works Winslow *et al*. (Winslow, Herrington & Gagge, 1936), two equations were for determining the convective heat transfer coefficient of the human body; equation 2.2 and 2.3 (Winslow, Herrington & Gagge, 1936).

From both of the equations, we immediately notice the dependence of the convective heat loss on the difference between skin and air temperature. It can also be seen that for an increasing temperature gradient, the heat loss by convection would see an increase.

The work of Kurazumi *et al* (Kurazumi *et al*., 2008b) supports this proposition as through experimentation, they showed that, as the temperature difference grows larger between the skin and air temperatures, the convective heat coefficient is also seen to increase. The dependence of convective heat transfer coefficient on the temperature gradient between the body's surface temperature and that of the atmosphere is a generally accepted notion, and various relationships for this have been derived (shown in Table 2.2) based on both theoretical and experimental approaches. Of interest here is the fact that all of these are based on steady state behaviours as opposed to a transient state which would be experienced in the analysis of heat transfer from a corpse.

Table 2.2: Brief review of convective heat coefficients in literature (Virgilio *et al*., 2014)

Convective heat transfer coefficient ($W/m^2 * K$)	Posture	Air Velocity	Author
$1.007 * \Delta T^{0.406}$	Standing (no floor contact)	V < 0.2m/s	(Kurazumi *et al*., 2008a)
$1.183 * \Delta T^{0.347}$	Standing (floor contact)		
$1.175 * \Delta T^{0.351}$	Chair sitting exposed to atmosphere		
$1.222 * \Delta T^{0.299}$	Chari sitting contact with seat, chair back and floor		
$1.271 * \Delta T^{0.355}$	Cross-legged sitting (floor contact)		
$1.002 * \Delta T^{0.409}$	Legs out sitting (floor contact)		
$0.881 * \Delta T^{0.368}$	Supine (floor contact)		
3.4	Standing	V < 0.1m/s	(de Dear *et al*., 1997)
3.3	Sitting		
$2.02 * \Delta T^{0.24}$	Standing	V < 0.15m/s	(Quintela, Gaspar & Borges, 2004)
$1.94 * \Delta T^{0.23}$	Sitting		
$2.48 * \Delta T^{0.18}$	Supine		
$1.21 * \Delta T^{0.43}$	Standing	V<0.1m/s	(Oguro *et al*., 2002)
$0.78 * \Delta T^{0.59}$	Sitting		

Where;

$\Delta T =$ Temperature difference between the skin surface temperature of the subject, and that of the atmosphere. The values shown for de Dear in the table above are for a temperature difference of 12K.

2.1.7 EFFECT OF RADIATIVE HEAT LOSS

Convective loss from the human body is hardly mentioned in literature without a mention of radiative loss. This is partly due to the fact that some authors have analysed and determined the convective heat transfer coefficient for the human body by difference. This technique is

primarily based on the notion that total dry heat loss form the human body is the sum of the convective and radiative components (de Dear *et al*., 1997). With the temperature difference between the subject's surface temperature and the atmosphere equal to zero ($T_{skin} = T_{air}$), the convective heat exchanges from the body can thus be ignored, leaving total dry heat loss from the body to be almost purely radiative. By equating the mean radiative temperature to the atmospheric temperature of the test chamber, the radiative component can easily be determined experimentally. One way this can be achieved is seen in the work by de Dear (de Dear *et al*., 1997) where the manikin was coated with aluminium foil of known low emissivity (ε) equal 0.10, with that of the nude subject (a manikin) equal to 0.95. The total dry heat loss of the uncoated manikin with the temperature gradient of approximately 0 is then equated to the total dry heat loss from the coated manikin still with temperature gradient equal 0. This is described in the following calculation;

$$
\begin{aligned}
&h_{\mathrm{r(uncoated)}} - h_{\mathrm{r(foil)}} = h_{\mathrm{uncoated}} - h_{\mathrm{foil}} \\
&h_{\mathrm{r(foil)}} = \frac{0.1}{0.95} h_{\mathrm{r(uncoated)}} \\
&h_{\mathrm{r(uncoated)}}\left(1 - \frac{0.1}{0.95}\right) = h_{\mathrm{uncoated}} - h_{\mathrm{foil}} \\
&h_{\mathrm{r(uncoated)}} = 1.12\left(h_{\mathrm{uncoated}} - h_{\mathrm{foil}}\right) \quad (\mathrm{W/m^2\ per\ K})
\end{aligned}
\qquad 2.4
$$

Determining the radiative heat transfer coefficient in this way allows for reasonable estimates of both the radiative and convective heat transfer coefficient to be determined without much worry for determination of convective heat transfer areas taking into account a trade off with accuracy. For the present study this is not an advisable route to determination of the convective heat transfer coefficient. That being said, some work has been done in determining the effective radiative heat transfer area of the human body. Kurazumi *et al* (Kurazumi *et al*., 2008a) presents his finding shown in Figure 2.3. Asides these, very little work is encountered in literature with respect to the effective radiative heat transfer area as with the effective convective heat transfer area discussed in earlier paragraphs (section 2.1.1). Figure 2.3 is shown below again for continuity.

Area ratio	Stnd-exp	Stnd-cod	Chair-exp	Chair-cod	Cross	Leg-out	Supine
Radiation	0.786	0.773	0.741	0.732	0.606	0.686	0.708
Convection	0.954	0.948	0.918	0.860	0.843	0.906	0.844

Radiative heat transfer area ratio [N.D.] is the radiative heat transfer area to the total body surface area of the human body. Convective heat transfer area ratio [N.D.] is the convective heat transfer area to the total body surface area of the human body.

Figure 2.3: Heat transfer area ratios for calculating heat transfer coefficients (Kurazumi *et al.*, 2008a)

From the table, the radiative heat transfer area of the human body is typically smaller that it's convective counterpart. This doesn't necessarily translate into actual convective heat loss being greater as the radiative heat transfer coefficient of the human body is typically larger than the convective heat transfer coefficient of the body. This is seen by the values proposed in the works of de Dear (de Dear et al., 1997) as shown in Table 2.3.

Table 2.3: Comparison of convective and radiative heat coefficient for same wind velocity and temperature gradient

Posture	Radiative Heat Transfer Coefficient ($Wm^{-2}\,K^{-1}$)	Convective Heat Transfer Coefficient ($Wm^{-2}\,K^{-1}$)	Temperature Gradient (skin to air) (K)	Wind Velocity (m/s)	Author
Seated	4.5	3.3	12	V < 0.1	(de Dear *et al.*, 1997)
Standing	4.5	3.4			

That being said, in the same light, a simple way to estimate the convective heat loss from a subject would be to cover the body with aluminium foil of very low emissivity such that the total dry heat transfer of the manikin is almost entirely convective with a known temperature difference.

2.2 POSSIBLE EXPERIMENTAL APPROACHES TO DETERMINING THE CONVECTIVE HEAT TRANSFER CO-EFFICIENT OF THE HUMAN BODY

2.2.1 USE OF HEAT FLUX SENSORS ON THE SURFACE OF THE BODY/SIMPLE HEAT–EMITTING DEVICES

Clark *et al* (Clark & Toy, 1975) made use of small surface calorimeter plates to measure the local heat transfer from the human body (they focused on the human head). The plate calorimeters consisted mainly of two temperature sensing devices (thermocouples) arranged

face to face. The calorimeters were attached to the skin by use of double sided adhesive tapes with insulation against the skin. The associated wiring and thickness of the calorimeter plates were such that they didn't affect the convective flow patterns as shown by a *Schlieren device*. Electric power was applied to the calorimeter until the thermocouple junctions are of equal temperatures so as to eliminate the effect of conductive flow across the calorimeter. Their experiments were conducted in a climatic chamber with still air conditions with the walls, ceilings and floor lined with similar material so as to have uniform radiation to each surface. With this, any change in the measured heat output would thus be due to convective heat transfer differences. The calorimeters were attached to different parts of the human head as shown in Figure 2.4 used to measure the local heat transfer rates used to determine the convective and radiative heat losses of the human head (Clark & Toy, 1975).

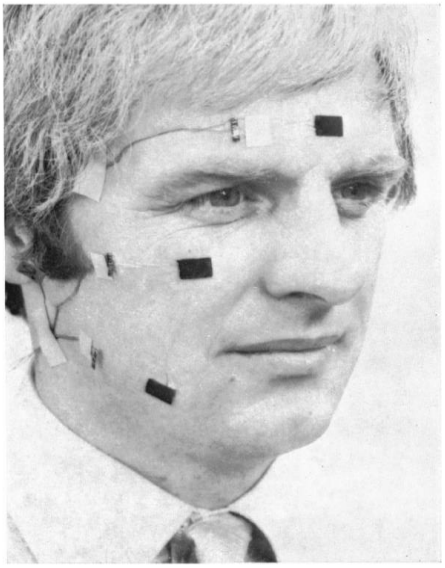

Figure 2.4: Calorimeter plates setup on the human head of one of the subjects for the experiment. (Clark & Toy, 1975)

A similar approach is used in a thesis by Danielsson in 1993 at the royal Institute of Stockholm as referenced by de Dear *et al*, (de Dear *et al*., 1997). Danielsson's approach was similar to that used by Clark *et al* (Clark & Toy, 1975) as explained in previous paragraphs. The main difference was that Danielsson masked the temperatures sensing devices – flat disks – (similar to the surface plate calorimeter used by Clark *et al*) used in his experiment with aluminium foils with known emissivity in order to eliminate the radiant component of the disks. This way, when the two disks achieve equilibrium temperature corresponding to the surface in which

they are attached to, the net heat flux through the instrument can be determined with knowledge of the temperature gradient between the two disks and the known resistance separating them.

Though this technique is seldom encountered in literature, one advantage it presents is that subject in motion can be analysed as well and values at any point across the human body's complex morphology can be determined. The main disadvantage is the fact that the instruments itself interfere with the air flow around the body and the temperature across the surface it is being attached to (de Dear *et al*., 1997).

2.2.2 NAPHTHALENE SUBLIMATION TECHNIQUE

The naphthalene sublimation technique is one whereby the rate of naphthalene sublimation is used as a proxy for the process of convective heat transfer (de Dear *et al*., 1997). Many of the work found in literature on the use of the naphthalene sublimation technique with regards to the convective heat transfer process make reference the works of either Chang *et al*., (Chang, Arens & Gonzalez, 1998) or that of Nishi *et al*., (Nishi & Gagge, 1970).

In a study by Chang *et al*., (Chang, Arens & Gonzalez, 1998), the convective heat transfer coefficient of the human body is investigated using the naphthalene sublimation technique in addition while making use of an articulated manikin. The main difference from the use of thermal manikins is the fact that the manikins used are not thermal manikins with controlled skin temperature thus their total surface area is not accounted for in the experimental procedures. In their study, "Scintillation" grade naphthalene with a melting point of 80°C is casted by use of casting disk cassettes which where appropriately curved to conform to surface curvatures of the corresponding body segments (upper arm, lower arm, thigh and calf). However, casting cassettes used for the chest were not curved to conform to any curvature. The surface area of each cassette disk is quantified and used in determination of "$\dot{m}$" the naphthalene sublimation loss per surface area as shown in the mass transfer relationship of naphthalene sublimation as presented in Nishi and Gagge, (Nishi & Gagge, 1970) in equation 2.5 below.

$$h_m = \frac{\left(R \times T_a \times \dot{m} \right)}{\left(P_s - P_a \right)} \qquad 2.5$$

Where;

h_m = naphthalene mass transfer co-efficient (m/s)

$\dot{m}$ = measured naphthalene sublimation loss per surface area $(\mathrm{kg\,m^{-2}\,s^{-1}})$

T_a = ambient temperature (K)

P_s = naphthalene surface vapour pressure (mmHg)

P_a = naphthalene vapour pressure in air (assumed = 0)

R = naphthalene gas constant $(0.487 mmHg\,m^3\,kg^{-1}\,K^{-1})$

Shown below in Figure 2.5 is an illustration of the locations of the naphthalene disks on the manikin.

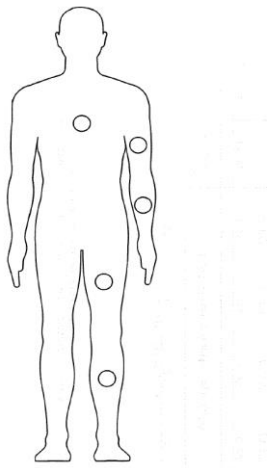

Figure 2.5: Schematic diagram of a human model showing the locations of the naphthalene disk on the manikin (Chang, Arens & Gonzalez, 1998)

Vinyl retainers were fastened onto the manikin with hooks and pile straps. The disks were then mounted on to the retainers. The naphthalene disks were then weighed immediately before and after an experiment on a scale balance of +/- 0.1mg (Chang, Arens & Gonzalez, 1998).

One down side of this method explained above is the fact that the disks did not cover the total surface area as well as the total circumference of the body segment being measured and thus the flow of air around the body is not accounted for. Here, just the local convective heat transfers at the locations of the naphthalene disks have been considered as opposed to an average value for the convective heat transfer coefficient for the body. Also, this is noteworthy as from the flow analysis of a cylinder (approximating body segments to be cylinders); one can see that the flow around a cylinder yields a higher convective coefficient than in the local regions as setup in the above experiment (Chang, Arens & Gonzalez, 1998).

The technique described above as used by Chang *et al*., (Chang, Arens & Gonzalez, 1998) is a modification of that originally used by Nishi and Gagge (Nishi & Gagge, 1970). The main difference between the above explain method of Chang *et al*., (Chang, Arens & Gonzalez, 1998) and that of Nishi and Gagge (Nishi & Gagge, 1970) is that in the work of Nishi and Gagge, (Nishi & Gagge, 1970), instead of circular disks, naphthalene balls of 3-cm diameter were used, located evenly over the body at 3-cm off the body surface. This still presents the problem described in the above paragraph.

Though seldom found in recent study, the use of naphthalene sublimation when encountered is a play between the above explained two sublimation techniques by Chang *et al*., (Chang, Arens & Gonzalez, 1998) and Nishi and Gagge (Nishi & Gagge, 1970). This is mainly because of the compromise in accuracy in results when one makes use of the naphthalene sublimation technique. That being said, the main disadvantage in using this technique in the investigation of convective heat transfer is the “spot nature” of the results, as the total body surface area of the manikin is not involved in the investigation of the convective heat transfer area/coefficient (which as explained in section Factors affecting the convective heat transfer coefficient of the human body is of great importance in convective heat transfer of the human body). To achieve more accurate results, it thus presents even more laborious experimental procedures, somewhat impractical when one considers the available options today as much work has been done since these techniques were first used.

2.2.3 TECHNIQUE OF HEAT BALANCE INVESTIGATION OF THE HUMAN BODY

Another approach at determining the convective heat exchange of the human body a few researchers in literature have used is the analysis of the heat balance of the human body and

its surrounding environments. Although a number of researchers in recent times attempt to use this approach, the methods used in the works of Winslow *et al*, (Winslow, Herrington & Gagge, 1936) and that of Hardy *et al*, (Hardy & Dubois, 1937) are typically employed.

In the works of Hardy *et al*., (Hardy & Dubois, 1937) a direct calorimetry method is used to determine the total heat lost from the human body (radiation and convection). The heat lost by convection is then determined by subtraction as the heat lost via radiation is measured directly in his experiment. The human body is placed in the calorimeter and sealed. Air flow through the calorimeter from the head of the calorimeter positioned close to the head of the subject is assumed adequate to remove body gases but not sufficient to affect heat loss. This is because the air is "baffled" as it enter the head of the calorimeter so there is no air movement perceptible to a delicate anemometer, and thus to the naked subject.

Cold water flowing in pipes just above the roof of the calorimeter is used for removing the total heat from the calorimeter. The water temperature is measured right before it enters the box, and after it leaves the box. The heat removed using the flowing water is assumed to typically be the total of radiation and convection as it is assumed that the heat lost by conduction is negligible due to the experimental set up. The average radiating temperature of the surface of the body is determined by pointing the radiometer at twenty points (as shown in Figure 2.6) on the surface of the human body and measured directly.

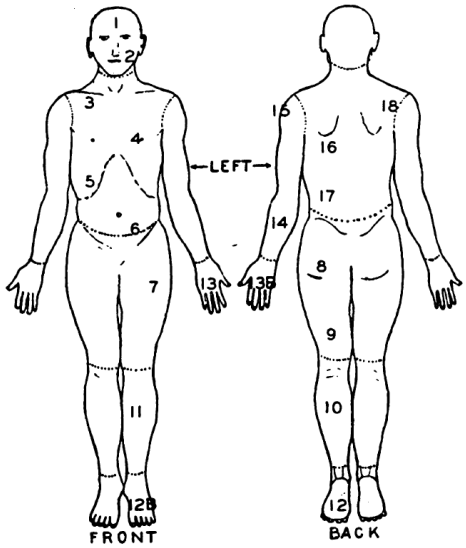

Figure 2.6: Locations of individual areas over the body surface which were tested and the division of the skin surface for weighting. (Hardy & Dubois, 1937)

It is important to note here that measurement of radiation and of total heat lost by the body (measured through the flowing water) is only conducted once the system is in equilibrium. That being said, some-time is thus allowed after the subject is positioned in the calorimeter in the supine position for the system (subject plus calorimeter) to reach equilibrium. Thus, measurements are basically done over a period of time of which the subject has to remain as quiet and motionless as possible.

The proportions of the total surface contributed by the various body sections as divided are accounted for from the linear formula, and the average radiation for each section is then multiplied by the percentage of the total area contributed by the body part (section). The various weighting factors are computed from the linear formula measurements of sixteen subjects. Finally, measurements of the radiation of the internal surfaces of the calorimeter are taken to determine the radiation exchange between the subject and the calorimeter. Once this is done, the total heat lost by radiation is then subtracted from the total heat lost from the body to determine the heat lost by convection.

One obvious downside of this approach is the fact that measurements are conducted over a period of time of which accuracy is somewhat affected by the human subject as he/she has to remain as still as possible during the experimental period. Another downside is that the effects of convection and radiation are not differentiated during the experiments, as it does not provide the opportunity of determining radiation and convective losses separately.

These two apparent problems were somewhat tackled in the works of Winslow *et al*., (Winslow, Herrington & Gagge, 1936). In their works, they presented a method of Partitional Calorimetry. Their method affords the separate determination of radiative and convective heat losses once the mean radiant temperature and the mean surface temperature of the subject can be controlled and made equal to each other. This was based on the theory that the sum of the Convective (C) and Radiative (R) heat loss from the body is equivalent to that of the Total Heat (H) produced by the body minus the Evaporative heat loss (E) of the body plus or minus the change in body in heat content (Nielsen & Pedersen, 1952). Also, the works of Winslow *et al*, (Winslow, Herrington & Gagge, 1936), makes it possible for readings to be done in relatively shorter periods of time.

In their work, the subject is placed in a nine-sided copper enclosure in an air conditioned chamber. Radiant heaters introduce infra-red radiation reflected and diffused over the entire enclosed area. This way, the mean radiation temperature is controlled and known at all times. The setup thus allows for variation of the mean radiation temperature independent of the ambient air temperature. The enclosure allows the free circulation of air from the air conditioned chamber so that the air within the enclosure is slightly above that of the air conditioned chamber. With the subject in the copper enclosure, mean skin temperature is determined by use of a thermopile over 15 body region as seen in Figure 2.7.

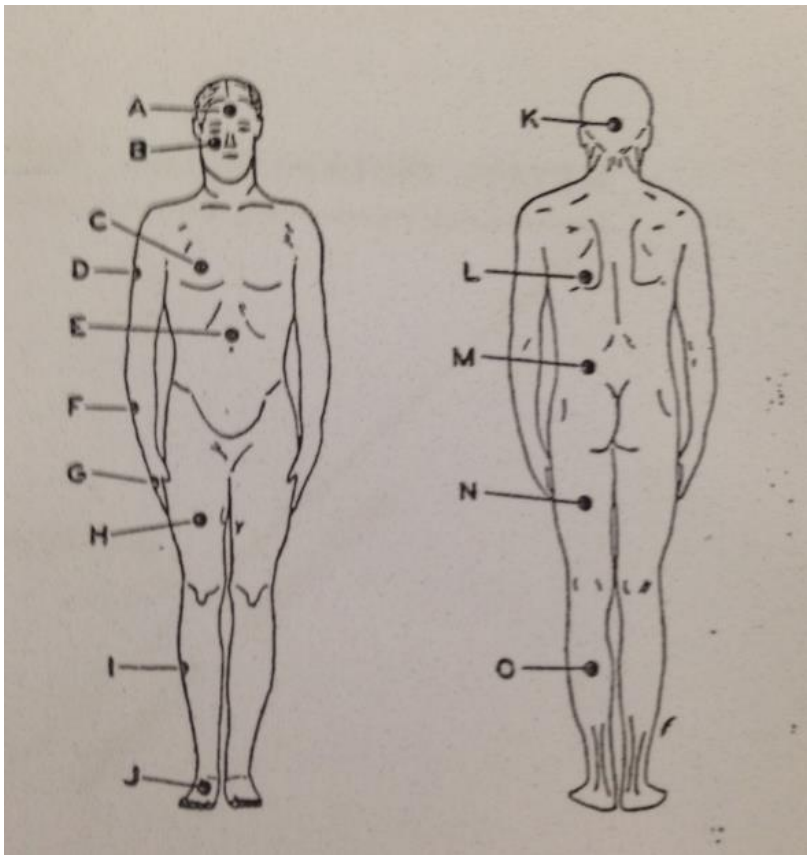

Figure 2.7: Fields (body regions) used for air movements and skin temperature observations (Winslow, Herrington & Gagge, 1936)

The temperature values are then weighted by a factor numerically equivalent to the percentage of the total surface area represented by the separate segments. Thus, somewhat accounting for the effective convective area. Once this was done, the convective loss was then determined by the relation shown in equation 2.6. Another equation as presented in their works is show in equation 2.7. They showed through experimentation in their works (Winslow, Herrington & Gagge, 1936) that the practical difference between the results of

using either of the equations is negligible for the range of air movements they considered; 0.0762m/s – 0.3556m/s (Winslow, Herrington & Gagge, 1936).

$$C = (A + BV)\Delta T \qquad 2.6$$

$$C = A\sqrt{V}\Delta T \qquad 2.7$$

Where;

V = Velocity of air

ΔT = difference between skin temperature and air temperature

A & B = arbitrary constants

By the use of their Partitional calorimetry method and the expression above, one of the by-products of this method is the fact that the effective radiative surface area of the human body can be deduced (and thus the convective surface area of the human body) once all arbitrary constants have been determined from the graphs of the equations after conducting several experiments (Winslow, Herrington & Gagge, 1936). As shown in the works of Winslow *et al*, a comparison of the convective losses determined by the use of their Partitional calorimetry method and the equations above with that determined by difference, similar to the works of Hardy *et al* described above (Hardy & Dubois, 1937), has an error of less than 4% (Winslow, Herrington & Gagge, 1936).

2.2.4 USE OF THERMAL MANIKINS

With thermal manikins, heat flux measurements are made with circuitry embedded below the surface of the manikin making them more accurate due to the fact that they are less obtrusive (de Dear *et al*., 1997) as opposed to techniques described in previous paragraphs. In the works of de Dear *et al*, (de Dear *et al*., 1997), an articulated thermal manikin was used to investigate both radiative and convective heat transfer coefficients of the human body. The manikin used in their study simultaneously measures total dry heat transfer from its surface (skin) as well as its corresponding temperature. The manikin similar in build to that of a

'female show room dummy' has 16 independent body parts. Each body part consists of a 4mm thick fibre-glass polyester shell covered with 0.3mm nickel wire wound at a spacing of 2mm to ensure even heating across the entire surface area of each body segment. The total body surface area of each segment of the manikin is predetermined as indicated in Figure 2.8. Each segment of the manikin is controlled separately by an external computer which works on the assumption that under steady state conditions, the heat lost from the skin (of a particular segment) to the environment is equal to the heat supplied to the nickel heating element of the respective segment. The convective and radiative heat loss can then be separated by assuming that the mean air temperature was equal to the mean radiant temperature in the operating environment (de Dear *et al*., 1997). The segmentation of the manikin allows for various configurations of the manikin (seating, standing, supine etc.). It also allows the body to simulate realistic body motion to some degree of accuracy. However, in their study, they only focused on the standing and seated position illustrated in Figure 2.8. Simulation of realistic body motion becomes very important when one wants to investigate the effect of body motion or the pendulum effect on the convective heat transfer coefficient of the human body as described in section 2.1.3. The manikin's skin temperature was cooled naturally as it did not have a heat loss mechanism.

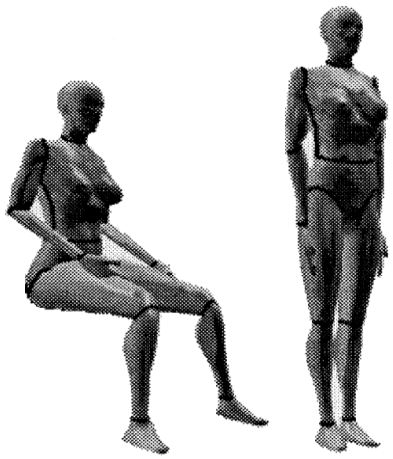

Manikin Segment	Surface Area (m^2)
left foot	0.043
right foot	0.041
left lower leg	0.089
right lower leg	0.089
left thigh	0.160
right thigh	0.165
pelvic region	0.182
head	0.100
left hand	0.038
right hand	0.037
left forearm	0.052
right forearm	0.052
left upper arm	0.073
right upper arm	0.073
chest	0.144
back	0.133
Total	**1.471**

Figure 2.8: Manikins segmentation and respective surface area, and illustration of postures investigated in study (de Dear *et al*., 1997)

The manikin is placed in a boundary layer wind tunnel where it is exposed to a variety of accurately regulated wind speeds. Wind speeds are measured using a heated element anemometer suspended in the air steam by a programmable stepper-motor vertical mast. Readings made from the experiment are then used to make calculations of the radiant heat transfer coefficients. The radiant temperature is determined by the use of equation 2.8 (de Dear *et al*., 1997).

$$h_r = 1.12(h_T - h_{foil})\ W/m^2 \qquad 2.8$$

Where;

h_T = Total dry heat transfer for nude manikin

h_{foil} = Total dry heat transfer with an aluminium foil with known emissivity ($\varepsilon = 0.10$)

The value for h_{foil} is obtained by repeating the experimental procedure with the manikin wrapped in an aluminium foil coating of known emissivity. This is to reduce the radiative component to as little as possible to enable the derivation of equation 2.8. This can be seen in their publication (de Dear *et al*., 1997).

The convective heat transfer coefficient is then determined by subtracting the radiant heat transfer coefficient form the total dry heat transfer coefficient of the naked manikin. In the above described work of de Dear *et al* (de Dear *et al*., 1997), the effective heat transfer area for radiation and convection were not explicitly accounted for. By doing this, it is being implied that all portions of the body parts are equally exposed to convective flows except for those that must be physically blocked – like the soles of the feet (Kurazumi *et al*., 2008b). In the works of Kurazumi *et al*, (Kurazumi *et al*., 2008b), an articulate manikin placed in an artificial climate chamber was also used for the investigation of the radiative and convective heat transfer coefficient. Kurazumi *et al* (Kurazumi *et al*., 2008b) accounted for the effect of the heat transfer area for each posture. This was done by incorporating heat transfer area ratios for each manikin posture examined. The heat transfer area ratios used for determining the heat transfer coefficient is shown in Figure 2.1 in section 2.1.1. Due to the inclusion of the heat transfer area ratio for each body segment of the manikin, the radiative and convective

heat transfer coefficient where calculated with formulas – described in (Kurazumi *et al*., 2008b) – different from that used above by de Dear *et al* (de Dear *et al*., 1997).

2.2.5 NUMERICAL SIMULATIONS

In more recent years, with the advancement of computing power, various experimental works have been biased where applicable towards computational simulations for the obvious reasons of more controlled conditions and thus better accuracy. The determinations of the convective heat transfer coefficient is not an exception to this. Here, works carried out by use of a thermal manikin are simulated using fluid flow and heat transfer software packages with similar methodology to their experimental counterparts, where the thermal manikin is replaced by a computer simulated person (CSP)/virtual manikin and simulated using principles of computational fluid dynamics (CFD). The analytical domain with the CSP is usually arranged as represented in Figure 2.9.

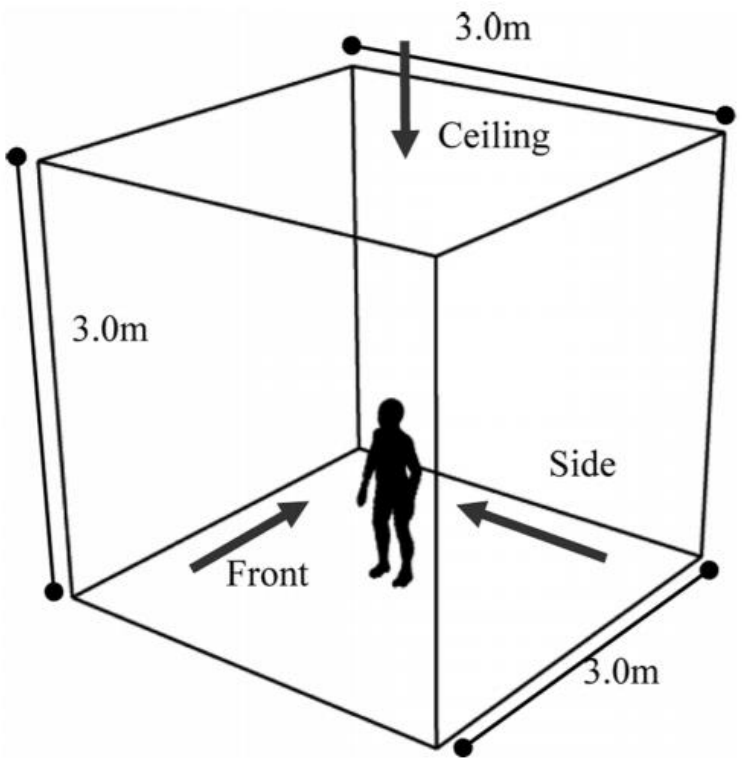

Figure 2.9: Analytical domain with CSP as described in works of Cong Li *et al*. (Cong & Kazuhide, 2012)

In literature this is a relatively new method and thus works to this regards are not as surplus as those seen in other methods described in preceding sections. Some of the earlier works in this area were carried out by Murakami *et al*. (Murakami, Kato & Zeng, 1997). They proposed

a two dimensional CSP prototype and analysed its heat exchange characteristics. Another work worth noting is works carried out more recently by Cong Li *et al*. (Li & Ito, 2014a). In their works, they conducted both numerical and experimental estimations of the convective heat transfer coefficient of the human body and made a comparison of both methods where a remarkable similarity of results are seen, with better accuracy seen in the results presented by the works of the numerical simulations. They made use of the commercial fluid flow software package ANSYS/FLUENT which would be employed in works carried out in this paper.

The method of numerical simulation is of primary interest in this thesis, and would thus be looked at in more detail in the chapters to follow.

2.3 PROBLEM STATEMENT

The works done in literature for computation of the convective heat coefficient of the human body typically presents the problem of accuracy of methodology used, especially when experimental procedures are employed. Some of the main problems encountered affecting the accuracy of the results include;

- Interference of the instrument with the air flow around the body and the temperature across the surface it is being attached to, as seen in works by de Dear et al where they employed use of the heat flux sensor as discussed in section 2.2.1 (de Dear *et al*., 1997).
- Failure to account for the total body surface area of the body in the investigation of the convective heat transfer area/coefficient (which as explained in section 2.1 is of great importance in convective heat transfer of the human body). This problem is seen in works of Chang *et al*., (Chang, Arens & Gonzalez, 1998) and that of Nishi *et al*., (Nishi & Gagge, 1970) as described in section 2.2.2. In their works, they employed the Naphthalene sublimation method.
- Failure to exactly replicate the experimental apparatus when changing experimental variables over time. This is seen mostly when live human beings are used as models during experimental computations. Here, measurements are conducted over a period of time of which accuracy is somewhat affected by the human subject as he/she has to remain as still as possible during the experimental period. This problem was encountered in works by Winslow *et al*, (Winslow, Herrington & Gagge, 1936) and that of Hardy *et al*, (Hardy &

Dubois, 1937), which employed the method of heat balancing. This is described in section 2.2.3.

- Failure to accurately differentiate the effects of convection and radiation during experiments by determining radiation and convective losses separately. This is also seen in works by Winslow *et al*, (Winslow, Herrington & Gagge, 1936) and that of Hardy *et al*, (Hardy & Dubois, 1937), which employed the method of heat balancing. This is described in section 2.2.3.

The use of the thermal manikins as described in section 2.2.4 for long has been an answer to most of the above mentioned problems. However, due to the experimental nature of procedures employing the thermal manikin, it is inherently prone to some degree of inaccuracy overall. Numerical Simulations as described in section 2.2.5, which employ the use of a computer simulated person builds on top of the experimental methodology of thermal manikins, but investigations are numerical as opposed to experimental, thus allowing for better accuracy.

In literature, works on Numerical Simulations investigating the convective heat transfer co-efficient are not as available as that for other methods for computing the convective heat transfer coefficient. Also, when present, they investigate specific body positions. Works in this paper take a closer look at the method of numerical simulation for the determination of the convective heat transfer coefficient.

2.4 OBJECTIVE OF THE WORK IN THIS PAPER

The overall goal of the works carried out in this paper is to investigate, develop and verify a framework for determining the convective heat transfer co-efficient from a cylindrical body that can easily be adaptable to more complex geometry – more specifically the human geometry. To do this, the following objectives are set out;

1. Perform a mesh generator analysis for both a stretched and equispaced mesh for different order upwinding schemes. This is done to verify the accuracy of the discretization schemes as well as inform our decisions going forward in modelling the fluid flow and heat exchange of a fluid over a representative cylindrical body.

2. Investigate the relationship between the body configuration and the convective heat transfer co-efficient under laminar and turbulent fluid flow. This is to enable analysis of effects of the human body configurations on the convective heat transfer co-efficient. To do this, we vary the orientation of the cylinder with respect to the incoming wind velocity to determine a relationship between the effective surface area and the convective heat transfer coefficient.
3. Propose a formula for the convective heat transfer co-efficient for both turbulent and laminar flow. To achieve this, we investigate the convective heat transfer co-efficient from a cylinder representative of the human body for laminar and turbulent flows. Thus, a geometry similar in height and surface area to that of a typical human model geometry as seen from literature. These dimensions and supporting argument for choice would be discussed in chapters to follow.

2.5 SCOPE AND FOCUS OF STUDY

There exists numerous amount of works investigating the convective heat transfer coefficient of a body for laminar flow as can be seen in the literature review (Section 2.1 and 2.2). Thus, though works on laminar flow are carried out in this paper, most of the focus is placed on turbulent flow.

3 RESEARCH THEORY

The underlying theory for the modelling of fluid flow as per works carried out in this thesis is described in this chapter. The chapter is started with an overview of numerical modelling, followed by a description of the numerical modelling procedure. The governing equations for the fluid flow problem are presented and discussed. The necessary boundary conditions are then explained. The chapter is brought to an end by an introduction to the mesh generator analysis, where we analyse what possible methods of discretization are available for use with regards works carried out in this thesis.

3.1 NUMERICAL MODELLING

For simulation of fluid flow using computational fluid dynamics (CFD), there exists numerous commercial CFD software packages to aid the study of fluid flow and heat transfer as is the case in this thesis. The governing equations of the fluid flow being partial differential equations (PDE's) can become very complex and complicated to solve analytically. This complexity also makes solving analytically prone to accuracy problems if at all attempted. The solution to this is to use CFD software packages which substitute the PDE's with a system of algebraic equations easy to solve using the CFD packages. Also, in comparison to experimental methods in solving fluid flow and heat transfer problems, Numerical procedures shows greater advantages as experimental methods tend to be very expensive and time consuming.

There exists three main elements in most commercial CFD codes (Versteeg & Malalasekera, 2007);

1. Pre-Processor Element: This element of the package deals with;
    - Geometry Definition of the Computational Domain
    - Grid/Mesh Generation: that is, the subdivision of the domain into smaller, non-overlapping sub-domains (control volumes)
    - Modelling of the fluid flow phenomenon as well as fluid Properties
    - Specification of boundary conditions

2. Solver Element: This element comprises primary of;
    - Integration of the fluid flow governing equations for the computational domain
    - Discretisation of the governing equations
    - Solution of the resulting algebraic equations
3. Post – Processing Element: At this stage, a majority of the computation has already been carried out. It basically involves:
    - Discretized domain geometry
    - Solution visualization
    - Various plots and particle tracking analysis

While using CFD packages, the numerical solutions to the governing equations discussed in section 3.3 is obtained through the use of any of the following numerical approximation schemes;

- The Finite Difference Method (FDM)
- The Finite Element Method (FEM)
- Spectral method
- The Finite Volume Method (FVM)

The commercial CFD software package used is ANSYS – FLUENT 16.0, a well-established commercial CFD software. As with most commercial CFD codes, ANSYS – FLUENT uses the Finite Volume Method (FVM) for its "Solver Element" to obtain solutions to the governing equations. The FVM methods is explained in later sections of this chapter.

3.2 NUMERICAL MODELLING PROCEDURE

The CFD software package used (ANSYS-FLUENT) comes fully equipped with an integrated workbench that allows for all the steps as listed in section 3.1 to be carried out on a single software using different software tools/modules. This is made possible as data and information on the software can be passed between the different tools required at different stages of the fluid flow modelling and simulation. This process is described in Figure 3.1.

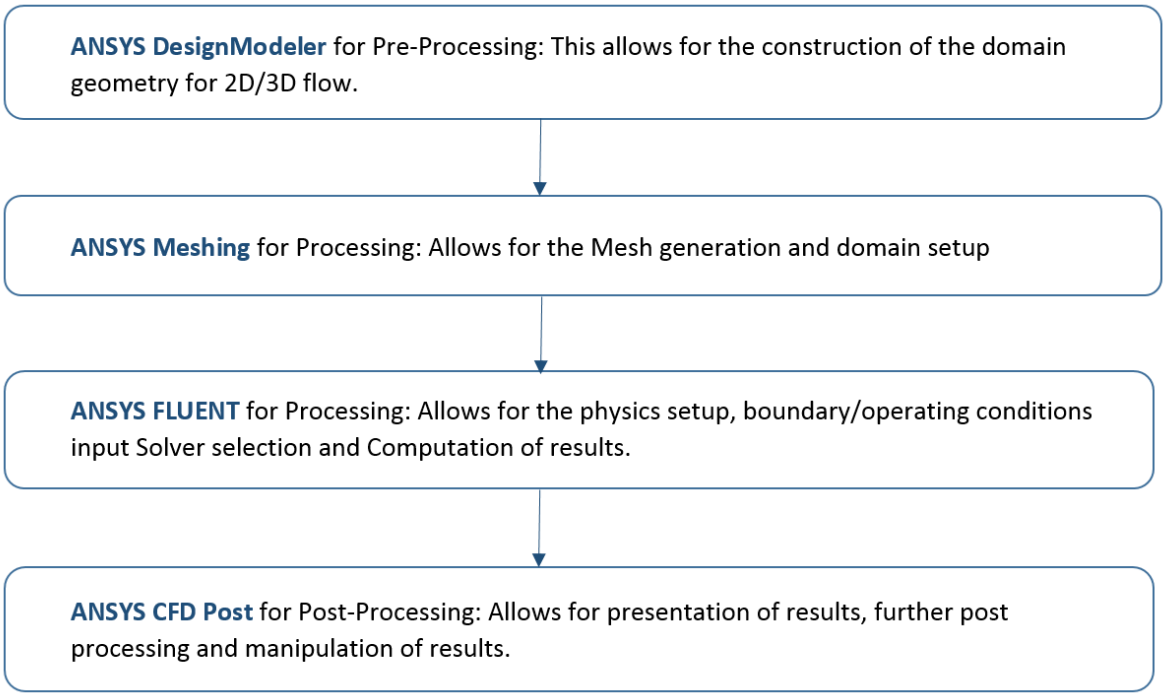

Figure 3.1 Numerical Modelling Procedure using the ANSYS Software package

3.2.1 CREATION OF GEOMETRICAL MODELS AND COMPUTATIONAL DOMAIN

This is the first stage of the simulation and involves the use of the ANSYS DesignModeller for geometry creation. It is a parametric feature-based 3D modeller similar in functionalities to other more familiar packages for 2D/3D computer aided design (CAD) modelling packages like Solidworks, AUTOCAD etc. Once the geometry is successfully modelled, it is then transferred to the ANSYS Mesh tools.

3.2.2 MESH GENERATION

This is the first stage of the pre-processing. This is carried out using the ANSYS Meshing tool integrated on the ANSYS workbench. This allows for the information from the ANSYS DesignModeller to be passed onto the ANSYS Meshing tool for pre-processing. Here, the computational domain is subdivided into control volumes/cells. These control volumes/cells are basically just subdivisions of the computational domain into a finite number of discrete, non-overlapping sub-domains. The pre-processing meshing stage allows the selection of the appropriate meshing schemes and techniques to be used. This depends mostly on whether the model is 2D or 3D. The cells types available for 2D meshes are the triangular and the

quadrilateral meshes, while for 3D meshes we have the hexahedral, tetrahedral, pyramid, wedge and polyhedral cells. These cells types are shown in figure 3.2.

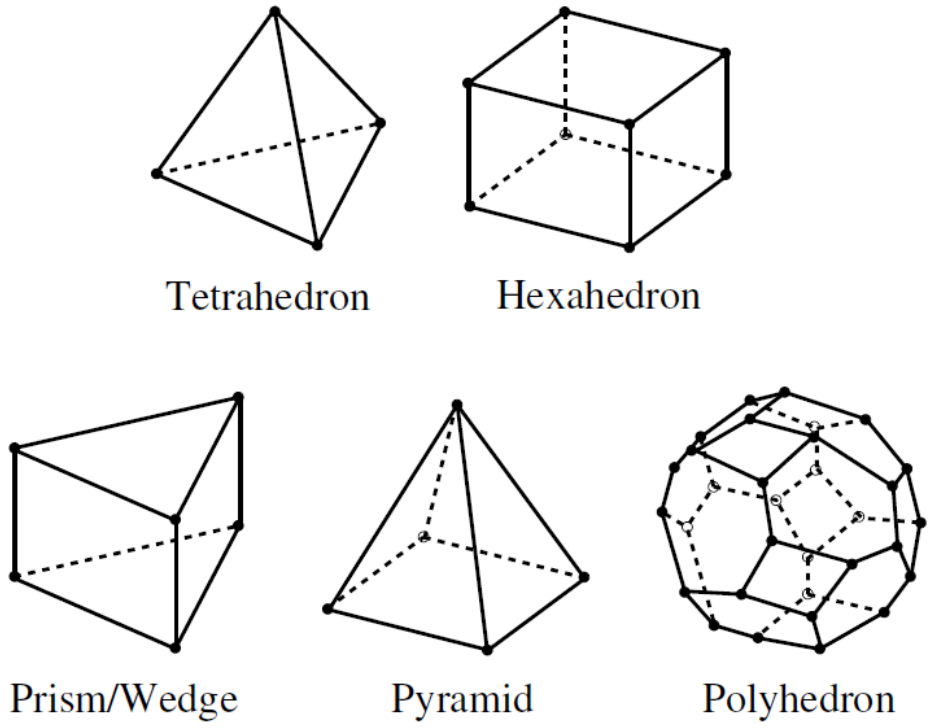

Figure 3.2: 3D Cell Types for Meshing (Ansys, 2009)

For 2D and 3D meshing, the complexity of the geometry determines the type of mesh cells to be used. For 3D meshing, the meshing can either be structured or unstructured. Structured meshes consisting of quadrilateral or hexahedral mesh tend to be more time consuming to create than their unstructured mesh counterparts which uses triangular or tetrahedral mesh cells. This is primarily due to the fact that quadrilateral or hexahedral mesh cells generally force cells to be placed in regions where they are not needed (experienced especially in complex geometries), while triangular or tetrahedral mesh cells or a combination of the two allows for clustering of cells in selected regions of the flow domain (Ansys, 2009).

The more mesh cells used in the grid, the finer the grid, and the more computational expensive the meshing would be. For this reason, for an optimal mesh, finer mesh cells are used in regions of large variations in the geometry, allowing coarser meshes to be used where there are relatively fewer point to point variations in the geometry (Versteeg & Malalasekera, 1995). To accomplish this, a technique known as “Inflation” in the ANSYS “Mesh” is used.

Basically, thin cells adjacent to the boundaries are generated to enable a more accurate capture of wall surfaces adjacent to boundary layers. These cells are created by “inflating” from the surface mesh into the volume (Ansys, 2016b). As at the time of writing this thesis, there exists 5 main options for inflation on the Mesh of the ANSYS software;

- Smooth Transition; this maintains a ‘smooth’ volumetric growth between each adjacent layers. This is displayed in Figure 3.3.

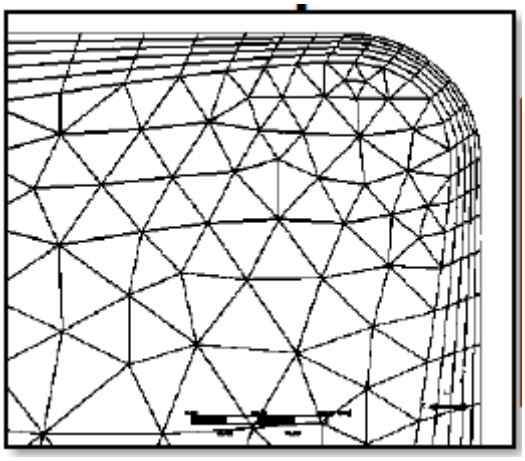

Figure 3.3: Smooth Transition Inflation

- First Layer Thickness; here, the height of the first cell is maintained throughout. Shown in Figure 3.4.

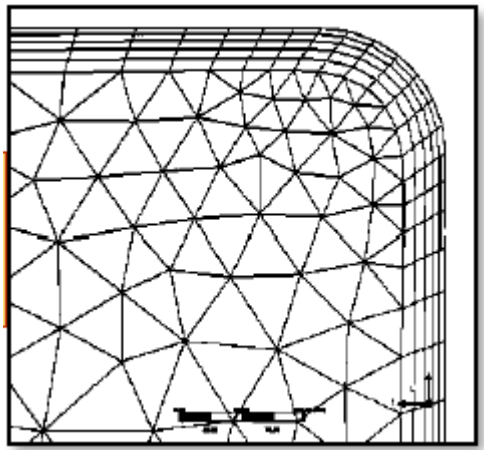

Figure 3.4: First Layer Thickness Inflation

- Total Thickness; here, the total height of the inflation layer is predetermined by the user. Shown in Figure 3.5.

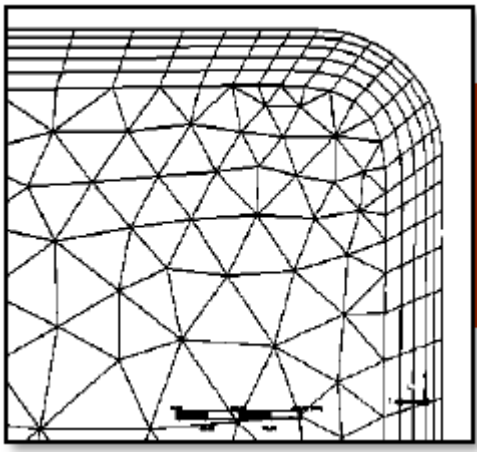

Figure 3.5: Total Thickness Inflation

- First Aspect Ratio; here, the height of the inflation layers are defined by the aspect ratio of the inflations extruded from the inflations base. Shown in Figure 3.6.

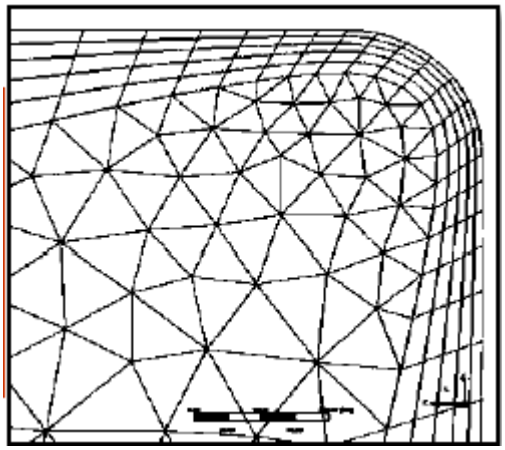

Figure 3.6: First Aspect Ratio Inflation

- Last Aspect Ratio; here, the height of the inflation layers are defined by the predetermined first layer height, the aspect ratio controls and the maximum layers. Shown in Figure 3.7.

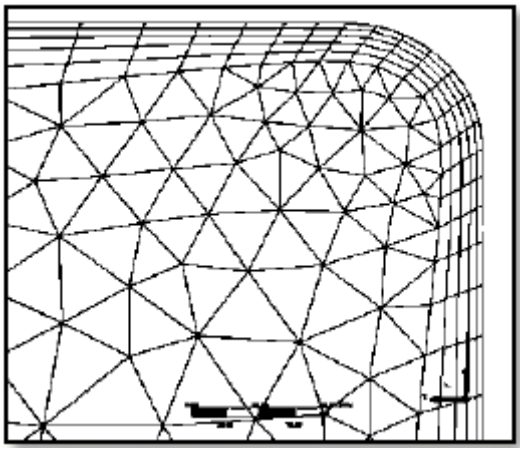

Figure 3.7: Last Aspect Ratio Inflation

The smooth transition inflation is used for works carried out in this thesis.

3.2.3 SOLUTION AND POST-PROCESSING

Once the Mesh is successfully generated, it is exported to ANSYS FLUENT where the physics is setup, the boundary/operating conditions are set, the Solver is selected, and computation is carried out. For works in this thesis, most of the time in each simulations is spent during the solution computation. This is due to the time dependent nature of the simulations, as it takes a considerable amount of time for each computation to be carried out. Once the computation is done, the results are exported to CFD Post where they are analysed and any necessary post processing and manipulation is carried out, for example analysis of the simulation flow fields etc.

3.3 GOVERNING EQUATIONS

The non-linear, partial differential equations presented below are representative mathematical statements of the conservation law of physics that describes the characteristics of fluid and heat flow modelling.

3.3.1 CONSERVATION OF MASS

$$\frac{\partial \rho}{\partial t} + \nabla \cdot \left(\rho \vec{V}\right) = 0 \qquad 3.1$$

Where ρ = fluid density

$\vec{V}$ = the velocity vector of the fluid

$$\nabla = \frac{\partial}{\partial x} + \frac{\partial}{\partial y} + \frac{\partial}{\partial z}$$

The law of conservation of mass states that the mass of a fluid continuum is conserved and its general form is represented by equation 3.1 (Tannehill, Anderson & Pletcher, 1997). This is also referred to as the continuity equation which is used for both a compressible and incompressible fluid continuum.

From equation 3.1, the first term of the left of the equation ($\frac{\partial \rho}{\partial t}$), is the rate of increase of density in the control volume, while the second term ($\nabla \cdot \left(\rho \vec{V}\right)$) is the convective term, which is the rate of mass flux passing out the surface of the control volume.
When we consider steady incompressible flow, the density (ρ) is constant, thus, we re-write equation 3.1 as shown in equation 3.2.

$$\nabla \cdot \left(\rho \vec{V}\right) = 0 \qquad 3.2$$

3.3.2 CONSERVATION OF MOMENTUM

The conservation of momentum states that, the rate of change of momentum equals the sum of forces on a fluid particle. This is a derivative of Newton's second law which states that the rate of change of momentum of a fluid particle is equal to the sum of forces on the fluid particle.

$$\rho \frac{DV}{Dt} = \rho g - \nabla P + \frac{\partial}{\partial x_i}\left[\mu\left(\frac{\partial u_i}{\partial x_j} + \frac{\partial u_j}{\partial x_i}\right) - \frac{2}{3}\delta_{ij}\mu\frac{\partial u_k}{\partial x_i}\right] \qquad 3.3$$

Where g = vector for acceleration due to gravity

P = total pressure

x = spatial coordinate

μ = the dynamic viscosity

u_i, u_j, u_k = the components of velocity vector $\vec{V}$

x_i, x_j, x_k = the components of the position vector

δ_{ij} = the Kronecker delta function

Mathematically, the conservation of momentum can be represented by equation 3.3 (Tannehill, Anderson & Pletcher, 1997), also known as the Navier-Stokes equations.

For incompressible flow, the viscosity coefficient is assumed constant, thus, we re-write equation 3.3 as shown in equation 3.4.

$$\rho \frac{DV}{Dt} = \rho g - \nabla P + \mu \nabla^2 V \qquad 3.4$$

Where, $\nabla^2 = \frac{\partial^2}{\partial x^2} + \frac{\partial^2}{\partial y^2} + \frac{\partial^2}{\partial z^2}$

3.3.3 ENERGY EQUATION

The energy equation is an expression of the first law of thermodynamics, which tells us that the rate of change of energy of a fluid particle is equal to the rate of heat addition to the fluid particle plus the rate of work done on the particle. The general form of the energy equation is given by equation 3.5 (Tannehill, Anderson & Pletcher, 1997).

$$\rho \frac{Dh}{Dt} = \frac{DP}{Dt} + \frac{DQ}{Dt} - \nabla q + \emptyset \qquad 3.5$$

Where P = Pressure

Q = Heat produced from external sources

q = heat transferred = $-k\nabla T$

Ø = dissipation function involving viscous stresses as described in equation 3.6.

h = enthalpy, expressed as $\left(e + \frac{P}{\rho}\right)$, where 'e' is the internal energy peer unit mass.

$$\emptyset = \mu\left[2\left(\frac{\partial u}{\partial x}\right)^2 + 2\left(\frac{\partial v}{\partial x}\right)^2 + 2\left(\frac{\partial w}{\partial x}\right)^2 + \left(\frac{\partial v}{\partial x} + \frac{\partial u}{\partial y}\right)^2 + \left(\frac{\partial w}{\partial y} + \frac{\partial v}{\partial z}\right)^2 + \left(\frac{\partial u}{\partial z} + \frac{\partial w}{\partial x}\right)^2\right] + \lambda\left(\frac{\partial u}{\partial x} + \frac{\partial v}{\partial y} + \frac{\partial w}{\partial z}\right)^2 \qquad 3.6$$

Once again, considering incompressible flow assuming constant thermal conductivity and neglecting the effects of heat produced by external agencies, the viscous dissipation becomes negligible. Equation 3.5 thus reduces to:

$$\frac{DT}{Dt} = \alpha \nabla^2 T \qquad 3.7$$

Where, $\alpha = \frac{k}{\rho C_p}$ is the thermal diffusivity and C_p is the specific heat capacity

3.4 FINITE VOLUME METHOD (FVM)

The FVM is a method used in obtaining numerical solutions to the governing equations. For the FVM, the integral form of the conservation equations is discretised directly in the physical domains. Here, the computational domain is further divided into control volumes, which are basically small sub-domains. The governing equations are then discretised into a system of algebraic equations for each control volume and solved using an iterative method. The result of this is an approximate value of each variable at a specific point in the computational domain. Thus, enabling the derivation of the complete behaviour of the flow being analysed (Jiyuan, Guan & Chaoqun, 2013).

3.5 PRESSURE – VELOCITY COUPLING

It can be shown by discretising the momentum equation (equation 3.4) that there exists a linear dependence of velocity on pressure and vice-versa. The pressure velocity coupling thus refers to the numerical algorithm used to derive an equation for pressure when using a pressure based solver. This is done by using a combinations of the momentum and continuity equation.

In ANSYS – FLUENT, pressure – velocity coupling can be achieved by any of the available four segregated algorithm it provides (ANSYS, 2003). These include:

1. The semi-implicit method for pressure linked equations (SIMPLE),
2. The semi-implicit method for pressure linked equations (SIMPLEC),
3. The pressure-implicit with splitting of operators (PISO)
4. Coupled.

In this thesis, the SIMPLE algorithm was used. This choice was based primarily on its advantage of being able to handle problems associated with non-linearity in the set of governing equations as well as the pressure-velocity linkage by making use of an iterative solution approach.

In the SIMPLE scheme, to solve the momentum equation, a hypothetical pressure field is used to calculate pressure and velocities for an incompressible flow. This is followed by deducing a pressure correction equation from the continuity equation, which is solved to obtain a pressure correction field, which in turn is used to update the pressure and velocity fields. These hypothetical fields are improved progressively through an iterative process until convergence is achieved for both the velocity and pressure fields (Jiyuan, Guan & Chaoqun, 2013). This iterative process is the basis of the SIMPLE algorithm and is described in Figure 3.8.

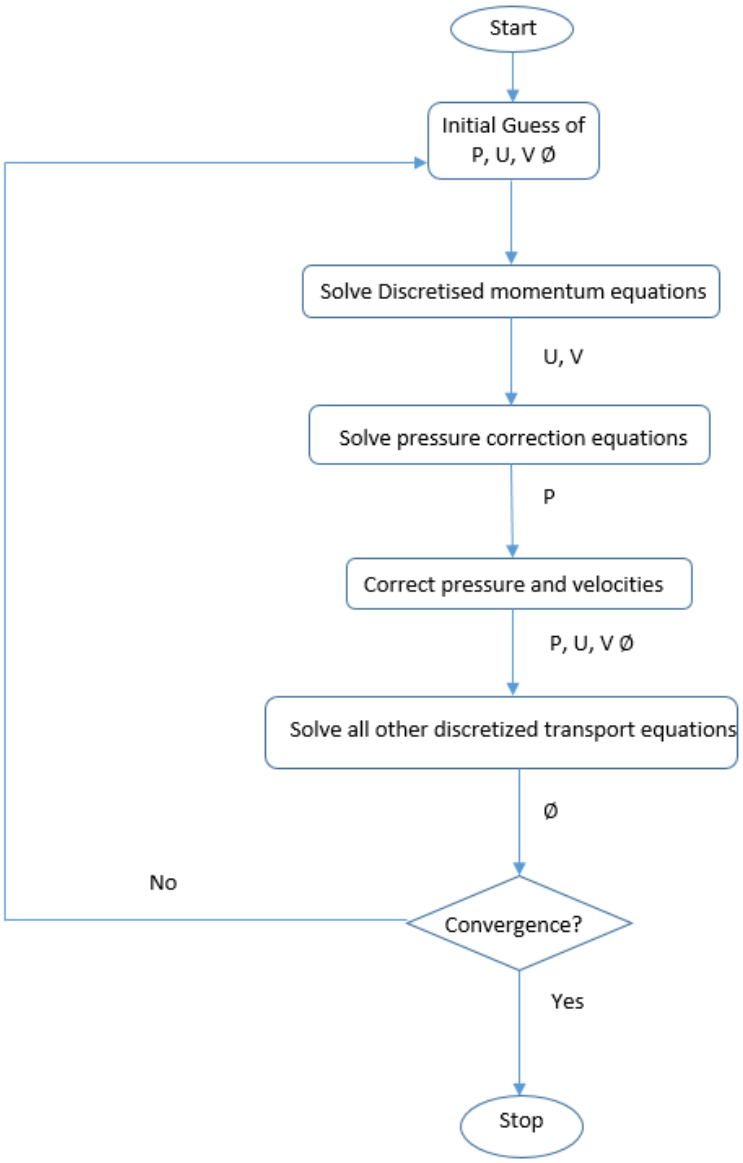

Figure 3.8 The Simple Algorithm

3.6 MODELLING OF FLUID FLOW AND HEAT TRANSFER

Numerical simulations enable resolution of only motions of scales larger than the mesh size. While this can be considerably managed for laminar flow, it becomes a problem for turbulent flow as a multitude of scales are experienced in time and space. Eddies in turbulent flow are characterized by the transportation of energy from large eddies to smaller eddies and then to heat through the action of viscosity (Cong, 2013). This leaves the upper bound of the length scale to be determined by the geometric boundary and the lower bound to be determined by the viscosity dissipative scales. Thus, for example, for ventilation flow, the smallest length scale of the mesh may be of order 0.1mm and the larger length scale the dimension of the ventilated room.

Direct Numerical Simulation (DNS) – which provides a three dimensional, time dependent solution of the Navier-Stokes equation – can be employed here in solving the whole spectrum of turbulent scales. This is because it allows for solving non-linear differential equations with full resolution down to the smallest mesh scale with minimal modelling approximation if any (Cong, 2013). Even at that, the most useful results from the DNS approach of solving the Navier-Stokes equation is obtained by time-averaging the instantaneous quantities as it lies in the mean field. DNS simulations employ costly simulation resources, and are thus not common for industrial engineering application (Versteeg & Malalasekera, 2007). This model is of no interest in this thesis.

Another approach would be to use Large Eddy Simulation (LES) models. Here, unsteady Navier-Stokes equations are space filtered to sieve through larger eddies, while rejecting smaller eddies. In other words, small scales are filtered out so as to make a relatively coarse mesh that is usable for the numerical resolutions of larger scales. This technique is typically considered for CFD problems with complex geometry (Versteeg & Malalasekera, 2007). As we are dealing with a simple cylindrical geometry, this would not be explored in this thesis.

An alternative to the DNS model and the LES model is the use of statistical approaches of the Reynolds-Averaged Navier Stokes Equation (RANS). In the RANS approach, time-averaging is also practised to average out all stochastic turbulent fluctuations. This averaging process introduces extra terms due to the interactions between various turbulent fluctuations (Versteeg & Malalasekera, 2007). These new unknowns are modelled using different

turbulence models. There are two main general forms of the RANS turbulence model equations used to solve extra terms as described extensively by Cong (Cong, 2013);

1. The One Equation RANS: in this model, there is no calculation of the length scale related to the local shear layer thickness of the model. In addition to that, the turbulence model used here is local and thus equations at a given point have no influence on equations at a different point in the model, thus making the model insensitive to free stream values. This is extensively described by Spalart *et al*. (Spalart & Allmaras, 1992) in their well cited report on the one-equation turbulence model.
2. The Two Equation RANS: this is regarded as one of the simplest "complete turbulence models" in literature. Here, two separate transport equations allow both the turbulent viscosity and length scales to be independently computed. These models see the most use in engineering applications today. Some examples of the two-equation RANS models include;
    - The Standard $k-\varepsilon$ model
    - The low Reynolds type $k-\ \varepsilon$ model. This is typically used for transport processes in very close proximity to the model surfaces as described in works published by Abe *et al* (Abe, Kondoh & Nagano, 1994).
    - The Menter's Shear Stress Turbulence (SST $k-\ \omega$) Model which has been proven to account for the transport of turbulent shear stress (Menter, Kuntz & Langtry, 2003).
    - The v^2-f model which estimates the turbulence viscosity by in-cooperating the effects of anisotropy on near wall turbulence

The Shear-Stress Transport (SST) $k-\omega$ model of the two equation RANS model is considered a more accurate and reliable model for a wider class of flow in literature. It was first proposed in works by Menter (Menter, 1993). The main difference between these models is that in the Menter's SST k-ω model, the specific dissipation (ω) is used rather than the dissipation rate ε as with the Low Reynolds Type $k-\varepsilon$ model and the Standard $k-\varepsilon$ model. The specific dissipation rate ω, is however basically the ratio of ε - k shown by equation 3.8 (Versteeg & Malalasekera, 2007).

$$\varepsilon = k\omega \qquad 3.8$$

Where k = the turbulent kinetic energy.

The Menter's SST $k-\omega$ model uses a blending/damping function to ensure that the model equations are suitable for both the near-wall and far-field zones. As a matter of fact, it uses the standard $k-\varepsilon$ models in fully turbulent regions and the transformed $k-\varepsilon$ to $k-\omega$ model in near wall regions. It also incorporates modifications to account for turbulent shear stresses. These features make the model reliably accurate for a wide variety of flows. The SST $k-\omega$ model would be explored in this thesis via the function in the ANSYS FLUENT commercial code. The transport equation of the SST $k-\omega$ model is described in **Figure 3.9**.

Rate of change of k or ω (I)	+	Transport of k or ω by convection (II)	=	Transport of k or ω by turbulent diffusion (III)	+	Rate of production of k or ω (IV)	-	Rate of dissipation of k or ω (V)

$$\underbrace{\frac{\partial(\rho\omega)}{\partial t}}_{\text{(I)}} + \underbrace{\operatorname{div}(\rho\omega\mathbf{U})}_{\text{(II)}} = \underbrace{\operatorname{div}\left[\left(\mu+\frac{\mu_t}{\sigma_{\omega,1}}\right)\operatorname{grad}(\omega)\right]}_{\text{(III)}} + \underbrace{\gamma_2\left(2\rho S_{ij}\,.\,S_{ij}-\frac{2}{3}\rho\omega\frac{\partial U_i}{\partial x_j}\delta_{ij}\right)}_{\text{(IV)}} - \underbrace{\beta_2\rho\omega^2}_{\text{(V)}} + \underbrace{2\frac{\rho}{\sigma_{\omega,2}\omega}\frac{\partial k}{\partial x_k}\frac{\partial\omega}{\partial x_k}}_{\text{(VI)}}$$

Figure 3.9: Transport equation of the SST $k-\omega$ model (Versteeg & Malalasekera, 2007)

A look at **Figure 3.9**, we see that there is an extra term as marked in the red box. This extra term comes about by the transformation of the ε – equation of the $k-\varepsilon$ model to the ω – equation of SST $k-\omega$ model using the $\varepsilon = k\omega$ transformation (Versteeg & Malalasekera, 2007).

To leverage the SST $k-\omega$ model in the ANSYS - FLUENT software package, the values of k *and* ω are to be pre-computed while all other values are either derived from this or constants. The computed values of k *and* ω are then entered as boundary conditions.

3.7 BOUNDARY CONDITIONS

3.7.1 INLET BOUNDARY CONDITIONS

$$k = \frac{3}{2} * (U * 0.01 * TI)^2 \quad 3.9$$

$$\omega = C_\mu * \frac{k^{0.5}}{l} \quad 3.10$$

Where TI = Turbulence intensity. For works in this paper, this would be supplied

l = turbulence length of scale. This is approximated as the characteristic length of the flow opening. For example, for a cylinder in a rectangular domain, the turbulence length of scale would be the length of the largest side of the opening rectangle for incoming flow.

C_μ = this is an empirical constant specified in the turbulence model as employed by the Ansys Code. It is given as approximately 0.09.

For the SST $k - \omega$ two-equation RANS model which is to be used in this thesis, the velocity, temperature and turbulent transport quantities for the inlet boundary conditions are computed using the formulas seen in equations 3.9 and 3.10 above, as described in the Ansys theory guide (ANSYS, 2003).

3.7.2 NEAR WALL TREATMENT

In modelling fluid flow, the presence of walls (walls of the surrounding domain for example) significantly affect the modelling process. For one, at the walls, the condition of no-slip has to be satisfied for typical fluid flow as it applies to works in this thesis. This in turn affects the mean velocity of the flow at the walls. At close to the walls, tangential velocity fluctuations is reduced by viscous damping and towards outer parts of the near-wall region, production of turbulent kinetic energy due to large gradients in mean velocity rapidly amplify the turbulence (ANSYS, 2003). Thus accurate representation of flow in near wall regions significantly affects the prediction accuracy of wall bounded flows, especially of turbulent flows.

For modelling of flow, it has been proven in literature that the near-wall region of turbulent flow can be subdivided into three layers (ANSYS, 2003);

- The Viscous Sublayer: being the innermost layer closest to the wall, here, flow is almost laminar and momentum heat/mass transfer is determined chiefly by molecular viscosity
- The Interim Layer: here, the effects of turbulence and molecular viscosity have a somewhat equal role in describing the fluid flow.
- The Fully Turbulent Layer: this is the furthest layer from 'near-wall'.

Figure 3.10, depicts these 3 layers on semi log co-ordinates.

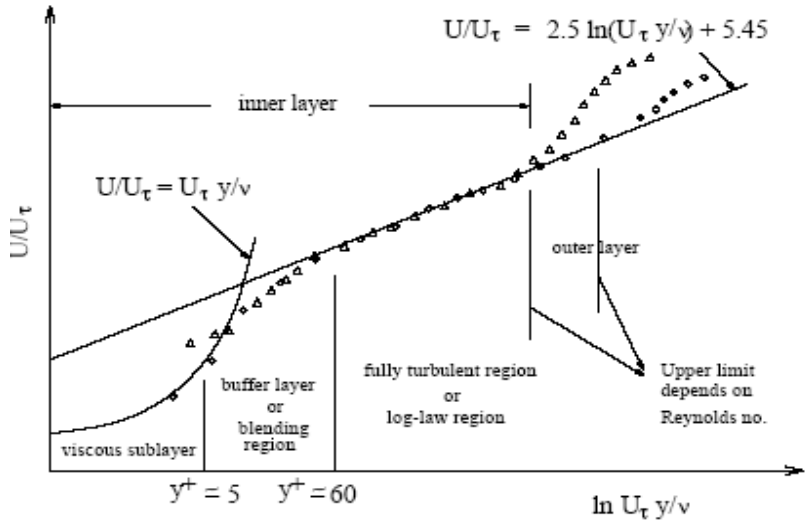

Figure 3.10: Subdivision of Near Wall Region (ANSYS, 2003)

The software package used for modelling provides us two broad options. These are;

1. The Wall Function Approach: here, the viscosity affected region is modelled using a wall function as opposed to being resolved. The viscosity affected region is 'bridged' between the wall and the fully-turbulent flow using these wall-functions. A schematic taken off the Ansys theory guide is show in in Figure 3.11. This is very advisable for flows with High-Re numbers, and is thus mainly available for High-Re turbulence models or similar models. Though economical and of reasonable accuracy, it is not at all advised for low-Reynolds-number flow (ANSYS, 2003).
2. Near-Wall Model Approach: here, the turbulence models are directly modified to enable mesh resolution of the viscosity affected regions all the way to the walls incorporating the viscous sub layer.

3. Enhanced Wall Treatment: here, FLUENT combines the method of near-wall treatment with enhanced wall functions. It is described in the fluent theory guide that this is only possible if the near-wall mesh is fine enough to enable resolution of the laminar sub layer, having a value typically of $y^+ \approx 1$with reference to Figure 3.10 above (ANSYS, 2003).

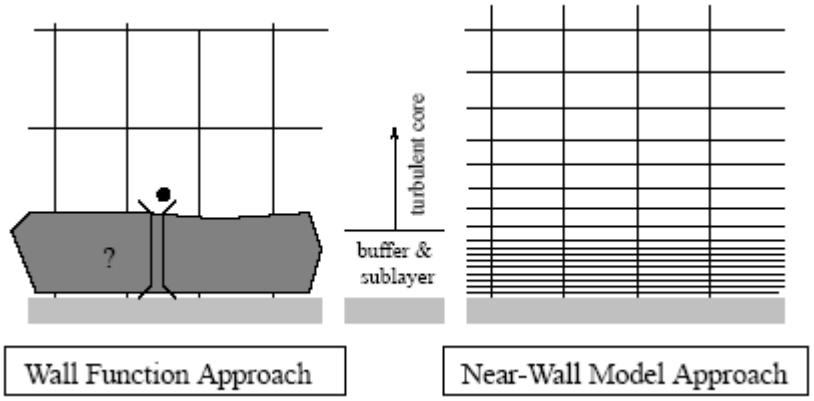

Figure 3.11: Depiction of Near Wall Treatments in Ansys (ANSYS, 2003)

The method of enhanced wall treatment present literally a scenario of best of both world in the context of works carried out in this thesis, especially due to the fact that we are not necessarily dealing with really high Reynolds turbulence model as described in previous sections. In literature as well, it is seen to be the choice of different authors who conducted similar numerical models, although based on human models. These are also seen to be the "wall-treatment" of choice in literature as seen in the works of Cong Li *et al* (Cong & Kazuhide, 2012), Li *et al* (Li & Ito, 2014a). Also, influencing the decision of what near-wall approach to consider, the SST $k-\omega$ model chosen in previous sections of this chapter (section 3.6) as the turbulence model of choice were designed to be applied throughout the boundary layer as long as the resolution of the mesh is sufficiently fine as described for enhanced wall treatment.

The enhanced wall treatment method of the ANSYS FLUENT software would be employed for works in this paper.

3.7.3 OUTFLOW BOUNDARY CONDITIONS

To model the boundary conditions at the outflow, we acknowledge that the flow velocity and pressure at the flow outlets are not known prior to modelling the fluid flow. For scenarios such as this, it is given in the FLUENT guide that outflow boundary conditions are not to be

defined and FLUENT extrapolates the required information from the interior during computation (ANSYS, 2003). Thus, no outflow boundary condition was specified in the Fluent solver.

3.8 MESH GENERATOR ANALYSIS

The discretization of the fluid flow partial differential governing equations into algebraic equations constitutes the basis of the numerical simulations. The resulting algebraic equations relate the values of the independent variables at the nodes of the computational grid. There exists a number of schemes used in the discretization of the governing equations. One of the objectives of this thesis is to present a mesh generator analysis, which basically involves the analysis of these numerical schemes.

To perform a mesh generator analysis and thus discuss the various discretization schemes consider the convection – diffusion equation which describes a steady inviscid Newtonian flow in a straight tube of unit depth and height

$$S(x) = -\frac{\partial u_x T}{\partial x} + \frac{\partial}{\partial x}\left(k\frac{\partial T}{\partial x}\right) \qquad 3.11$$

Where $S(x)$ = Source term = 0

k = thermal conductivity

T = Scalar quantity temperature 'T'

For the tube of constant cross sectional area 'A', and a steady inviscid flow at speed u_x, Figure 3.12 describes a mesh structure that could be used to solve the problem definition above. The mesh takes into consideration beta factors for increasing/decreasing spacing between each consecutive node along the channel. Boundary conditions for temperature are known and denoted as T_{in} and T_{out}. Figure 3.12 describes how the tube is split into N number of nodes both for the equi-spaced and stretched scenarios.

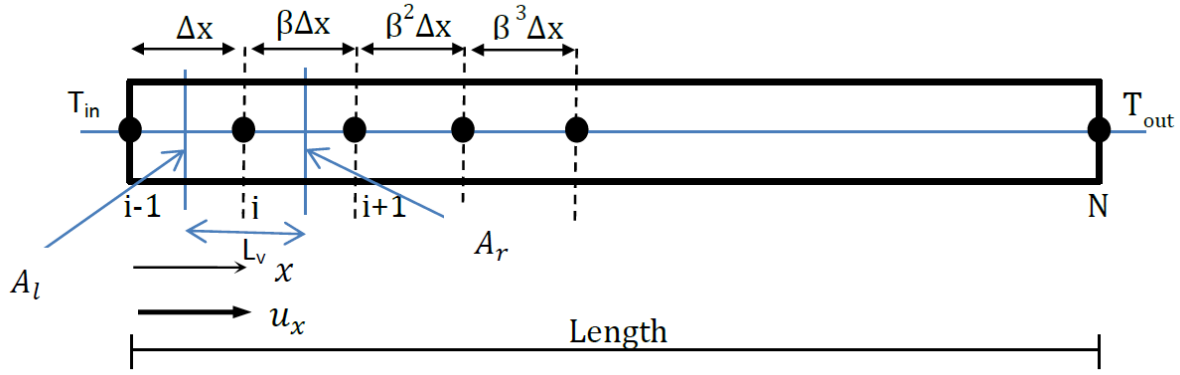

Figure 3.12: Describing the tube split into N nodes with a stretching factor ß

Where; Lv = Control volume which changes for the stretched mesh. = $\frac{x_{i+1} - x_{i-1}}{2}$

Thus, for the equi-spaced mesh, all control volumes simply equals 'Δx' as ß = 1. For the stretched mesh however, the control volume changes as one might expect, increasing as ß increases for ß > 1, and vice versa. This thus creates the need for a Δx value that changes as ß changes. This can be derived by realising that the summation of the ΔL_v is a geometric progression. Thus;

$$\Delta x = \frac{\text{Length}}{1 + \beta + \cdots + \beta_{N-2}}$$

Now, considering the control volume, we have that;

Control volume = V_N = L_v * A.

Other terms to note are;

A_l = Control area of the left face of node i

A_R = Control area of the right face of node i

These would be used in discretizing the governing equation explained next.

3.8.1 THE DIFFUSIVE TERM

The finite volume method is used in discretizing the equations. The diffusive term is first converted into weak form. Greens theorem was then applied and the integral assessed. The value for volume at each node, as described in previous paragraphs was used and the following final equation for the diffusive term is determined:

$$\frac{\partial}{\partial x}\left(k\frac{\partial T}{\partial x}\right) \approx \frac{1}{V_N}\oint_{A_N} k\frac{\partial T}{\partial x}n_x dA$$

$$\approx \frac{1}{V_N}\left[-k\frac{\partial T}{\partial x}|_L + k\frac{\partial T}{\partial x}|_R\right]\cdot A$$

$$\approx \frac{1}{L_N * A}\left[-k\frac{\partial T}{\partial x}|_L + k\frac{\partial T}{\partial x}|_R\right]\cdot A$$

$$\approx \frac{k}{L_V}\left[\frac{T_{i-1} - T_i}{\Delta x_L} + \frac{T_{i+1} - T_i}{\Delta x_R}\right]$$

$$\frac{\partial}{\partial x}\left(k\frac{\partial T}{\partial x}\right) \approx \left(\frac{k}{L_V}\right) * \_T_{i-1} + \left(\frac{k}{L_V * \Delta x_R}\right) * T_{i+1} - \left(\frac{k}{L_V} * \left(\frac{1}{\Delta x_R} - \frac{1}{\Delta x_R}\right)\right) * T_i \qquad 3.12$$

The above method used in discretizing the diffusive term is known as the First Order Upwinding Method. It basically uses one upstream node along the mesh as described in Figure 3.12 in addition to the properties on the respective boundaries of the cell and uses that in computation at the centre of the cell. This form of first order Upwinding is called the Central Difference Method (CDM) (Versteeg & Malalasekera, 2007). The central difference methods works for both first and higher order upwind methods of discretising the diffusive term. This is not the case with the convective term, as discussed next.

3.8.2 THE CONVECTIVE TERM

As with the diffusive term, one might be tempted to make use of the first order central difference method to discretize the convective term of equation 3.12. While this would work for first order Upwinding methods, it would not work for higher Upwinding methods. Using the CDM to discretise the convective term as done with the diffusive term in the previous section, it can be shown that

$$\frac{\partial u_x T}{\partial x} \approx -\frac{1}{V_N} * \left[-T_L u_x A_L + T_R u_x A_R\right]$$

$$\frac{\partial u_x T}{\partial x} \approx \frac{u_x}{L_V}\left[T|_L - T|_R\right] \qquad 3.13$$

The above is done using the first order CDM. Now, to show that the previously describe mesh shown in Figure 3.12 would not be able to discretize the convective term for higher order upwinding, Figure 3.13 is introduced, which describes a mesh on which the higher order Upwinding method would be used to discretise the convective term.

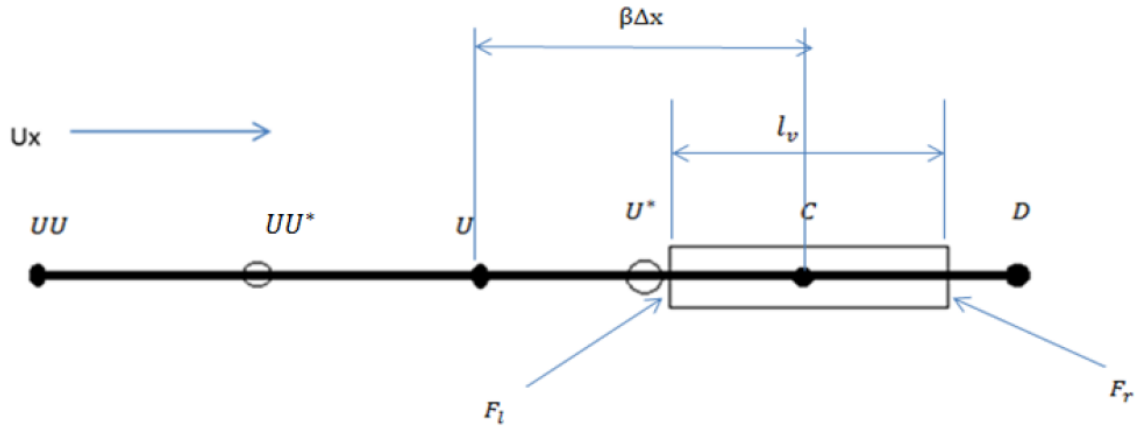

Figure 3.13: Describing the tube split for higher order discretisation

Using Figure 3.13, once again the convective term is converted to weak form and discretised using the kappa 'κ' scheme, where the choice of 'κ' in the equations to follow determines the accuracy of the scheme.

Considering node C,

Let

$$W_1 = {}^{(1+k)}/_{4} \tag{3.14}$$

$$W_1 = {}^{(1-k)}/_{4} \tag{3.15}$$

Where,

k = 1 for the Central Difference Scheme (CDS)

k = $1/2$ for the Quadratic Upwind Interpolation (QUICK Scheme)

k = 1/3 for the Cubic Upwind Interpolation (CUI Scheme)

$$-\frac{\partial}{\partial x}(u_x T)|_C = -\frac{u_x}{V}\left[T|_{f_L} + T|_{f_R}\right]\cdot A$$

$$-\frac{\partial}{\partial x}(u_x T)|_C \approx \frac{u_x}{l_v}\left[T|_{f_L} + T|_{f_R}\right] \tag{3.16}$$

For brevity, the step by step discretization of equation 3.16 is shown in appendix A0.

Addition of the discretised convection and diffusion equation would lead to discretised form of the governing equation of the flow (the convection – diffusion equation). Upon addition and rearranging of the discretized equations, a diagonal matrix of the form A.T = b results from the temperature difference co-efficient.

Where;

C = Matrix Diagonal = coefficient of T_i = $\left(\frac{k}{L_V} * \left(\frac{1}{\Delta x_R} - \frac{1}{\Delta x_R}\right)\right)$

L = Left of Matrix Diagonal = coefficient of T_{i-1} = $\left(\frac{k}{L_V}\right)$

R = Right of Matrix Diagonal = coefficient of T_{i+1} = $\left(\frac{k}{L_V * \Delta x_R}\right)$

Thus, solving the combined equation at every node from 1 to N, we get a matrix of the form A.T = b,

$$\therefore T = A^{-1} \cdot b$$

Where A^{-1} = inverse of the matrix

Using the discretisation methods described with the resulting matrix, a detailed analysis of the first order and higher order upwind schemes was carried out for both an equi-spaced and stretched mesh. The aim was to take a closer look at the workings of the scheme, verify the order of accuracy of the numerical scheme as well as determine the optimum number of nodes needed for simulating at a desired accuracy of below 1% for the example case. This thus informs our decision of what numerical scheme to choose for works in this thesis. This analysis is carried out in the next chapter, chapter 4.

4 MESH GENERATOR ANALYSIS REPORT AND DISCUSSION

In this chapter, we present the results of the mesh generator analysis of the upwind schemes for an equispaced and a stretched mesh as described in the previous chapter. Both the stretched and equispaced mesh are analysed for first and higher order upwind schemes. The governing equation as described in the previous chapter is repeated here for continuity.

$$S(x) = -\frac{\partial u_x T}{\partial x} + \frac{\partial}{\partial x}\left(k\frac{\partial T}{\partial x}\right) \quad 4.1$$

Where $S(x)$ = Source term = 0

k = thermal conductivity

T = Scalar quantity temperature 'T'

The matrix form resulting from discretizing the equation is modelled in MATLAB. The detailed discretization of the governing equation (equation 4.1) can be found in section 3.3. The results, graphs, and conclusion from the analysis is presented below. Based on this, a numerical scheme to be used in this paper is picked at the end of this chapter.

4.1 FIRST ORDER UPWINDING

4.1.1 EQUISPACED MESH

Based on the MATLAB simulations (code seen in appendix A1), for an equi-spaced mesh, the minimum number of nodes required to reduce the maximum nodal error to below 1% is 611, with an error of 0.998938%. This is for a representative scenario as described in section 3.8. Presented in figure 4.1 to 4.3, are temperature plots of the temperature distribution using 3 different number of node (10, 100, 1000).

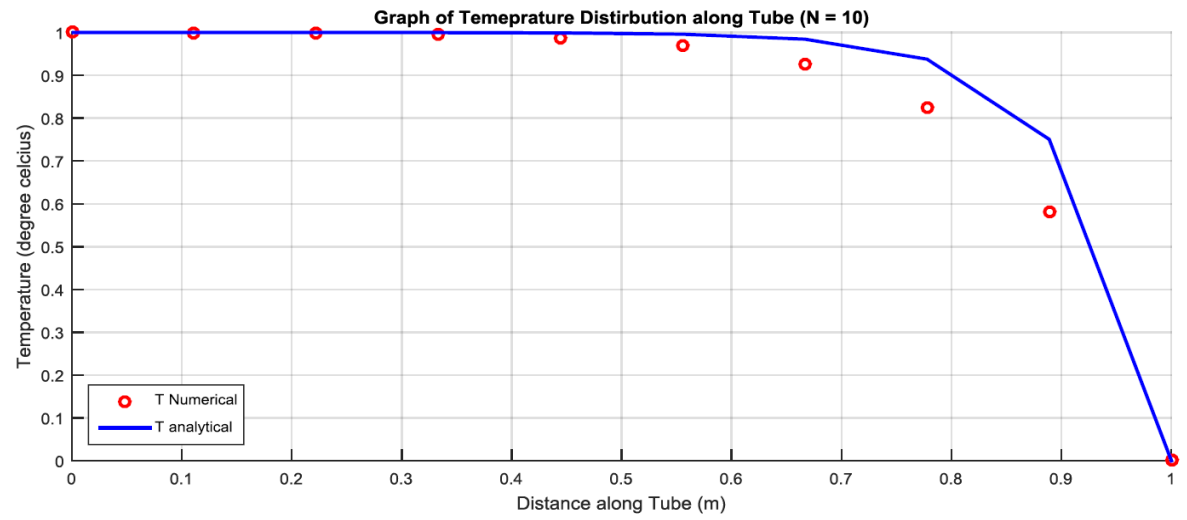

Figure 4.1: Temperature Distribution along Pipe (N = 10, equi-spaced)

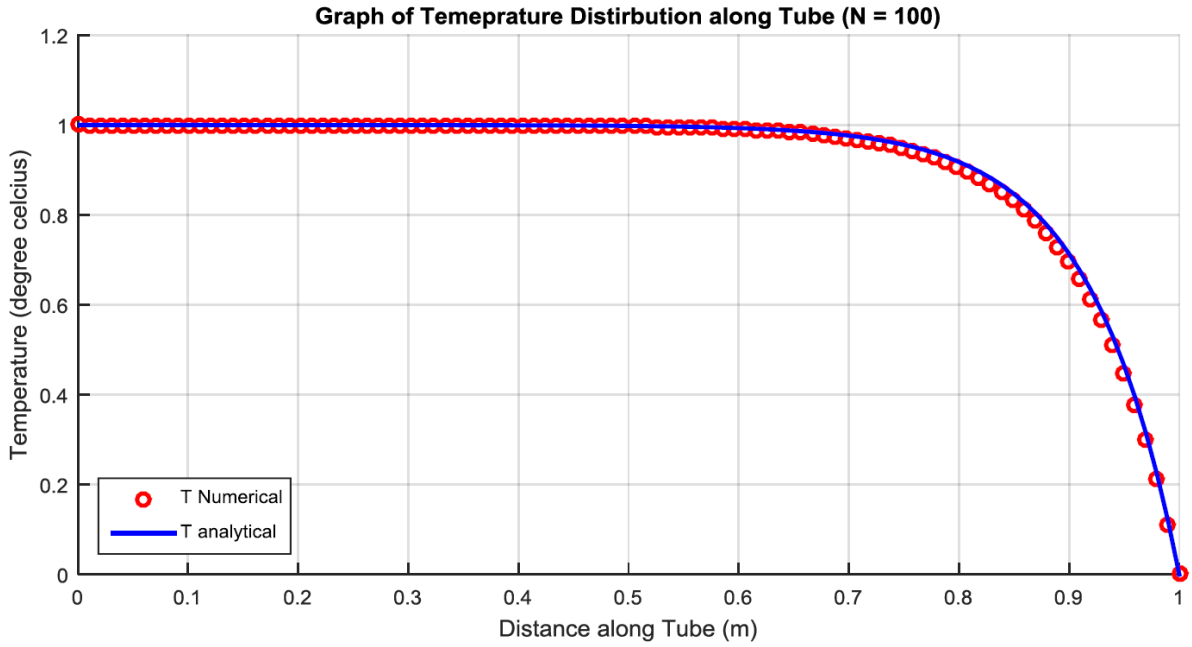

Figure 4.2: Temperature Distribution along Pipe (N = 100, equi-spaced)

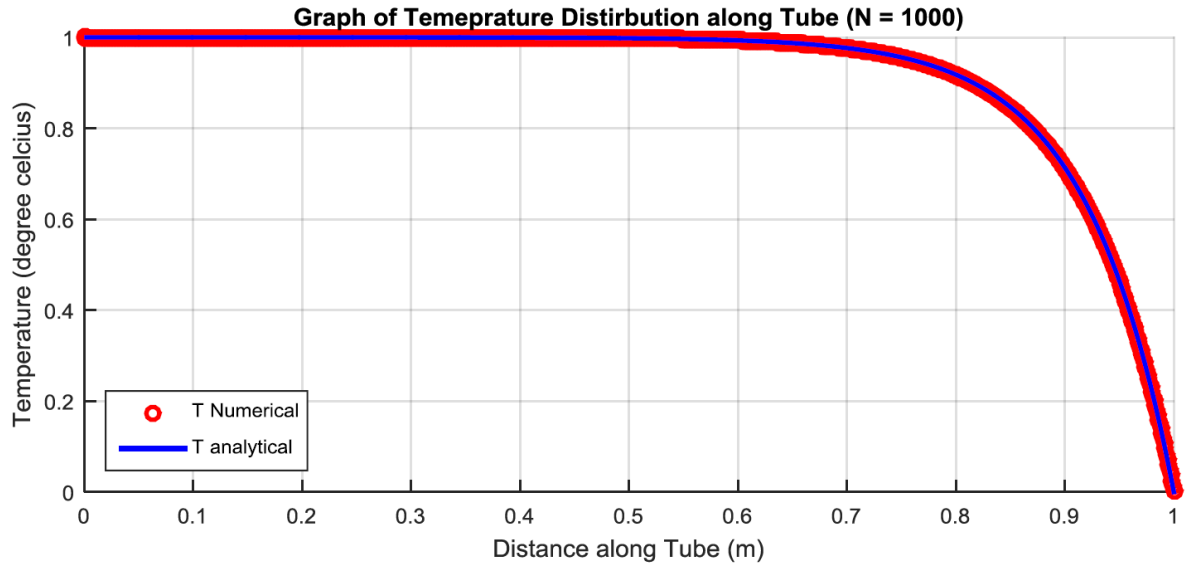

Figure 4.3: Temperature Distribution along Pipe (N = 1000, equi-spaced)

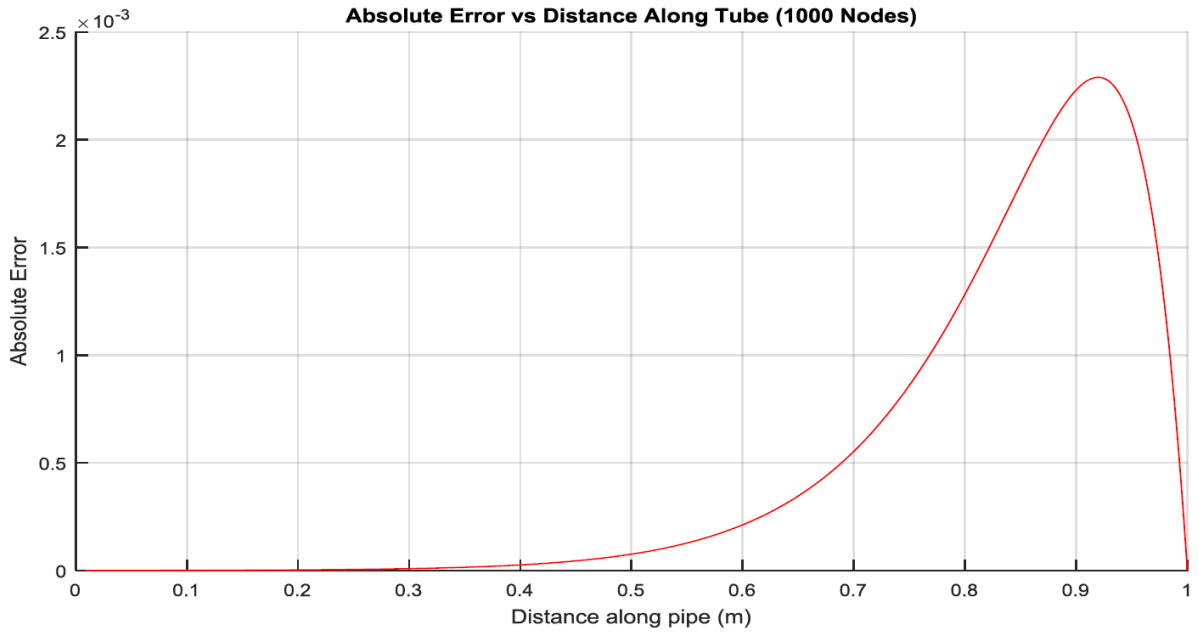

Figure 4.4: Error Analysis (equi-spaced, N = 1000)

Looking at the plots it is evident that the accuracy of the first order upwinding for an equi-spaced mesh increases with increasing number of nodes (finer mesh spacing).

The plot of absolute error against the distance in the tube seen in Figure 4.4, describes the error distribution in the tube as a function of flow gradient using the first order upwinding method. As the change in flow gradient increases toward the end of the tube, the error is

seen to drastically increase to plateau and then experience a negative change in gradient. This peak error point along the tube corresponds to the point of maximum change in gradient, which is what was to be kept to a minimum (below 1%), by reducing maximum nodal error.

4.1.2 STRETCHED MESH

For a stretched mesh, the minimum number of nodes required to reduce the maximum nodal error to below 1% was seen to be 86 with an error of 0.9925% with a ß value of 0.95. This was determined by varying both N (number of nodes) and ß (stretching factor). Table 4.1 shows minimum number of nodes needed to reduce the max nodal error to below 1% while varying the stretch factor - ß.

Table 4.1: Table showing Varying ß with Minimum Number of Nodes for 1% Error

Stretching Factor (β)	Minimum N for Max Nodal Error < 1%
0.87	249
0.88	254
0.89	306
0.90	316
0.91	361
0.92	422
0.93	483
0.94	106
0.95	86
0.96	89
0.97	102
0.98	130
0.99	197

From Table 4.1 above, using first order upwinding, it can be seen that with the stretching factor for a non-Equispaced mesh, there exists a sweet spot that results in the least number of nodes to achieve maximum nodal error below 1%. This ß value was seen to be 0.95.

Figure 4.5 to 4.7 shows the temperature distribution along the tube using 3 different numbers of nodes (10, 50,100). It shows that the accuracy of the first order upwinding for a stretched mesh also increases with increasing number of nodes (finer mesh spacing) while keeping ß constant.

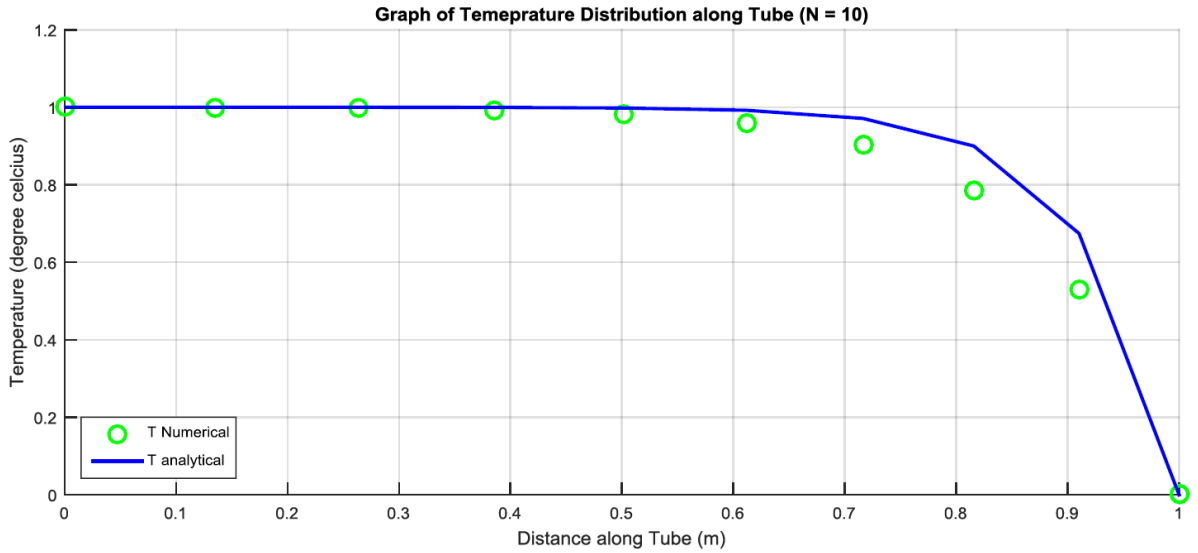

Figure 4.5: Temperature Distribution along Pipe (N = 10, stretched)

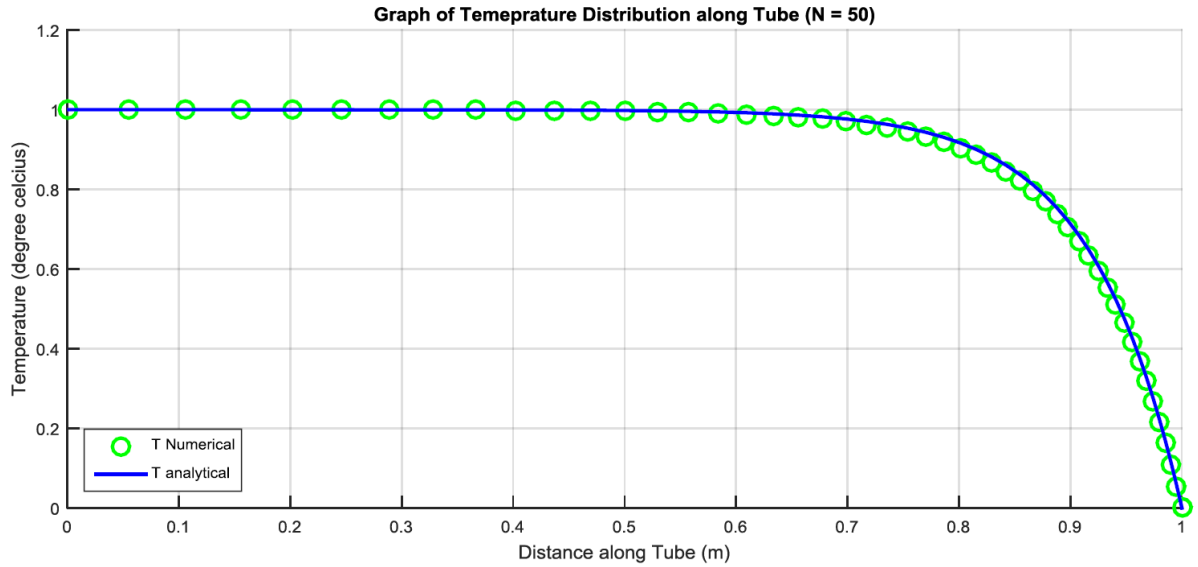

Figure 4.6: Temperature Distribution along Pipe (N = 50, stretched)

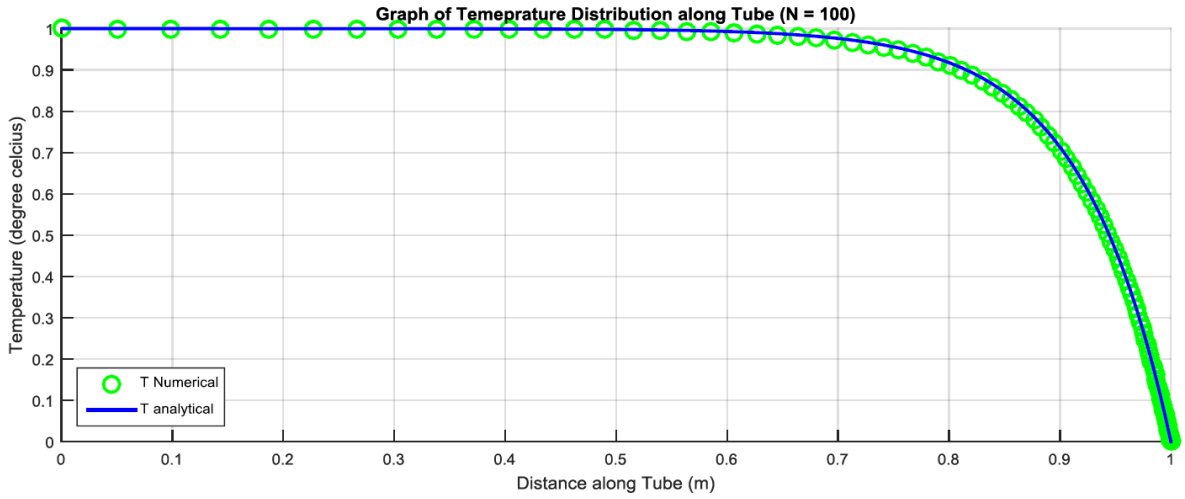

Figure 4.7: Temperature Distribution along Pipe (N = 100, stretched)

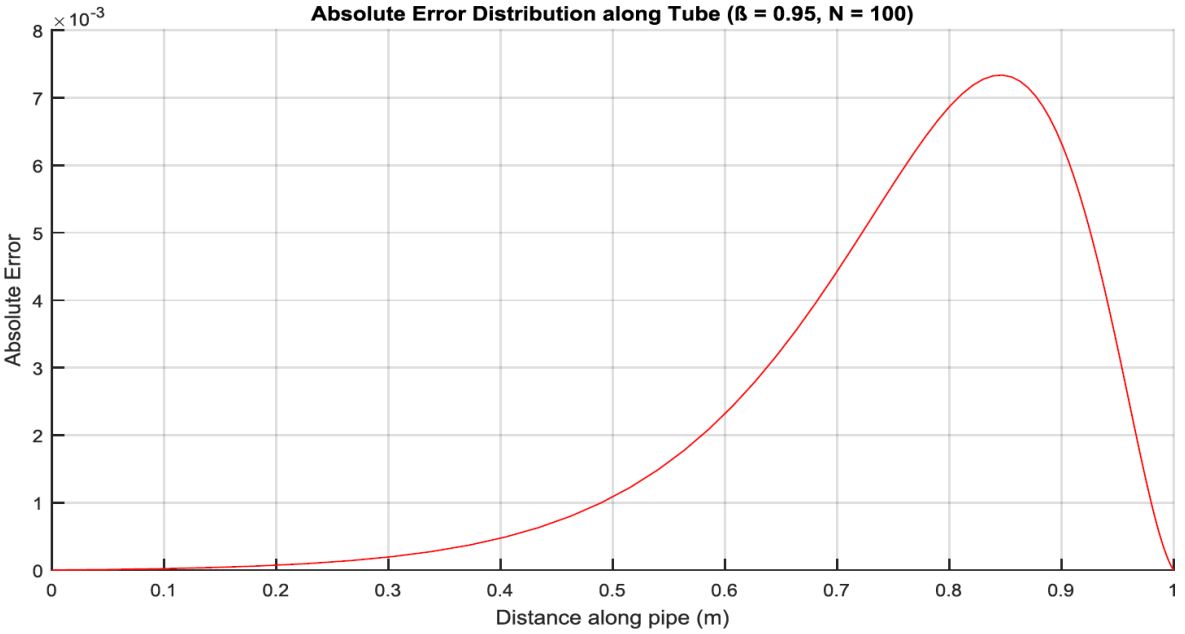

Figure 4.8: Error Analysis (stretched, N = 100)

From the plot of absolute error against the distance in the Figure 4.8, the change in flow gradient increases toward the end of the tube, the error is seen to drastically increase to plateau and then experience a change in gradient. This is similar to that of an equispaced mesh only more accurate. This can be seen by analysing the plots for both equi-spaced and stretched mesh.

4.1.3 MESH INDEPENDENCE STUDY

It can be shown that,

$$T_{analytical} = T_{numerical} + Error(\beta \Delta x) \quad 4.2$$

Applying some algebra;

$$Error = C * \beta \Delta x^n \quad 4.3$$

$$In\ Error = In\ C + n * In\beta \Delta x \quad 4.4$$

Where ß = 1 for an Equispaced mesh

Thus, a plot of the natural log of error against that log of mesh spacing (Δx) should result in a graph whereby the slope equates to the total order of error of the numerical scheme employed. For a numerical scheme using the first order upwinding method, for 100% accuracy, the slope of the log (Error) –log (Δx) graph would thus be equal to one.

1. Equispaced Mesh

The graph as described above of log (error) against log (Δx) is shown in Figure 4.9. This is plotted for N = 10 through to N = 1000.

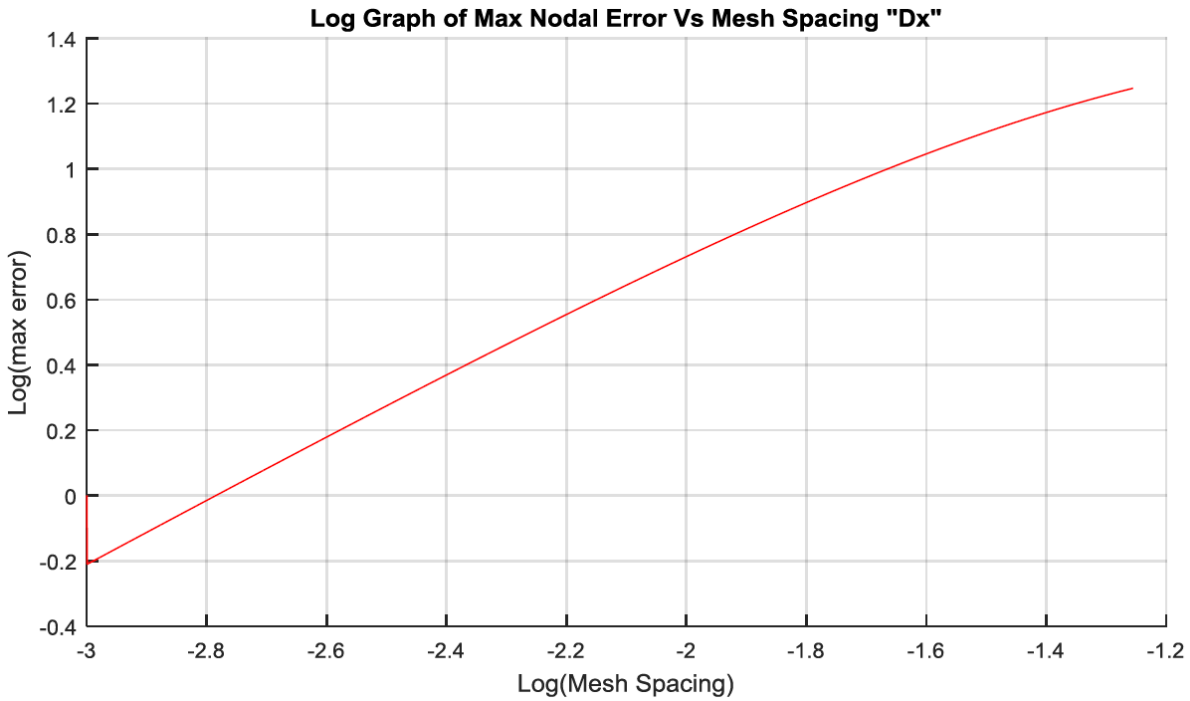

Figure 4.9: Mesh Dependence Plot Equi-Spaced Mesh

The values for Figure 4.9 were then exported to excel and plotted for two different ranges.

- For nodes 20 – 200
- For nodes 500 - 800

The equation of the trend line is presented in the table below showing the slope of trend line which gives a representation of the average slope of the graph for the selected range of nodes.

Table 4.2: Showing slope of log-log graph of Error vs. Mesh spacing for low and high number of nodes

Nodes	Equation of a Trend Line	Slope of Trend Line
Low Nodes (20 – 200)	y = 0.7965x + 2.3139	0.7965
High Nodes (500 – 800)	y = 0.9758x + 2.7174	0.9758

For the first order upwinding method, it is expected that the slope of the graph shown in Figure 4.9 should approach unity as the number of nodes is increased. This is because as we increase the number of nodes used, and thus reduce the mesh spacing, the accuracy of the numerical scheme increases because we approach a representative number of nodes for least error, which was determined in section 4.1.1. It is thus expected that at higher number of nodes, the slope of the graph should be closer to unity than at lower number of nodes. This is in fact shown by taking the average slope of the graph for the selected range of nodes for both low and high nodes as shown in Table 4.2. This thus verifies the order of accuracy of the numerical scheme employed in this solution.

2. Stretched Mesh

The graph of log (error) against log (Δx) is shown below for a stretched mesh. A similar process as described for the equi-spaced mesh is used here.

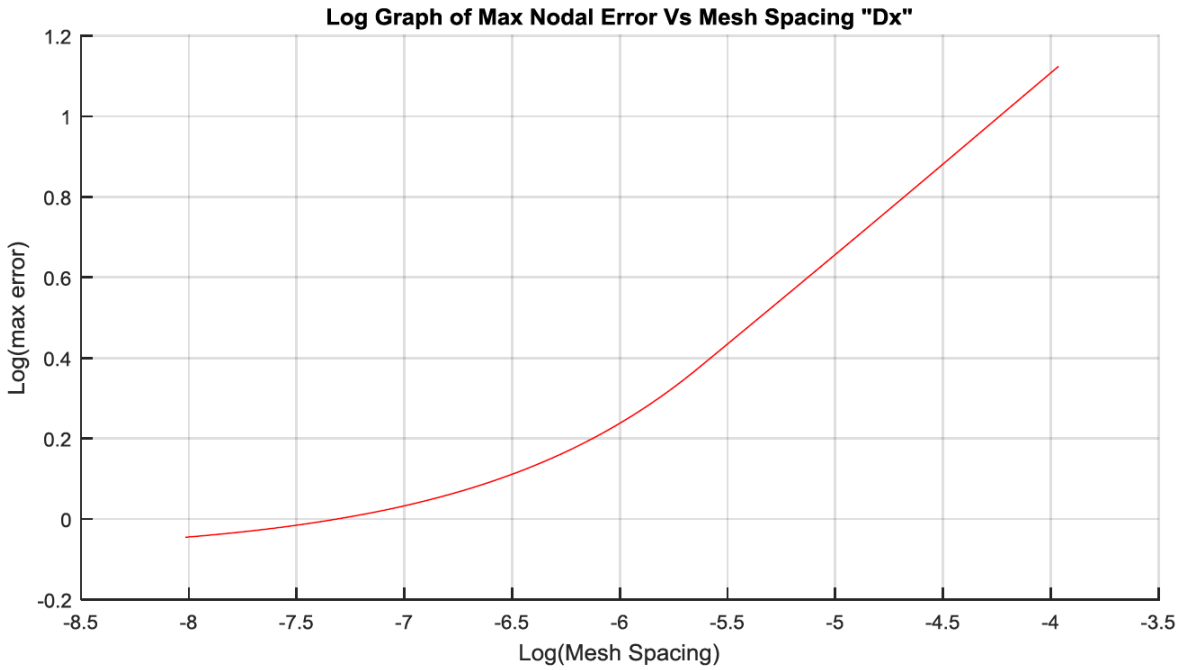

Figure 4.10: Mesh Dependence Plot, Stretched Mesh

Figure 4.11: Showing slope of log-log graph of Error vs. Mesh spacing for low and high number of nodes

Nodes	Equation of a Trend Line	Slope of Trend Line
Low Nodes (20 – 50)	y = 0.4492x + 2.9033	0.449
High Nodes (50 – 85)	y = 0.233x + 1.6529	0.233

For a non-Equispaced mesh, it is expected that the error term be first order. For constant ß, this error term is expected to decrease as the difference in size of adjacent control volumes decreases. Thus, as the mesh becomes finer in a given scenario, it is expected that the error reduces. Plotting the log – log graph of error vs. mesh spacing, the slope of the graph should thus be unity once again. From Figure 4.10 and Figure 4.11 however, this is not the case. This is most likely due to the implementation of an error in the numerical solution.

4.1.4 CLOSURE – FIRST ORDER UPWIND

For an Equispaced mesh, it was seen that the minimum number of nodes required to reduce the maximum nodal accuracy to below 1% was 611. The order of accuracy of the numerical scheme was then verified by plotting a log-log graph of error and mesh spacing. The slope of the graph was seen to approach unity for finer mesh spacing, thus, indicating that the order

of accuracy of the numerical scheme approaches unity for finer mesh spacing which was expected.

For a Stretched mesh, different ß values were used while also varying the number of nodes required to reduce the maximum nodal accuracy to below 1%. It was seen that for ß value of 0.95, the minimum number of nodes required was 86 nodes. This results in greater accuracy as finer mesh sizes are used for regions of higher changes in flow gradient. This also results in faster computation compared the scenario of an equi-spaced mesh.

It was also seen that with a stretched mesh for the first order upwinding method that increasing or reducing ß doesn't necessarily mean an increased or reduced accuracy. There thus exists a sweet spot with the ß value that results in the least number of nodes. The MATLAB code used for the first order upwind can be seen in appendix A1.

The next step to further increase accuracy would be the use of higher order upwinding methods.

4.2 HIGHER ORDER UPWINDING

Based on the discretized governing equation (equation 4.1), a mesh generator analysis was carried out in MATLAB for higher order upwinding. The processes are similar to that of first order upwinding seen in previous sections of this chapter.

4.2.1 EQUISPACED MESH

For an equi-spaced mesh, the minimum number of nodes used required to reduce the maximum nodal error to below 1% for different κ values are shown in Table 4.3

Table 4.3: Table showing Varying k values with Minimum Number of Nodes for 1% Error

K Values	Minimum Number of Nodes	Error at Node
1/2	11	8.357912e-01
1/3	8	2.043108e-01

The temperature distribution along the pipe of the three different schemes is shown in the figures 4.12 – 4.15 below for different numbers of nodes, one being the minimum number of nodes required for less than 1% accuracy.

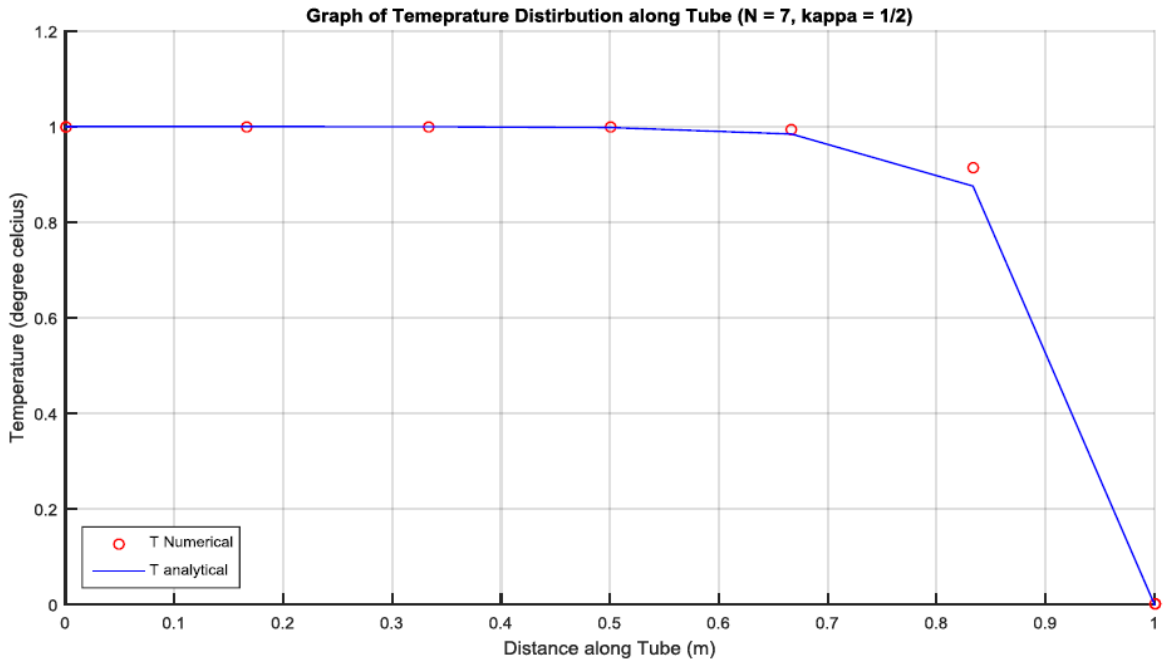

Figure 4.12: Temperature Distribution along Pipe (N = 7, ß = 1, kappa = 1/2)

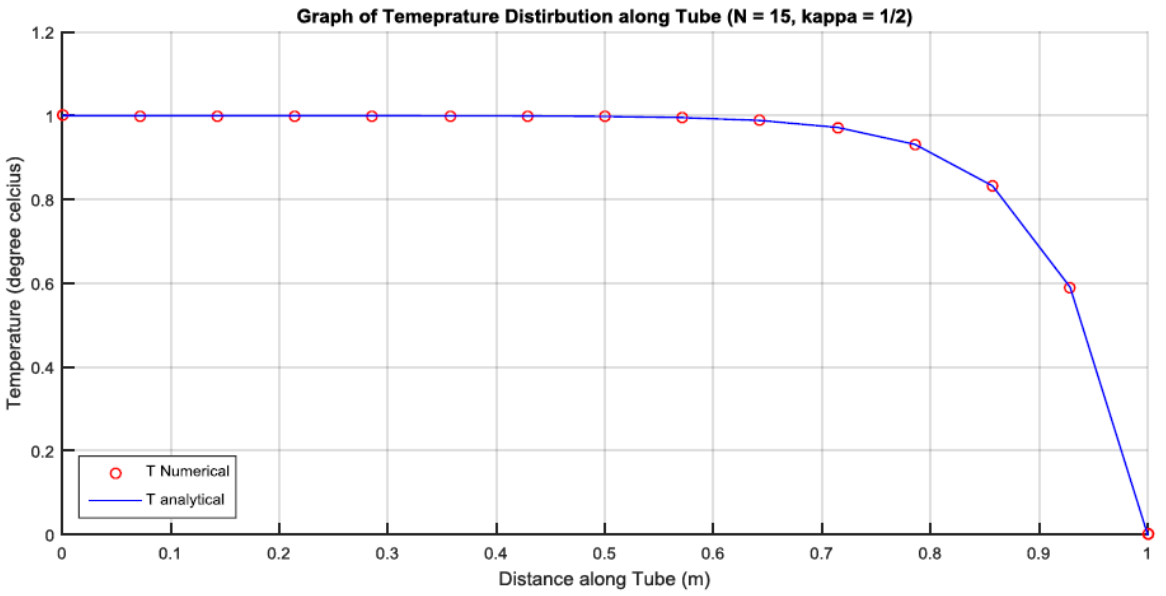

Figure 4.13: Temperature Distribution along Pipe (N = 15, ß = 1, kappa = 1/2)

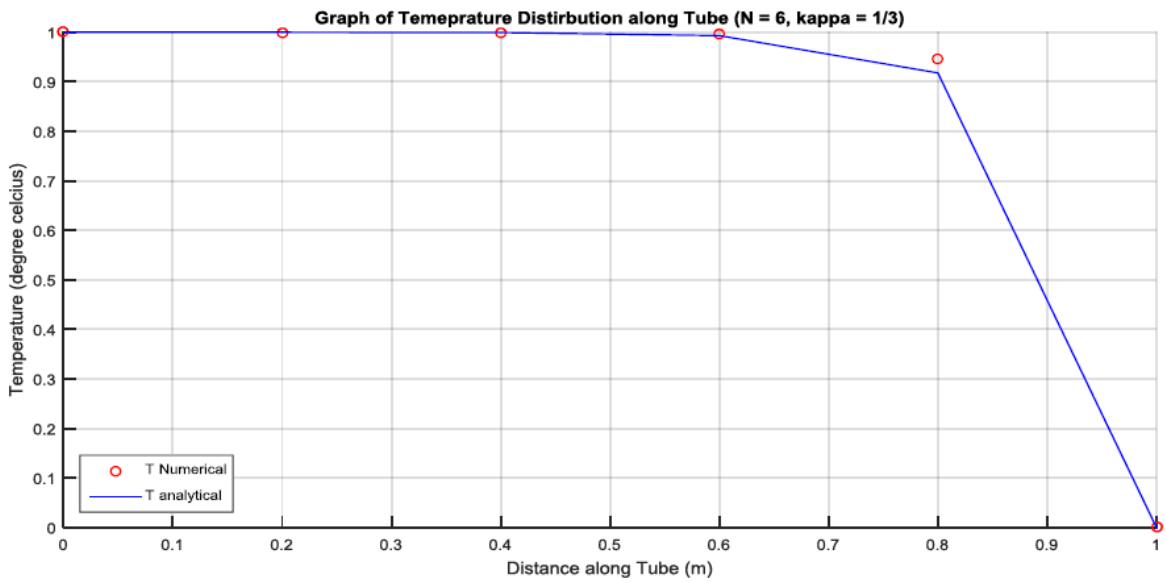

Figure 4.14: Temperature Distribution along Pipe (N = 6, ß = 1, kappa = 1/3)

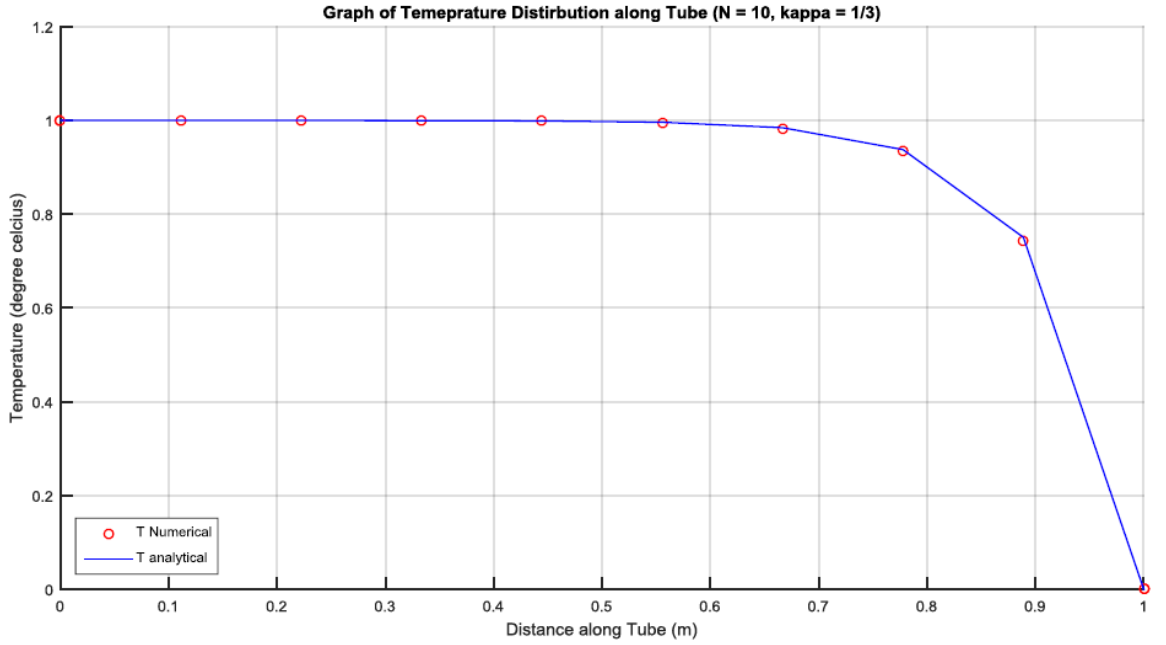

Figure 4.15: Temperature Distribution along Pipe (N = 10, ß = 1, kappa = 1/3)

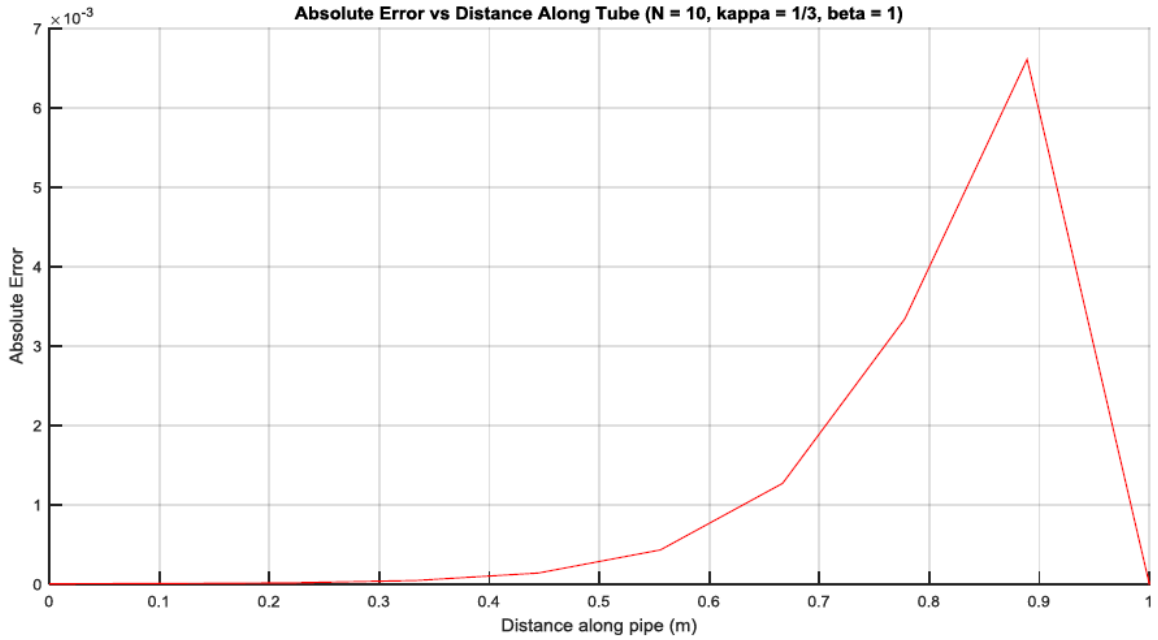

Figure 4.16: Error Analysis (equi-spaced, N = 10, kappa = 1/3)

In comparison to the first order upwinding methods for an equi-spaced mesh, it can be seen that the number of nodes is reduced exponentially in order to achieve a maximum nodal error of 1%. The CUI method being the more accurate with just 8 nodes as compared to the QUICK method which has 11 nodes, which still beats the first order upwinding method which saw 611 nodes.

4.2.2 STRETCHED MESH

For a non equi-spaced mesh, the minimum number of nodes used required to reduce the maximum nodal error t below 1% for different κ values varying the stretching factor (ß) are shown in Table 4.4.

Table 4.4: Table showing Varying ß with Minimum Number of Nodes for 1% Error for different Kappa values

Stretching Factor (ß)	Kappa Values	Minimum Number of Nodes
0.79	1	11
	1/2	6
	1/3	11
0.81	1	12
	1/2	6

	1/3	12
0.83	1	13
	1/2	7
	1/3	12
0.85	1	13
	1/2	7
	1/3	6
0.87	1	14
	1/2	7
	1/3	6
0.9	1	16
	1/2	8
	1/3	6
0.94	1	20
	1/2	9
	1/3	7

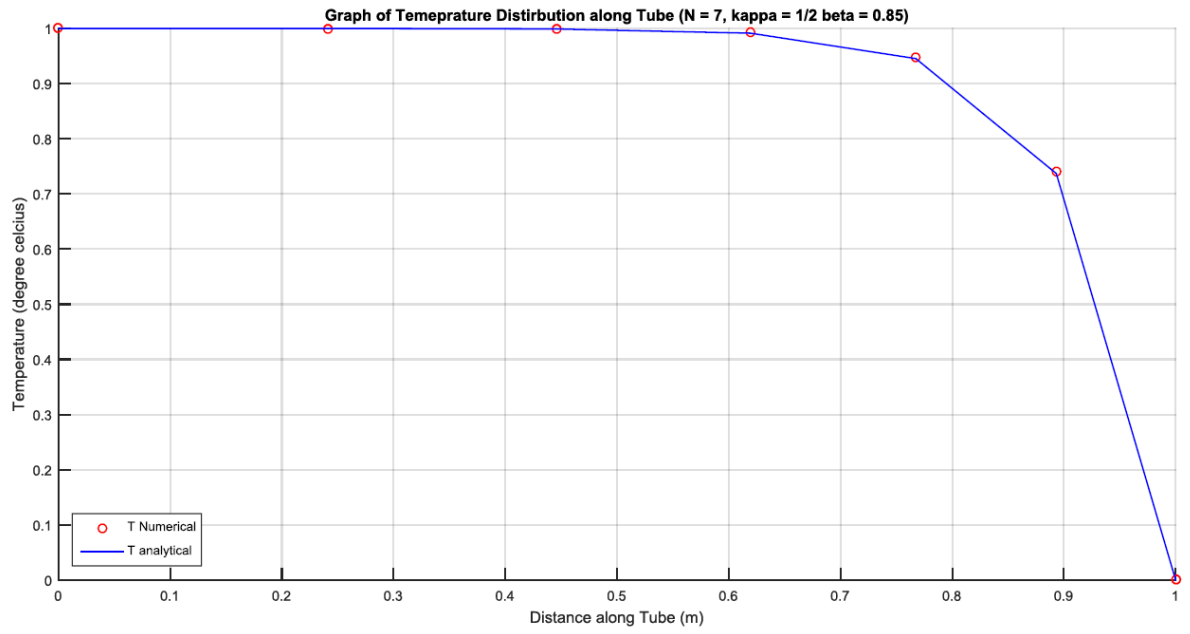

Figure 4.17: Temperature Distribution along Pipe (N = 7, ß = 0.85, kappa = 1/2)

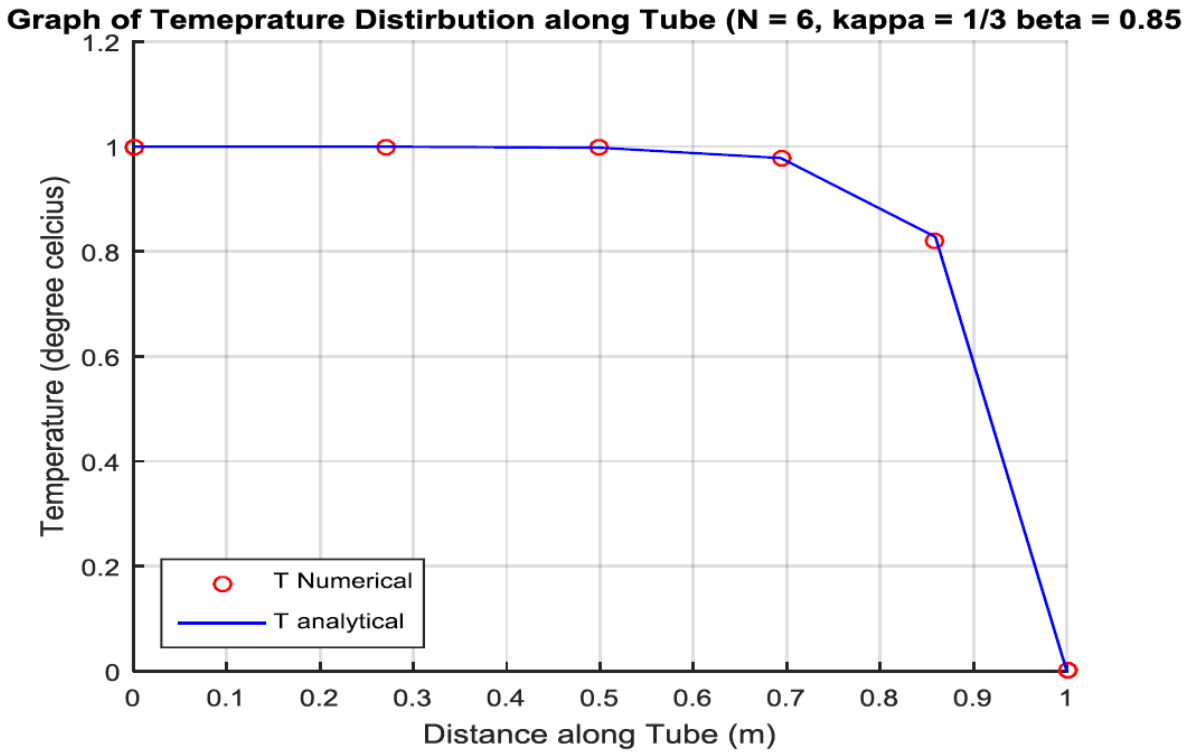

Figure 4.18: Temperature Distribution along Pipe (N = 6, ß = 0.85, kappa = 1/3)

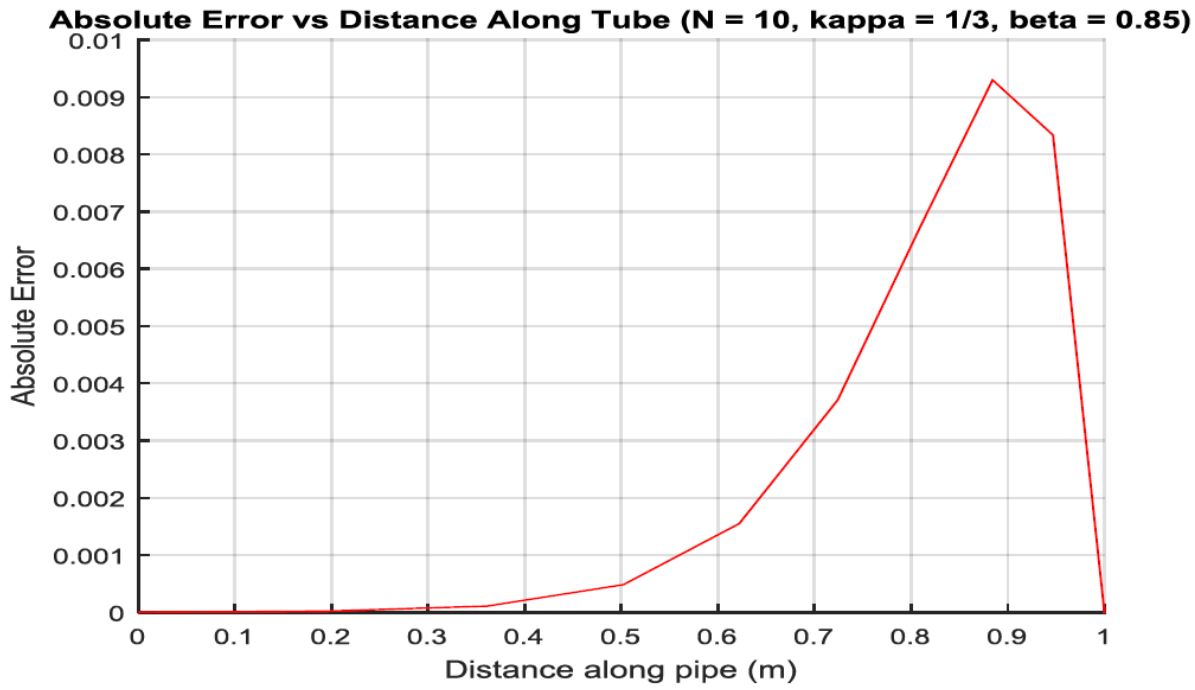

Figure 4.19: Error Analysis (equi-spaced, N = 10, kappa = 1/3, ß = 0.85)

From Figure 4.19, the stretching factor 'ß' of 0.85 results in the least amount of nodes to achieve a maximum error of 1%. With ß constant, we see that the CUI upwinding method as expected results in the least number of nodes required to get a maximum nodal error of 1%.

From the plot of absolute error against the distance in the tube (Figure 4.9), the change in flow gradient increases toward the end of the tube, the error is seen to drastically increase to plateau and then experience a change in gradient. This is similar to that of a stretched mesh only more accurate. This can be seen by analysing the plots for both equi-spaced and stretched.

4.2.3 MESH INDEPENDENCE STUDY

Similar to the study carried out for the first order upwinding, using equations 4.2 – 4.4 from the previous section on first order upwinding, a plot of the natural log of error against that log of mesh spacing (Δx) should result in a graph whereby the slope equates to the total order of error of the numerical scheme employed. For a numerical scheme using the CUI order upwinding method, for 100% accuracy, the slope of the log (Error) –log (Δx) graph would ideally be equal to three.

It is important to note that, though the order of accuracy for the convective term is 3^{rd} order, the diffusive term has an accuracy of 2^{nd} order. That being said, it can be expected that the slope of the log/log graphs of absolute maximum error against mesh spacing be less than 3 due to the lowest order of accuracy in the discretization method used for the complete equation being = 2. A behaviour that might be expected would be that for a convective dominated flow, the slope of the log, log graph would be closer to 3 than 2, as the convective term is 3^{rd} order accurate.

1. Equispaced Mesh

The graphs displayed in figure 4.20 – 4.21 shows the plot of log (error) against log (Δx). This is plotted for N = 3 through to N = 8.

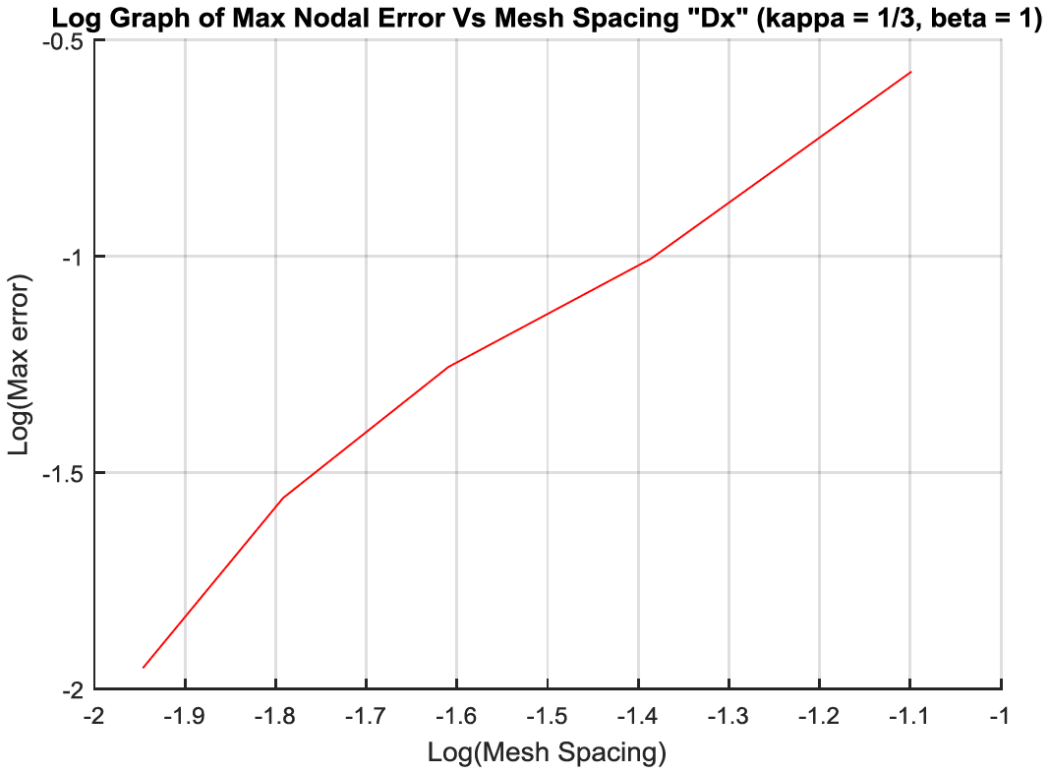

Figure 4.20: Mesh Dependence Plot Equi-Spaced Mesh (kappa = 1/3)

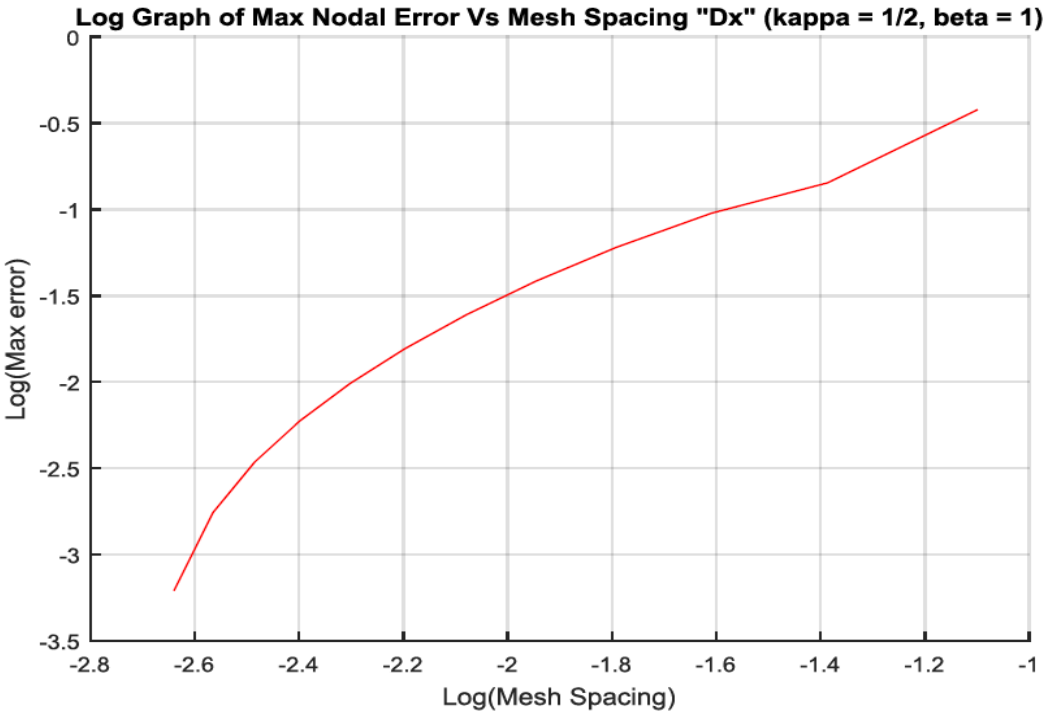

Figure 4.21: Mesh Dependence Plot Equi-Spaced Mesh (kappa = 1/2)

The equation of the trend line of the above graph is presented in the Table 4.5 showing the slope of trend line which gives a representation of the average slope of the graph for the selected range of nodes.

Table 4.5: Showing slope of log-log graph of Error vs. Mesh spacing for QUICK and CUI upwinding

Nodes	Equation Trend Line	Slope of Trend Line
QUICK(N = 3.15)	y = 1.204x + 0.8908	1.204
CUI (N = 3.8)	y = 1.5545x + 1.1661	1.5545

As explained at the beginning of this section, the slope of the trend line of the log-log graph plotted above would barely approach 3. This is due to the fact that the order of accuracy of the complete discretized equation is below 3 owing to the accuracy order of the diffusive term which has an accuracy of order 2. The slope of the graph should thus be seen to at least approach 2 as the system becomes more and more mesh independent (increasing N and reducing mesh spacing). From Table 4.5 above, the slope approaches 2, but doesn't quite get as close as one might expect. This ideally should improve by making use of a stretched mesh.

2. Stretched Mesh

The graph of log (error) against log (Δx) is shown in figure 4.22 – 4.23 for a stretched mesh. This is plotted for N = 3 to N = 7. A similar analysis done for the Equispaced mesh is employed here.

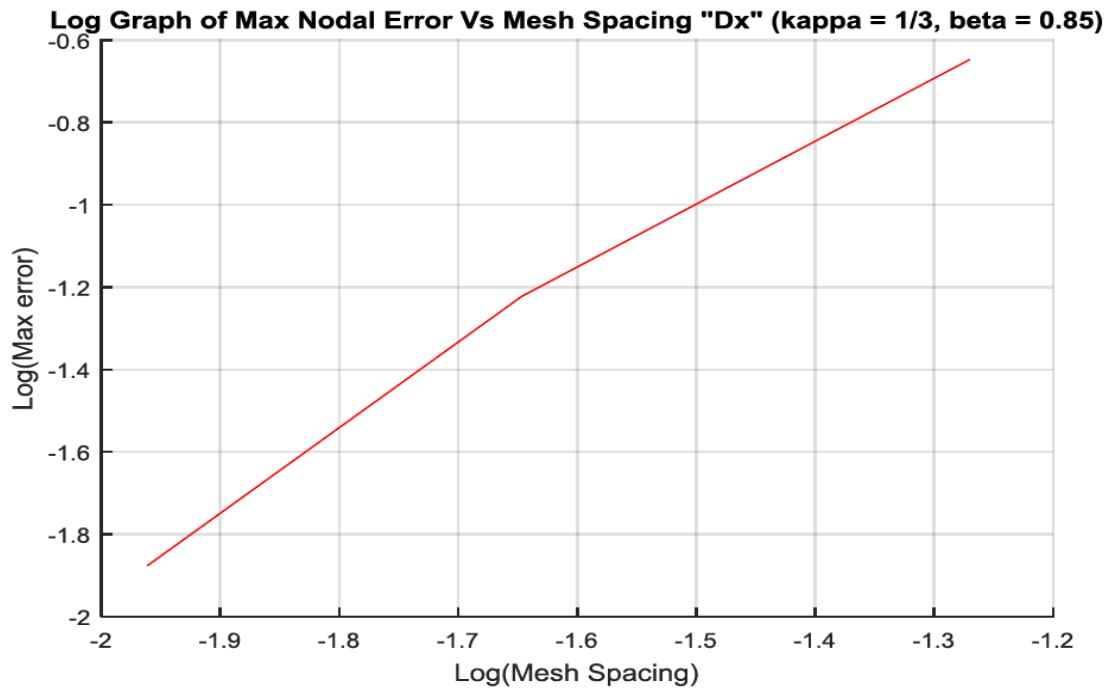

Figure 4.22: Mesh Dependence Plot Non Equi-Spaced Mesh (kappa = 1/3, ß = 0.85)

Figure 4.23: Mesh Dependence Plot Non Equi-Spaced Mesh (kappa = 1/2, ß = 0.85)

Table 4.6: Showing slope of log-log graph of Error vs. Mesh spacing for QUICK and CUI upwinding

Nodes	Equation of Trend Line	Slope of Trend Line
QUICK (N = 3.7)	y = 1.3259x + 1.2139	1.33
CUI(N = 3.6)	y = 1.7701x + 1.6296	1.77

For a non-Equispaced mesh, it is also expected that the total error term be less than 3^{rd} order accurate, owing to the diffusive part of the total governing equation, but greater than first order as the least order of accuracy of the upwinding methods used for discretization is 2. From Table 4.6 the slope of the trend line of the log/log plot for both the QUICK and the CUI upwinding method approaches error order accuracy of 2 as expected. This is an increase from the scenario of an equispaced mesh as seen in Table 4.5.

Of note however is the fact that for both the QUICK and CUI upwinding methods for the equispaced and stretched mesh, it was seen by plotting the log/ log graph of maximum nodal error against mesh spacing for higher nodes beyond the minimum nodes for 1% accuracy that the error doesn't follow a linear pattern as it is seen to increase and then decrease. This indicates some sort of instability in the error term by increasing the number of nodes beyond the determined minimum number of nodes for maximum nodal error to be equal to 1%. This can be seen in the graph for the CUI method for a stretched mesh (ß = 0.85) for nodes from 3 to 30 shown in Figure 4.24.

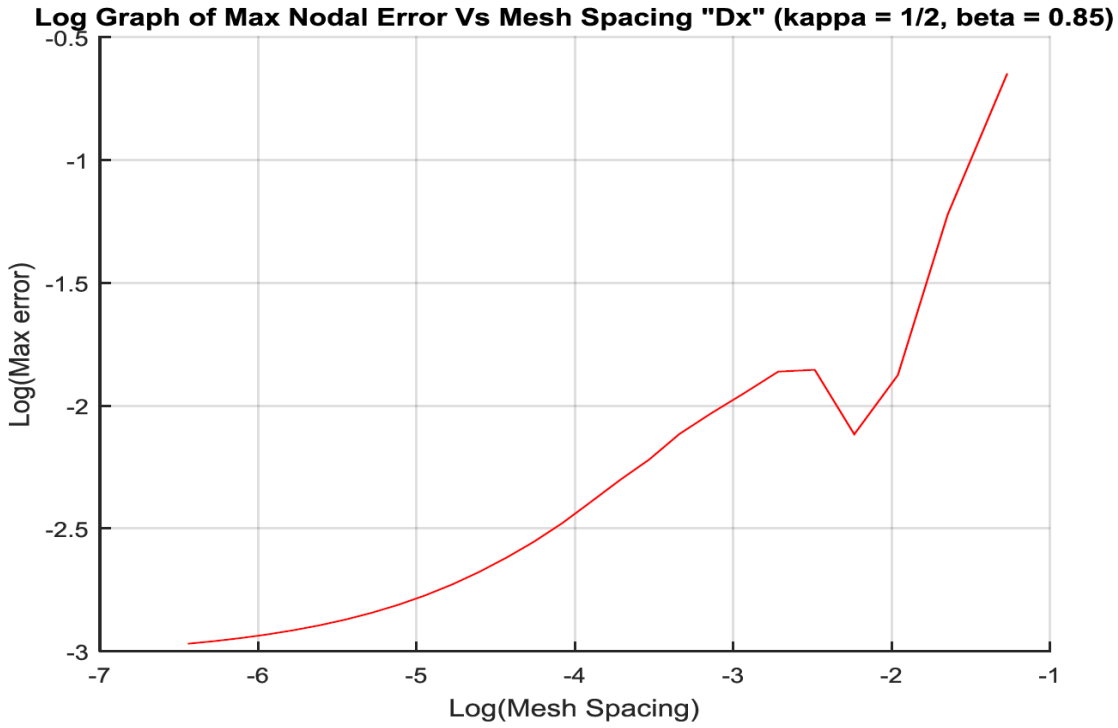

Figure 4.24: Mesh Dependence Plot Non Equi-Spaced Mesh (kappa = 1/2, ß = 0.85) for N = 3 - 30

4.2.4 CLOSURE – HIGHER ORDER UPWIND

For an equispaced mesh using the QUICK and CUI high order upwinding method, it was shown that maximum nodal error of below 1% is accomplished with way fewer nodes than that of the first order upwinding method, with the CUI upwinding method being superior. This improvement in reduction of number of nodes was made even better by making use of a non-equispaced mesh, where the number of nodes was further reduced to give 6 nodes, using the CUI upwinding method with ß = 0.85.

From the mesh dependency analysis, the slope of the log/log graph of max error against mesh spacing was seen to approach 2. This somewhat verifies the order of the accuracy as due to the fact that the diffusive term has an error of 2^{nd} order, the total error of the governing discretised equation should equal 2 for 100% accuracy.

For the stretched mesh, it was seen that increasing or decreasing beta doesn't necessarily result in increased accuracy. An optimal growth factor of ß = 0.85 was determined to yield the best results for this exercise.

The MATLAB code used for the higher order upwinding can be seen in appendix A2.

4.3 DECISION OF UPWINDING SCHEME

For the first order Upwinding method it was confirmed that the order of accuracy of the numerical scheme approaches unity for finer mesh spacing which as expected with a 611 minimum number of nodes while a minimum of 86 nodes was reported for the stretched mesh. Interestingly, it was seen that with a stretched mesh for the first order Upwinding method that increasing or reducing the stretch factor (ß) doesn't necessarily mean an increased or reduced accuracy. There exists a sweet spot with the ß value that results in the least number of node.

Similar observations were made for the equispaced and stretched mesh for higher Upwinding methods. Here, it was seen that the minimum number of nodes required for error to be below 1% improved for an equispaced and stretched mesh as expected, with the value for a stretched mesh being only 6 nodes using the CUI Upwinding method. It was also seen that for the stretched mesh, increasing or decreasing ß doesn't necessarily result in increased accuracy. An optimal growth factor of ß = 0.85 was determined to yield the best results for the exercise.

The software package being used, ANSYS FLUENT 16.0, incorporates several numerical schemes for discretising the convective term. These include the first-order upwind scheme, second-order upwind, QUICK scheme, central differencing scheme, and bounded central differencing amongst others.

For purpose of works done in this thesis, the QUICK Scheme as explained in previous paragraphs would be the chosen option in the ANSYS software package used for discretization due to absence of the CUI Scheme. The diffusion and source term would be discretized using the central difference scheme (CDS) as explained in previous paragraphs.

5 NUMERICAL SIMULATION METHODOLOGY

This chapter is started by describing the cylindrical model as was used in an analytical CFD domain used for the numerical simulations. The model was constructed using the 3D modelling package (DesignModeler) of ANSYS Fluent fluid flow simulation software. It is then followed by decisions on the geometry and domain setup, boundary conditions and CFD simulation based on procedures explained in chapter 3 of this thesis. The chapter is brought to an end by an analysis of the effects of radiation analysis on the CFD simulation and how the convective heat transfer coefficient (h_{conv}) was actually computed.

5.1 CYLINDRICAL MODEL AND CFD DOMAIN

The cylinder model and CFD domain were constructed using the model designer package of ANSYS workbench – DesignModeler. Figure 5.1 shows the outline of the domain with the cylinder model (in the inclined position) placed at the centre of the analytical surrounding domain with dimensions described in Table 5.1. The surrounding domain is made up of only air as the cylinder is assumed to cool with just air in this thesis.

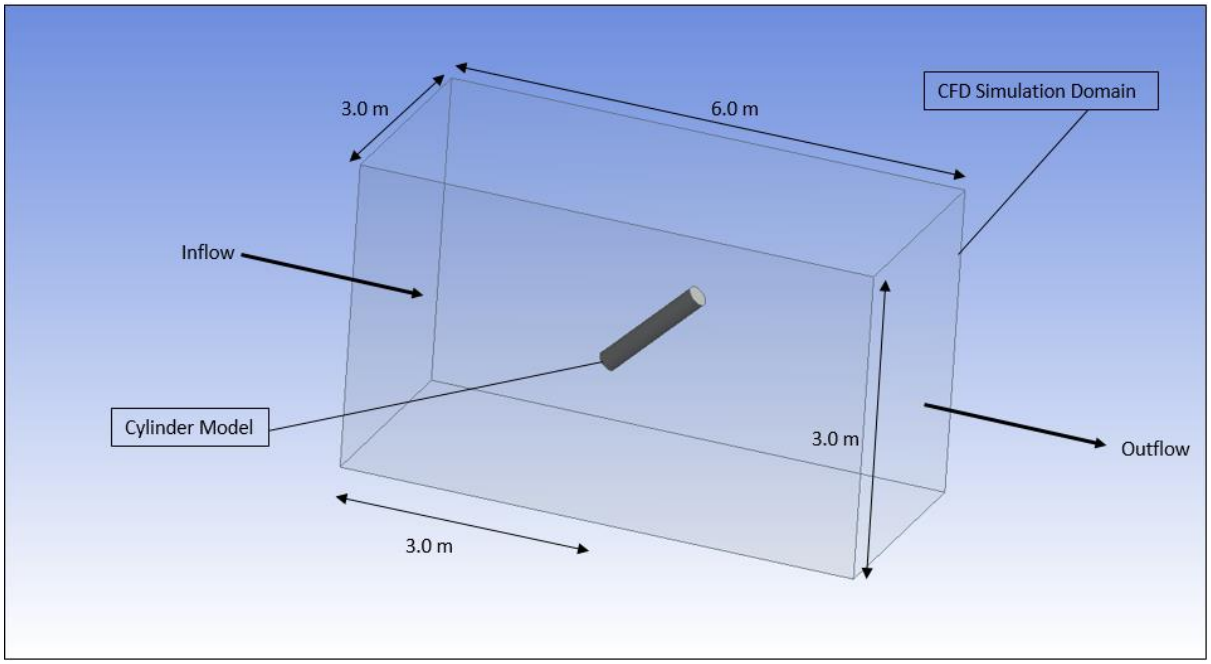

Figure 5.1 CFD Analytical Domain as used in the CFD simulation

The cylinder dimensions resulting in a total surface area of $1.74\mathrm{m}^2$ as shown in Table 5.1 were chosen to mimic that of a human body in the standing position as seen in literature such as works published by Kurazumi *et al*. (Kurazumi *et al*., 2003) and Cong Li *et al*. (Cong & Kazuhide, 2012; Li & Ito, 2014b), to mention a few. Three different cylinder positions – Upright, Inclined at 45 deg. and Supine – were analysed.

The temperature of the inlet wind was kept at 304K, the same as that of the surrounding temperature, while that of the cylinder was kept at 307K. This temperature difference between the cylinder and the surrounding is kept constant for all the simulations carried out for turbulent flow and varied from 291 K to 307K for laminar flow to allow for 5 different temperature differences. The temperature values of 304K and 307K for the inlet air temperature and the cylinder respectively were chosen deliberately to produce a temperature difference which minimizes the effect of radiation on the simulations as radiation is not the primary focus of this thesis. This effect of radiation and how this was accounted for is discussed further in section 5.4.

The dimensions of the cylinder were chosen to describe that of a human body model. To this end, the volume and surface area of the human model used in literature was used to computes the dimensions of the cylindrical model. The surface area of 1.74 m^2 as seen in the works by Cong *et al*. (Cong & Kazuhide, 2012) was used to compute the dimensions of the cylindrical model detailed in Table 5.1.

The inlet velocity was varied from 2m/s to 12m/s at 2m/s increment, resulting in a total of 6 cases per cylinder position. Turbulence Intensity (TI) is also varied from 2% to 10% as 0% is not a feasible scenario and TI greater than 10% is considered high TI and is ideal for scenarios where flow upstream is fully developed. For under-developed and undisturbed flow, as in this paper, low TI is advised, thus less than 10%. (ANSYS, 2003). The described variations result in a total of 90 numerical simulations to be carried out for turbulent flow over the cylindrical model. These variations are tabulated in table 5.1.

Table 5.1 CFD Simulation Parameters for turbulent flow

Item	Dimensions
Cylinder	Height = 1.736 m Diameter = 0.2934 m Surface Area = 1.74 m^2 (Cong & Kazuhide, 2012)

	Volume = 0.12 m^3 (0.064 in lit review - Cong & Kazuhide, 2012) Constant tempt. = 34 deg. (307 K) Variations (3 cases) • Upright • Inclined at 45 degrees and • Supine Cylinder
Surrounding Domain	Width = 3m Height = 3m Length = 6m Cylinder position = 3m from inlet Wall tempt. = 30 deg. (304 K)
Air at 304K	Density = 1.1644 kg/m^3 Dynamic viscosity = 1.8885 exp -5 kg/(m.s) P = 101325 pa Re = 4252.2 x Velocity. Thus, for velocity greater than 0.941m/s, Re > 4000, thus turbulent. Variations • Air velocity is varied from 2 to 12 m/s at increments of 2m/s. (6 cases) • Turbulence intensity is varied from 2 to 10 % at increments of 2 % (5 cases)

Using the parameters as described in table 5.1, the Reynolds number, Re is computed as 4252.2v, where v = velocity. Thus, for velocities greater than 0.941m/s, Re > 4000, thus turbulent.

5.2 MESHING THE 3D MODEL

At this point, the cylindrical 3D model and its surrounding domain has been constructed in design modeller of the ANSYS software package. The next step is to perform the meshing operations on the 3D geometry in the mesh generator of the ANSYS package as described in chapter 3.

For the mesh creation, the boundary layer of the cylinder was solved by creating an inflation layer of prism cells on the surface of the cylinder. This maintains a smooth volumetric growth between each adjacent layer with a growth rate of 1.2 and 4 layers using the smooth transition inflation. From the outside of this boundary layer to the side of the inside walls of the analytical space, tetra-meshes are arranged. This ensures a certain degree of accuracy as the elements stretches towards the side walls for a given number of grid points. The analytical space was set up from a total of approximately 200,000 to 300,000 cells.

5.3 NUMERICAL AND BOUNDARY LAYER CONDITIONS

The analytical surrounding domain with the cylinder is as described in the preceding section 5.1. In literature, there exists three types of turbulence model typically used for turbulence modelling as described in section 3.6. The SST $k-\omega$ turbulence model as decided in chapter 3 was used with low Reynolds (Re) number correction property on ANSYS fluent software.

With the analytical space (Mesh) all set up, the Ansys Fluent CFD code (Ansys 16.0) was used to calculate the air flow and heat transfer around the cylinder in three dimension. The "Energy" and "Viscous" model were turned 'On' for the CFD simulations, selecting the SST $k-\omega$ model with low Reynolds number corrections. The SIMPLE algorithm option was used with the QUICK scheme to solve for the convection. To enable precise analysis of the flow pattern and temperature gradient inside the analytical space, the NO-Slip condition was adopted as the boundary condition for velocity at the wall surfaces. The numerical and boundary conditions as used in the Ansys Fluent software are summarized below. For reference, the underlying theory behind these decisions are detailed in chapters 3 and 4.

Table 5.2 Numerical and Boundary Conditions

Turbulence Model	SST $k-\omega$ model with low Reynolds Number correction.
Scheme for the convection term	QUICK
Wall Treatment	Velocity = no slip
Cylinder Surface Treatment	
Inflow Boundary	$k_{in} = \frac{3}{2} * (U_{in} * 0.01 * TI)^2$ $\omega_{in} = C_{\mu} * \frac{k_{in}^{0.5}}{l_{in}}$
Outflow Boundary	$k_{in} = \omega_{in} = U_{in} = free\ slip$

Once Fluent was all set up with the parameters as outlined in Table 5.2, all cases as outlined in Table 5.1 were simulated by changing the k (turbulent kinetic energy) and ω (specific

dissipation rate) values. The comprehensive results from all 90 cases analysed in this paper using the model described above are presented in appendix B1 to B3.

The prediction accuracy of the SST $k-\omega$ model as used in this paper sees reasonable consistency as used in other works in literature. One of such with great similarity to works carried out in this paper is works published by Cong Li *et al*. where they validated the prediction accuracy of the model with a wind tunnel experiment using similar boundary conditions to that used in the CFD simulations (Cong & Kazuhide, 2012).

5.4 RADIATIVE HEAT FLUX ANALYSIS

All temperatures are assumed to be constant, and the temperature difference between the surrounding and the cylinder relatively low at a maximum temperature difference of 20K.

$$Q_R = \sigma\varepsilon\left(T_{Cylinder}^4 - T_{air}^4\right) \quad 5.1$$

Where σ = Stefan-Boltzmann constant = $5.6704\ x\ 10^{-8}$ W/m^2/K^4

ε = emissivity = 95% (Li & Ito, 2014b)

Q_R = radiative heat flux (W/m^2)

$$Q_{conv} = h_{conv}(\Delta T) \quad 5.2$$

Where Q_{conv} = convective heat flux

h_{conv} = convective heat transfer co-efficient ($Wm^{-2}\ K^{-1}$)

To determine if radiative effect of the heat transfer should be included directly in the CFD simulation, an approximation was made of both the radiative and convective heat fluxes using equations 5.1 and 5.2 respectively. Radiation would thus be included in the CFD simulation if the radiation heat flux is of the same order or greater than the convective heat flux as advised in the Ansys theory workbook (Ansys, 2016a).

The aim of this thesis is to determine the convective heat transfer co-efficient. However, an estimate was needed to determine if the radiative heat flux should be included in the CFD simulation. Seeing to the fact that the cylinder dimensions mimic that of a standing human

model, we make a well educated guess from literature for use in equation 5.2. The value of $h_{conv} = 4.5\ Wm^{-2}\ K^{-1}$ was used as seen in works by de Dear *et al*. (de Dear *et al*., 1997).

The radiation heat flux was seen to be relatively low due to the very low temperature difference – 3K – used in this paper for turbulent flow and that – maximum of 20 K – used for non-turbulent flow as seen in section on natural convection. For this reason, radiative heat flux was accounted for during the analysis using equation 5.1, and was not included in the CFD simulation. In addition to this, the wall boundary conditions were all set as fixed temperatures, furthermore eliminating the need for a radiation analysis in the CFD simulation.

5.5 CONVECTIVE HEAT TRANSFER COEFFICIENTS ANALYSIS

$$h_{conv} = \frac{Q_{conv}}{A * \Delta T} \qquad 5.3$$

Where h_{conv} = convective heat transfer co-efficient ($Wm^{-2}\ K^{-1}$)

A = Total surface area of the cylinder (m^2)

ΔT = Temperature different between the surrounding and the cylinder (K)

Q_{conv} = Convective heat Flux (W/m^2) = $Q_T - Q_R$

Q_T = Total heat Flux (W/m^2)

Q_R = Radiative heat Flux (W/m^2)

The convective heat transfer coefficient was determined from the formula shown in equation 5.3. Here, the convective heat flux in the equation was determined from the difference between the total heat flux and radiative heat flux (calculated using equation 5.1) as the effects of conduction is assumed negligible in this paper.

6 RESULTS AND DISCUSSIONS

The flow field of the cylinder in the computational domain as observed in the CFD simulation are presented in this chapter. It is then followed by the results of the CFD simulation carried out as described in the previous chapter. The effects of wind velocity and the wind turbulence intensity on the convective heat transfer coefficients (h_{conv}) are then discussed using the presented results. This is followed by presenting proposed equations for determining the h_{conv} accounting for wind velocities and turbulence intensities. Comparison of the results gathered from the CFD simulation and the proposed equations are compared to works found in different literature and discussed. The chapter is brought to an end by conducting a similar analysis on the cylinder for the 3 different positions in a natural convection set up while varying temperature difference. An equation is also proposed for the prediction of h_{conv} for natural convection.

6.1 FLOW FIELD

The flow field for the cylinder in the three different positions during simulations are shown in Figures 6.1 – 6.3.

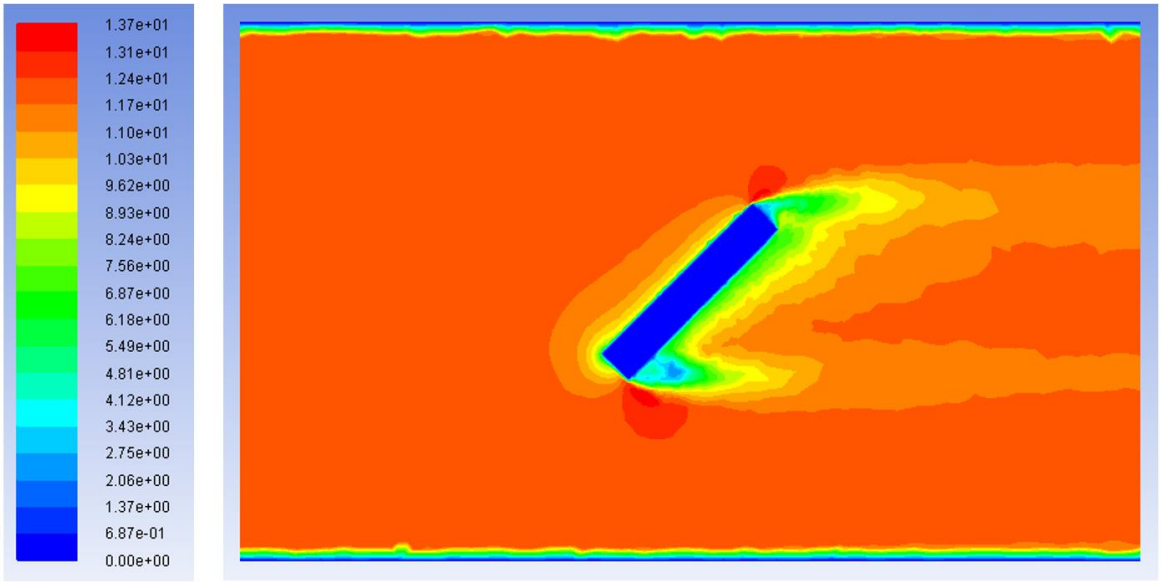

Figure 6.1 Contours of Velocity Magnitude for Inclined Cylinder

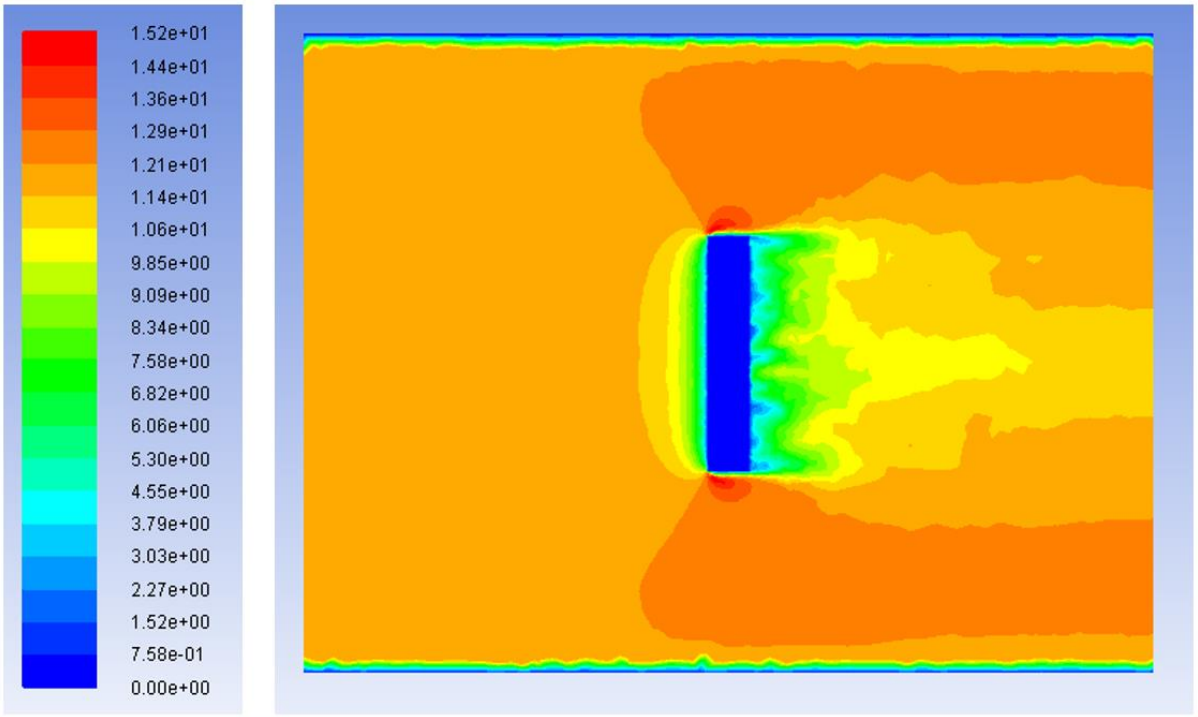

Figure 6.2 Contours of Velocity Magnitude for Upright Cylinder

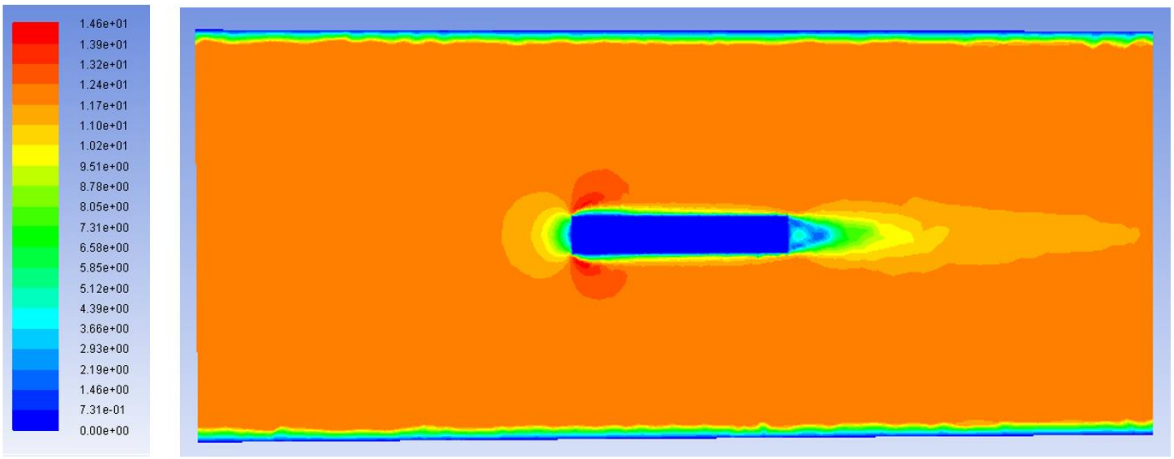

Figure 6.3 Contours of Velocity Magnitude for Supine Cylinder

As seen in Figure 6.2, for the cylinder in the upright position, the flow pattern of the wind was separated by the cylinder, resulting in a stagnant flow region behind the effective surface area of the cylinder. This same behaviour is noticed for the cylinder in the inclined position. For the inclined position however, it appears that the stagnant flow region on the wake side of the flow was somewhat greater than that of the cylinder in the upright position, though not by much. This can be attributed to the fact that due to the inclination of the cylinder, there is a larger effective surface area against the inlet wind flow compared to the cylinder in the

upright position as the base of the cylinder now contributes to the effective surface area. This would explain why there seems to be a more uniform flow for the cylinder in the supine position, seeing as it has a relatively smaller effective surface area to the inlet wind flow, resulting in a smaller region of stagnant flow behind the effective surface area facing the inlet wind flow. This was the general behaviour of the flow over the cylinder as expected, even while varying the wind velocity and the TI.

6.2 REPRESENTATIVE TIME PLOT

Figure 6.4 shows a representative time graph which describes the time profile of the cylinder cooling at different velocities. This was taken from results for the simulations of the cylinder in the standing position under turbulent flow conditions with turbulence intensity of 10%. In Figure 6.4, the time-axis is multiplied by a factor 52.5 as suggested by the Fluent CFD Post for ease of data manipulation for the CFD Post (ANSYS post processing software). Figure 6.4 is representative of the cooling profile of the cylinder in the different cases analysed in this thesis. From Figure 6.4, it is evident that as the air inlet velocity is increased, the rate of cooling of the cylindrical model is increased. However, keeping the turbulence intensities constant, as the inlet velocity increases, the change in rate of cooling approaches 0. This indicates that increasing the inlet velocity to increase rate of cooling is only effective up until a certain velocity x.m/s ($x > 12$), after which the increase in rate of cooling is negligible. The effect of velocity increase on the rate of cooling of the cylindrical model is not a direct objective of this thesis, thus this phenomenon was not explored any further. There is no direct implication on the convective heat coefficient of the cylindrical body from this observation.

As lower temperatures are approached by the cylindrical model, the cylinder takes a longer time to cool. This behaviour is consistent throughout the range of velocities v, from 2 m/s – 12m/s. However, the lower the temperature, it was observed that cooling of the last 0.5K – that is cooling from 304.5 K to 304.0K – takes a considerable amount of time as the slope of the graphs approaches 0 as seen in figure 6.4. To hasten the data gathering process to some degree, all data was gathered at 304.5K thus the overall temperature difference worked with in this thesis is 2.5K as opposed to the initial suggested 3.0K. This change in temperature difference has no effect on the analysis being carried out in this thesis paper.

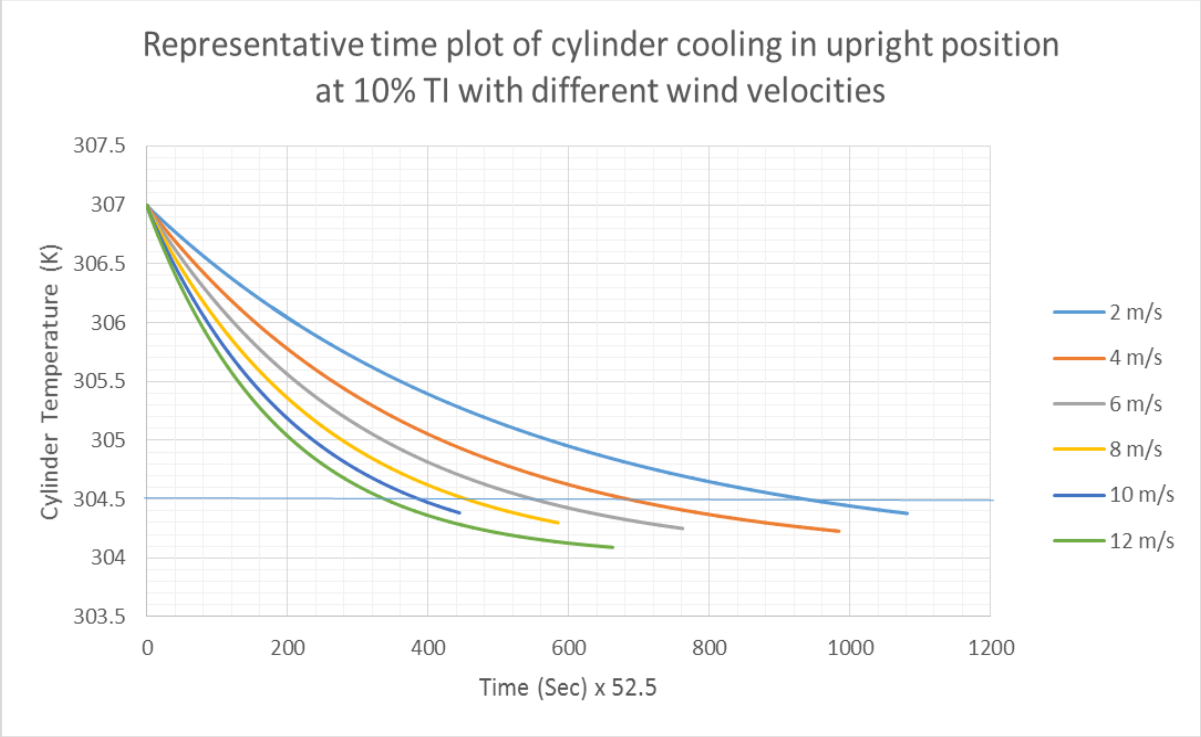

Figure 6.4 Time graph of the cylinder cooling in the upright position

6.3 RESULTS AND EFFECTS OF WIND VELOCITY ON h_{conv}

The results of the effect of wind velocity on h_{conv} are presented graphically below for the cylinder in the upright, supine and inclined positions exploring different turbulence intensities.

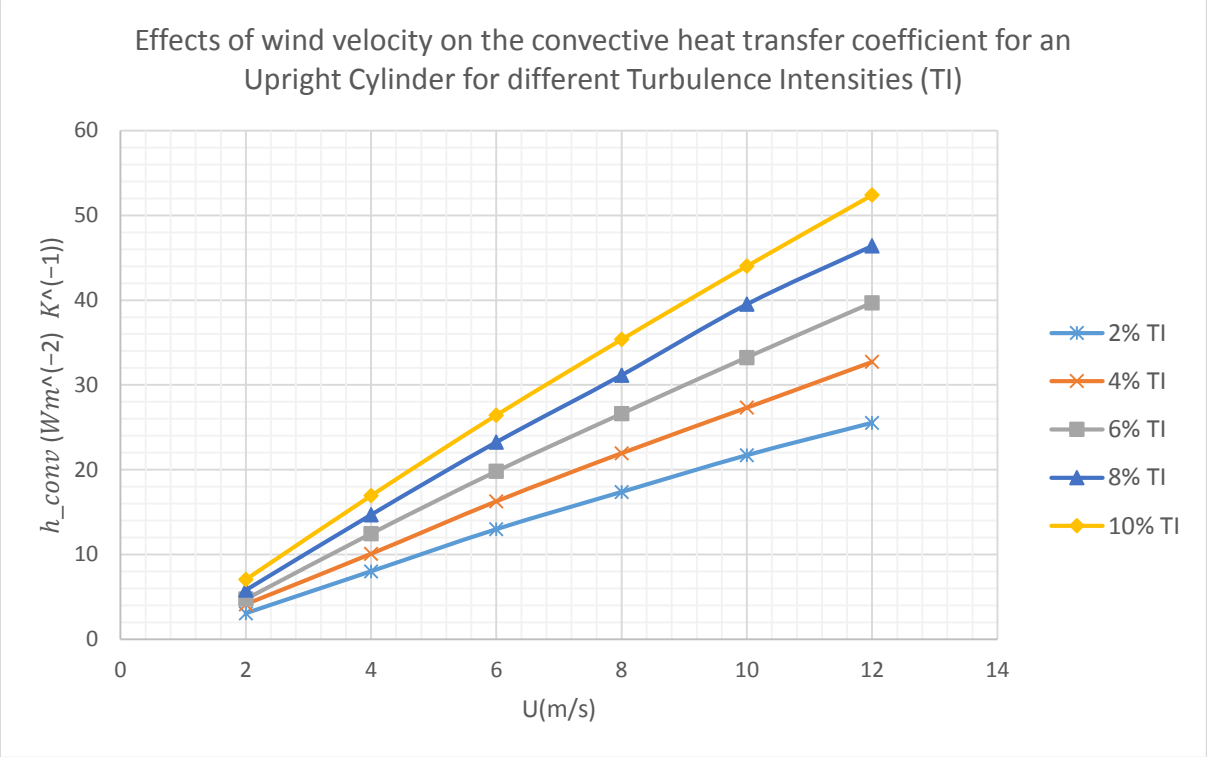

Figure 6.5 Effect of wind velocity on convective heat transfer coefficient for upright cylinder

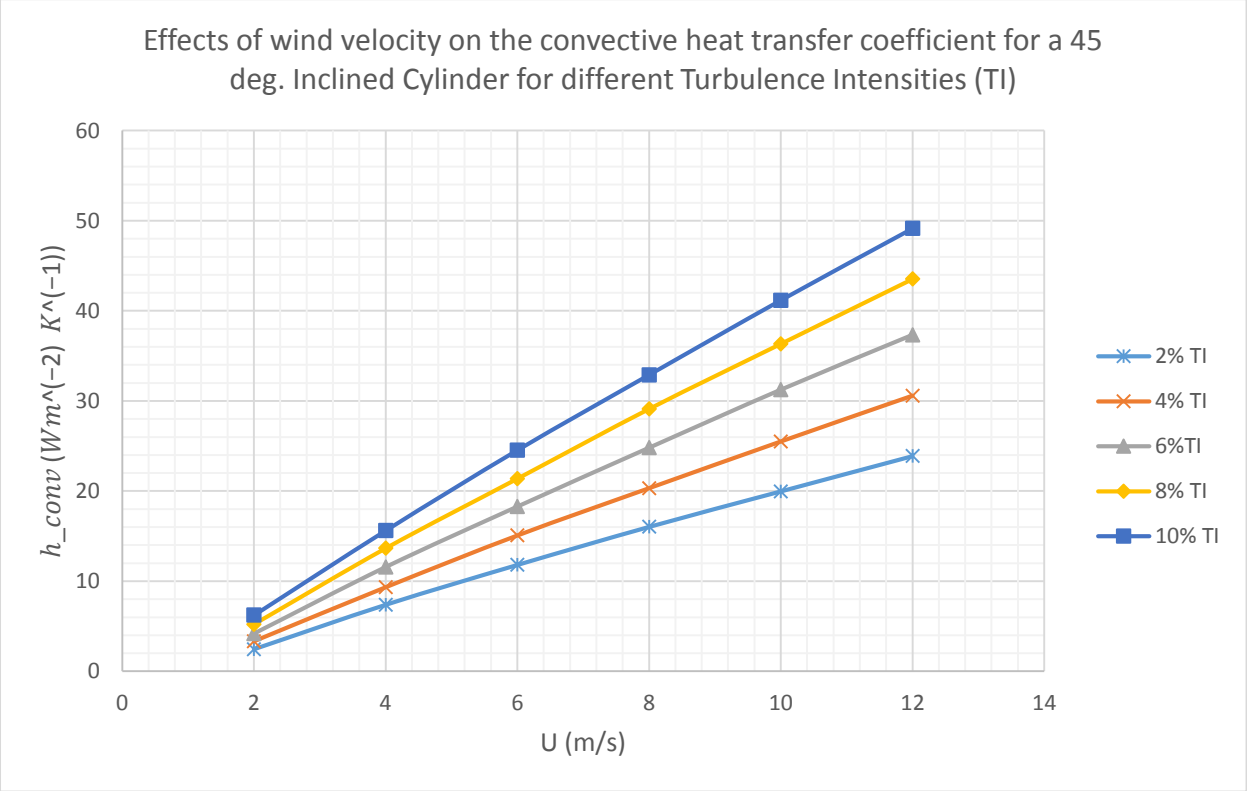

Figure 6.6 Effect of wind velocity on convective heat transfer coefficient for inclined cylinder

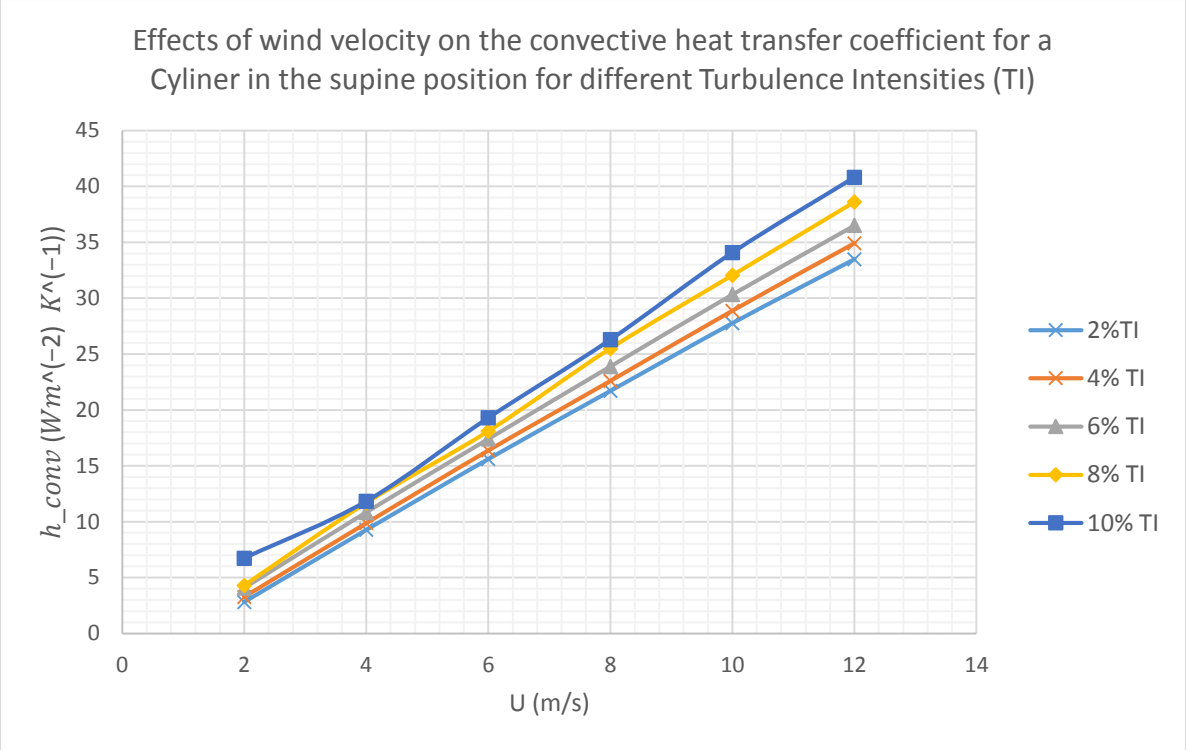

Figure 6.7 Effect of wind velocity on convective heat transfer coefficient for supine cylinder

Analysing the plots of h_{conv} for the cylinder in the 3 different positions with varying turbulence intensities and increasing wind velocities, as shown in Figure 6.5 – 6.7, we see that as velocity increases, so does h_{conv}. This behaviour is similar across all cases analysed, and is expected as it is in agreement with Newton's law of cooling (equation 1.1).

The distribution of the h_{conv} around the cylinder was confirmed as non-uniform, with larger values of h_{conv} (calculated using velocity magnitudes in this regions) seen in the regions of the flow field experiencing higher wind velocities – typically the effective surface area of the cylinder facing the inlet wind flow. This non-uniform distribution of h_{conv} is consistent with works in literature. Cong Li *et al*. (Cong & Kazuhide, 2012) reported that regions of high wind velocity in the flow fields displayed a higher h_{conv} with regions of low wind velocity displaying lower h_{conv}. Similar observations were also reported by Kurazumi *et al*. (Kurazumi *et al*., 2003), Hardy *et al*. (Hardy & Dubois, 1937) amongst others.

Comparing the results of all three use cases analysed as shown in Figure 6.88 while keeping turbulence intensity constant, it is observed that with an increasing effective surface area facing the inlet wind flow, h_{conv} decreases almost exponentially. This allows for the maximum h_{conv} to be experienced for the cylinder in the supine position, as it has the least effective

surface area facing the inlet wind flow, while the cylinder in the inclined position has the least h_{conv} as it displays the highest effective surface area. Thus, higher values of h_{conv} are observed for positions where the effective surface area facing the inlet velocity is higher as described in section 6.1.

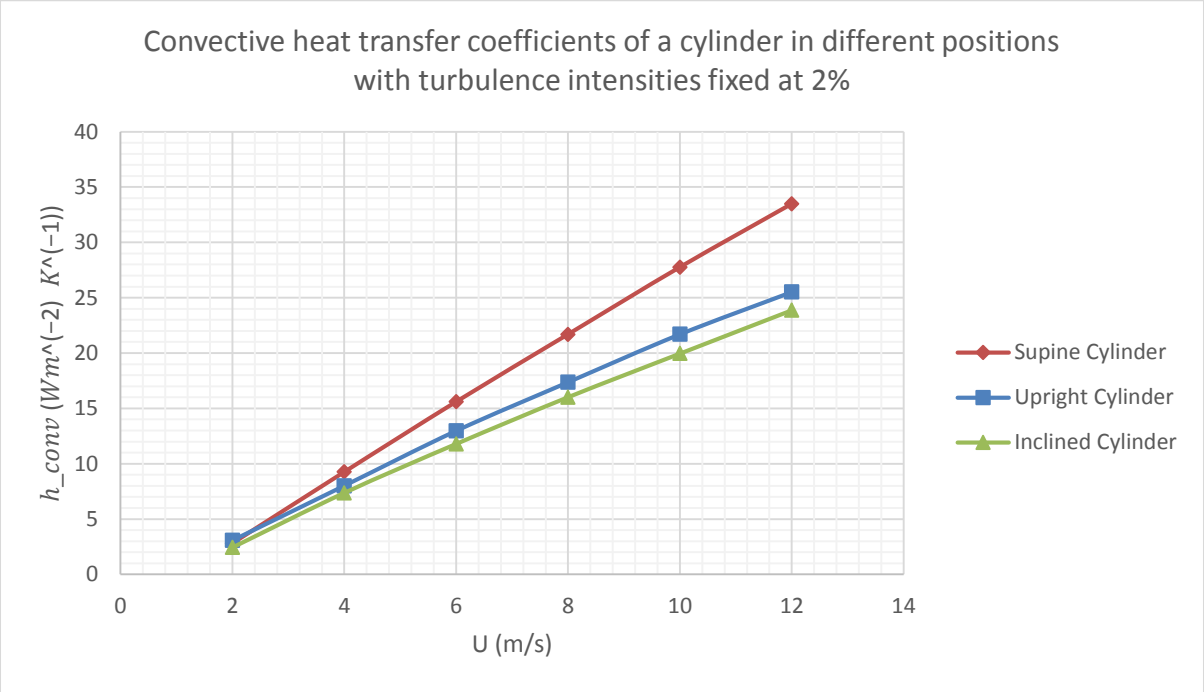

Figure 6.8 Effect of cylinder position on convective heat transfer coefficient for cylinder in 3 different positions

Thus a favourable position for the cylinder to obtain a minimum h_{conv} would be the cylinder in the inclined position. This is confirmed true for turbulence intensity of 2% as seen in Figure 6.8. That being said, it should also be noted that this is not necessarily true for turbulence intensities of higher values. The effect of turbulence intensity on h_{conv} is discussed next.

6.4 RESULT AND EFFECTS OF TURBULENCE INTENSITY ON h_{conv}

Figure 6.9 shows the effect of turbulence intensity on h_{conv} of the cylinder for the 3 different cases analysed for 10% turbulence intensity, being the maximum TI cases analysed.

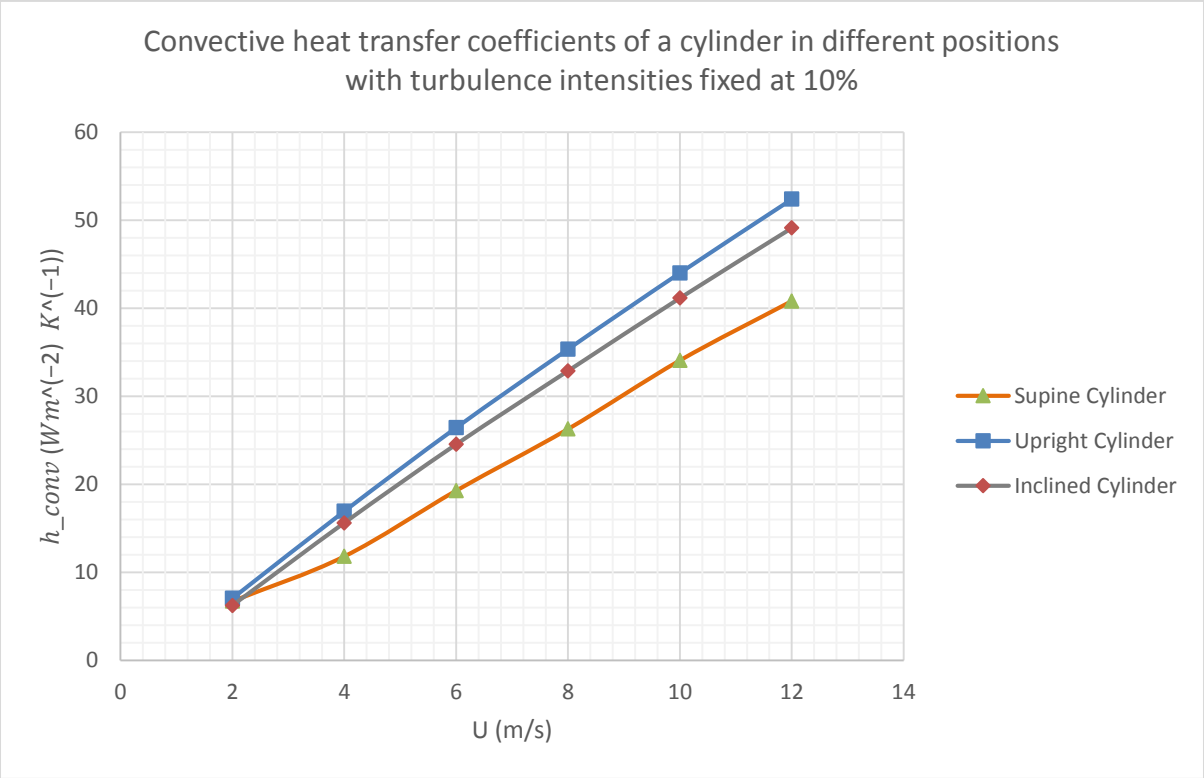

Figure 6.9 Effect of Turbulence Intensities on convective heat transfer coefficient for cylinder in 3 different positions

Here we see an opposite behaviour to that observed for a TI of 2% in the preceding section. The cylinder in the supine position displays the lowest h_{conv}, while the cylinder in the upright position shows the highesth_{conv}, exactly opposite to the patterns observed for TI of 2% everything else remaining the same. At TI of 10%, Cong Li *et al* (Cong & Kazuhide, 2012) did report a similar behaviour with the supine position displaying the lowest h_{conv}. Though they used a numerical human model, it still does confirm the fact that positioning of the geometric shape with respect to the inlet velocity does have a considerable effect on the convective heat transfer of heat. This behaviour of the supine position being favourable to convective heat transfer is also shown in the works by Kurazumi *et al* (Kurazumi *et al*., 2008b), which is cited by most works on convective heat transfer in recent years.

As shown for all 3 cases, it was confirmed that with increasing turbulence intensity, we see an increase in h_{conv}, while keeping the position of the cylinder and wind direction fixed. From

the data gathered and analysed in this paper, it is apparent that the turbulence intensity of the inlet velocity does play a significant role in determining the h_{conv}. In literature, works exploring the effect of turbulence intensity is not easily encountered as most researches focus on natural convection, however, some of the works that explore the effect of turbulence intensity include works by, Kondjoyan *et al* (Kondjoyan & Daudin, 1995) where they focused on cylindrical shapes similar to the objectives of this paper. Cong Li *et al* (Cong & Kazuhide, 2012) also explores the effects of turbulence intensity on h_{conv} though focusing on the human body geometry. The results from both these two papers agree with the observations made here, that as turbulence intensity increases, so does h_{conv}.

6.5 PROPOSED FORMULA FOR DETERMINING THE CONVECTIVE HEAT TRANSFER COEFFICIENT AS A FUNCTION OF WIND VELOCITY FOR TURBULENT FLOW

In literature texts, there exists numerous attempts at defining an accurate predictive formula for determining the convective heat transfer coefficients for a body under turbulent flow. These can be seen in works published by Li *et al*. (Li & Ito, 2014a), de Dear *et al* (de Dear *et al*., 1997) amongst others.

$$h = aU^b \qquad 6.1$$

Where $h = h_{conv}$

$U = wind\ velocity$

'a' and 'b' $= coefficients$

The general form for the empirical predictive formulas typically take the form of equation 6.1 and are usually determined from simulations using the geometry of the human body in different positions as opposed to work being done in this paper on a cylindrical geometry in different positions.

The range of velocities (2m/s – 12m/s) used for the numerical simulations of the cylinder in this paper are for forced convection as discussed in preceding sections. A wide enough range of velocities for each cylinder positions analysed enables a sufficient statistical regression relationship between the convective heat transfer coefficient" h_{conv}" and wind velocity "*U*" for different turbulence intensities.

$$h_{conv} = aU - b \qquad 6.2$$

Where h_{conv} = Convective heat transfer co-efficient

U = inlet wind velocity

'a' and 'b' = coefficients

The form of the prediction formula for the work done in this paper takes a linear form as seen in equation 6.2 as this gave reasonably high R^2 values from the regression analysis.

The values for coefficients 'a' and 'b' are displayed in Table 6.1 for different turbulence intensities values for the cylinder in 3 different positions. Figure 6.10 shows the graphs of h_{conv} plotted using the predictive formula proposed in equation 6.2 along with coefficients 'a' and 'b'. The general trend of the graphs is in agreement with the data gathered from the CFD simulations as expected seeing that all R^2 values were above 99%.

Table 6.1 Prediction Formula Co-efficient for turbulent flow

Cylinder Position	Turbulence Intensity (%)	Co-Efficient		R Squared
		a	b	
Upright	2	2.2535	1.0019	0.9977
	4	2.8631	1.2992	0.9992
	6	3.4829	1.6228	0.9988
	8	4.0756	1.7243	0.9986
	10	4.5276	1.325	0.999
Inclined	2	2.1304	1.3352	0.9981
	4	2.7153	1.6592	0.9989
	6	3.3035	1.8908	0.9991
	8	3.8194	1.8676	0.9992
	10	4.28	1.7003	0.9991
Supine	2	3.0709	3.0621	0.9996
	4	3.1655	2.8448	0.9998
	6	3.2453	2.2159	0.9998
	8	3.4306	2.3079	0.9996
	10	3.4892	-1.2552	0.9973

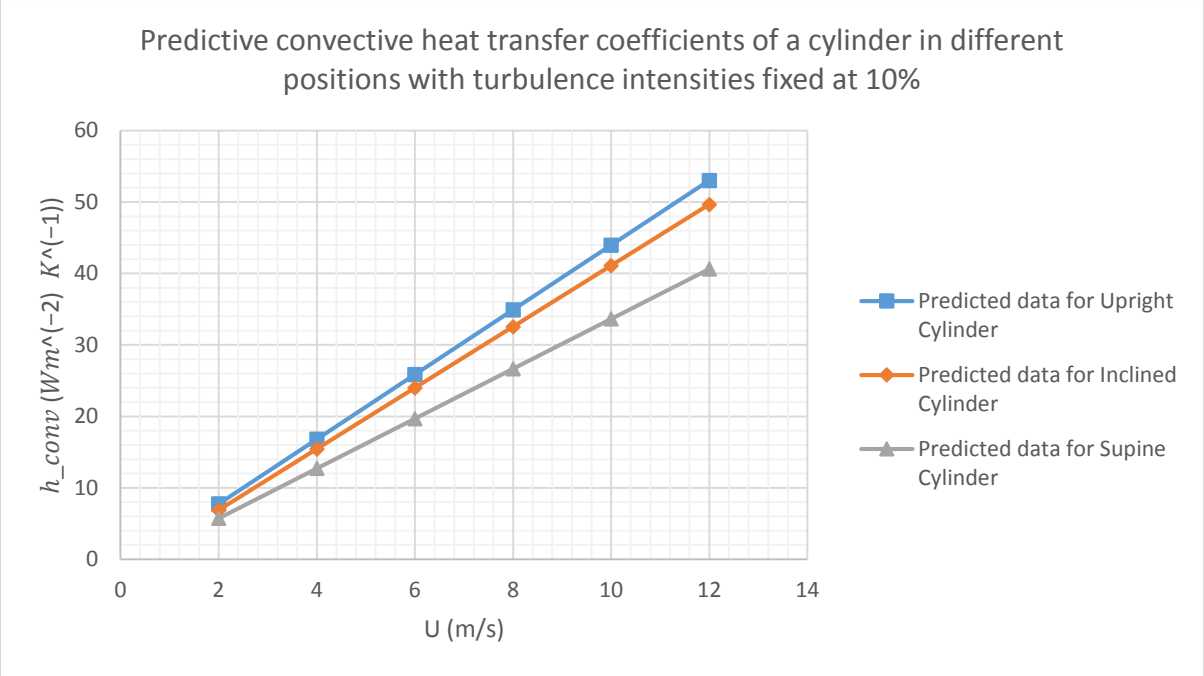

Figure 6.10 Convective heat transfer coefficient plotted using the predictive formula for cylinder in different positions

6.6 RESULTS VALIDATION FOR TURBULENT FLOW

Figure 6.11 shows comparison of the results gathered in this paper to results from literature.

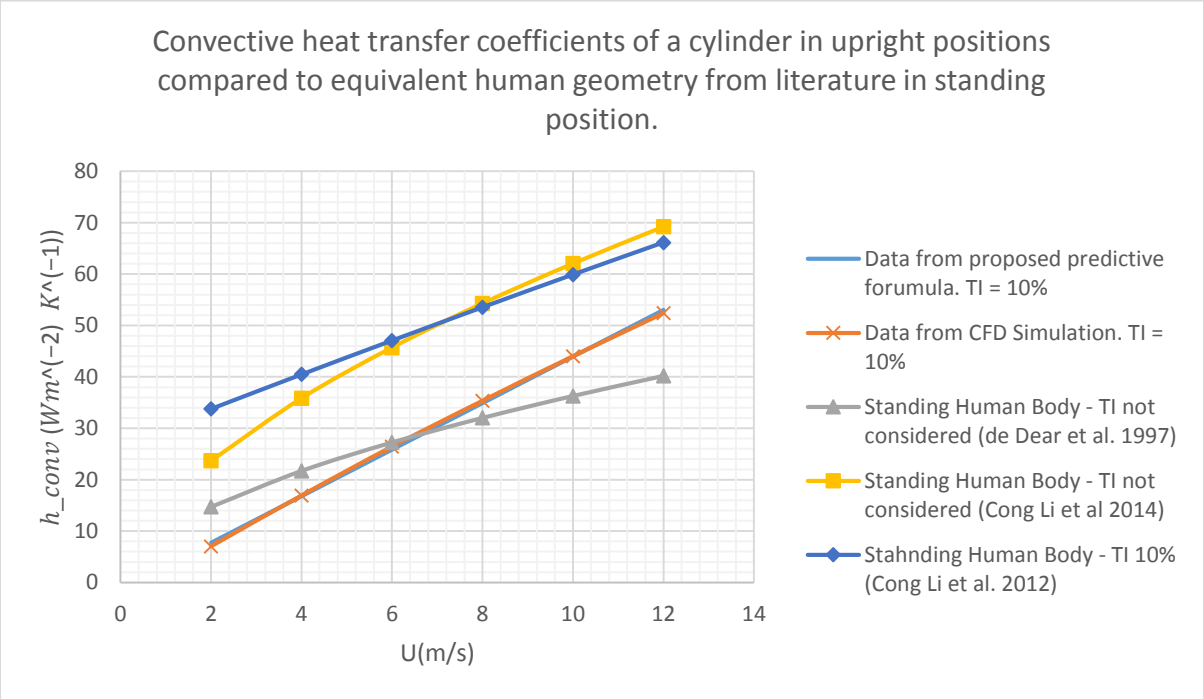

Figure 6.11 Comparison of results gathered from CFD simulations to results from predictive formula to results from literature for turbulent flow

It confirms that works carried out in this paper is consistent with work in literature. It should also be noted that we didn't have to worry about effective convective heat transfer area (the arm pits for example wouldn't be involved in calculations of h_{conv}) as in with the human body as we assumed that the full cylinder was involved in the convective heat exchange process. This is understandably seeing that we have no hidden surface areas from the approaching fluid flow. The effect of temperature gradient on the convective heat transfer coefficient is explored for the cylinder undergoing laminar flow in later sections of this chapter.

6.7 ANALYSIS OF h_{conv} OF THE CYLINDER FOR NATURAL CONVECTION

As detailed in opening sections of this chapter, for wind velocity below 0.941m/s, the cylinder experiences laminar flow. That being said, it was seen for wind velocities inciting natural convection, a change in the wind velocity as it approaches 0m/s has very little effect on the convective heat transfer coefficient (h_{conv}). For this reason, in literature it is difficult to find an analysis of h_{conv} for natural convection based on the effects of wind velocity. This was confirmed by carrying out analysis for the cylinder in the upright position for laminar flow velocities considering effects of wind velocity. The results are shown in Table 6.2 and plotted in Figure 6.12. The graph plotted shows the instability of the effects of wind velocity at very low temperatures.

Table 6.2 Results for the effect of wind velocity of upright Cylinder under laminar flow

Wind Velocity	Total Surface Heat Flux_average	Radiative Heat Flux_average	Convective Heat Flux	Convective Heat Transfer Co-Eff
0.05	43.99	35.98	8.01	0.4005
0.2	43.62	35.98	7.64	0.382
0.4	44.02	35.98	8.04	0.402
0.6	43.55	35.98	7.57	0.3785
0.8	43.84	35.98	7.86	0.393

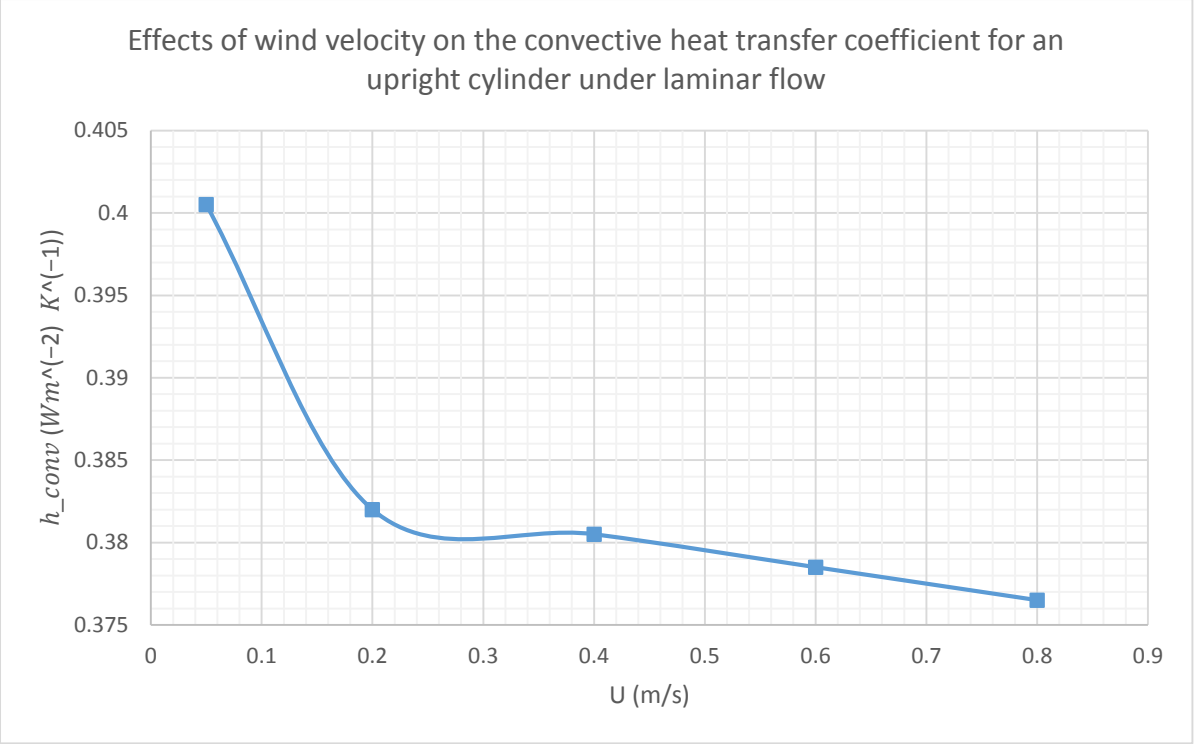

Figure 6.12 Effects of wind velocity on the convective heat transfer coefficient for an upright cylinder under laminar flow

Thus, when it comes to natural convection, unlike previous sections of this chapter, a more useful analysis would be to study the effects of temperature difference between the cylinder and the surrounding on h_{conv}. In literature, most researchers analyse scenarios dealing with effects of posture - Kurazumi *et al*.(Kurazumi *et al*., 2008b), effects of temperature difference - Virgilio *et al*. (Virgilio *et al*., 2012), amongst other factors. In this paper, we would analyse the effect of temperature difference between the cylinder and the surrounding and the effect of the cylinder position with respect to wind direction (posture with regards to the human body). The same computational model used for the CFD analysis for turbulent flow as used above is used here. The boundary conditions however are changed as shown in Table 6.3.

Table 6.3 CFD Simulation Parameters for laminar flow

Item	Dimensions
Cylinder	Height = 1.736 m Diameter = 0.2934 m Surface Area = 1.74 m^2 Volume = 0.12 m^3 (0.064 in lit review - Cong & Kazuhide, 2012) Constant tempt. = 34 deg. (307 K) Variations (3 cases)

	• Upright • Inclined at 45 degrees and • Supine Cylinder For each case, the temperature of the cylinder is varied from 291 K to 307K to allow for 5 different temperature differences (5 cases).
Surrounding Domain	Width = 3m Height = 3m Length = 6m Cylinder position = 3m from inlet Wall tempt. = 30 deg. (304 K)
Air at 287K	Density = 1.1644 kg/m^3 Dynamic viscosity = 1.8885 exp -5 kg/(m.s) P = 101325 pa Re = 4252.2 x Velocity. Thus, for velocity greater than 0.941m/s, Re > 4000, thus turbulent. <u>Variations</u> • No variations for natural convection

Using the parameters as described in table 6.3, the Reynolds number, Re is computed as 4252.2v, where v = velocity. Thus, for velocities greater than 0.941m/s, Re > 4000, thus turbulent.

6.7.1 EFFECTS OF TEMPERATURE DIFFERENCE ON h_{conv} FOR LAMINAR FLOW

The results of the effect of temperature difference on h_{conv} are presented graphically below for the cylinder in the upright, supine and inclined positions for velocity v = 0.1m/s.

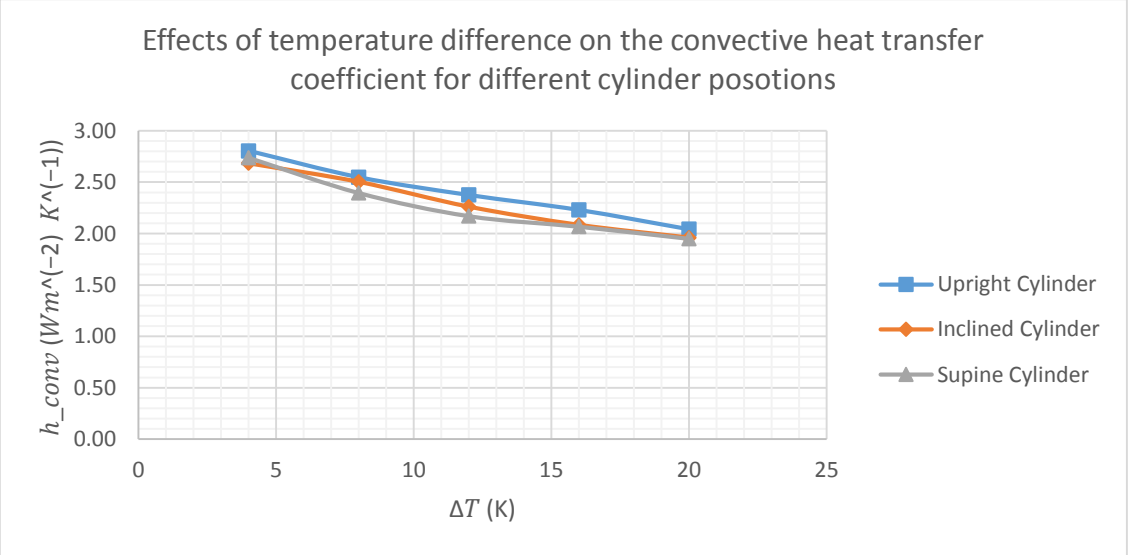

Figure 6.13 Effects of temperature difference on the convective heat transfer coefficient for different cylinder positions

Analysing the plots of h_{conv} for the cylinder in the 3 different positions with varying temperature difference as shown in Figure 6.13, we see that as the temperature difference increases, a decrease in the h_{conv} of the cylinder is observed. This behaviour is similar across all cylinder positions analysed for laminar flow as seen in the presented figure 6.13. Interestingly however, this is not the normality in literature. In literature, as seen in works by Virgilio *et al*. (Virgilio *et al*., 2012) amongst others, the h_{conv} of the cylinder is seen to increase with increasing temperature difference between the body and the environment

$$\dot{Q} = hA(T_a - T_b) \qquad 6.3$$

. It is difficult to find works with the reverse order where the h_{conv} is seen to decrease with increasing temperature difference even though this is in line with Newton's law of cooling as it applies to convection as seen in equation 6.3. One of such works in agreement with Newton's law of cooling as well as results presented din this paper is works by Nishi *et al* (Nishi & Gagge, 1970). In their works, they used the method of naphthalene sublimation as explained in the literature survey of this thesis (section 2.2.2).

It is not exactly clear the reason for this difference in the result trend. It should be noted however that of all the methods in literature, none was done computationally for laminar flow, the works on laminar flow were mostly carried out on thermal manikins. That being said, accuracy of experimental methods can be considered one of the possible reasons for difference in results trends. The same models and similar simulations procedures as used for the turbulent simulations were used for the laminar simulation, thus ruling out the possibility of a wrong CFD model or simulation procedure as those results were sufficiently validated as shown in previous sections. Asides the results trends, the figures of the h_{conv} were of reasonable magnitudes compared to previous works in literature as can be seen in Figure 6.15. Figure 6.14, is taken form the works of Kurazumi *et al*. (Kurazumi *et al*., 2008b) showing a more detailed comparison of the various works in literature on h_{conv} of a body.

Further, works by Nishi et al. (Nishi & Gagge, 1970) is outlined as their work displays similar trend to that seen in this paper. The results from their work is plotted on the same figure as the result from works in this paper for comparison. This is shown in Figure 6.15. Though a similar trend as seen in their work is observed in this thesis, a higher convective heat transfer

coefficient – 62% on average – is observed in this thesis. The reason for this large difference in convective heat transfer coefficient is largely due to the method used in their works. In their works, Nishi et al. (Nishi & Gagge, 1970), the naphthalene sublimation method (described in section 2.2.2 of this thesis) which doesn't account for the total surface area of the body was employed. In addition their work was also purely experimental, while works in this thesis have been purely computational, allowing for better accuracy.

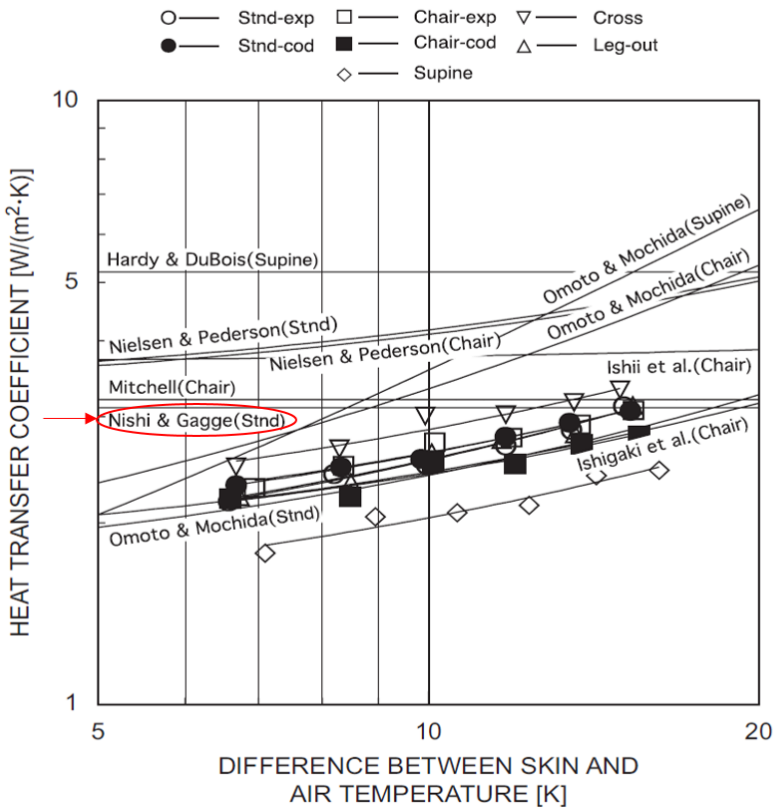

Figure 6.14 Trends of CHTC as seen in literature

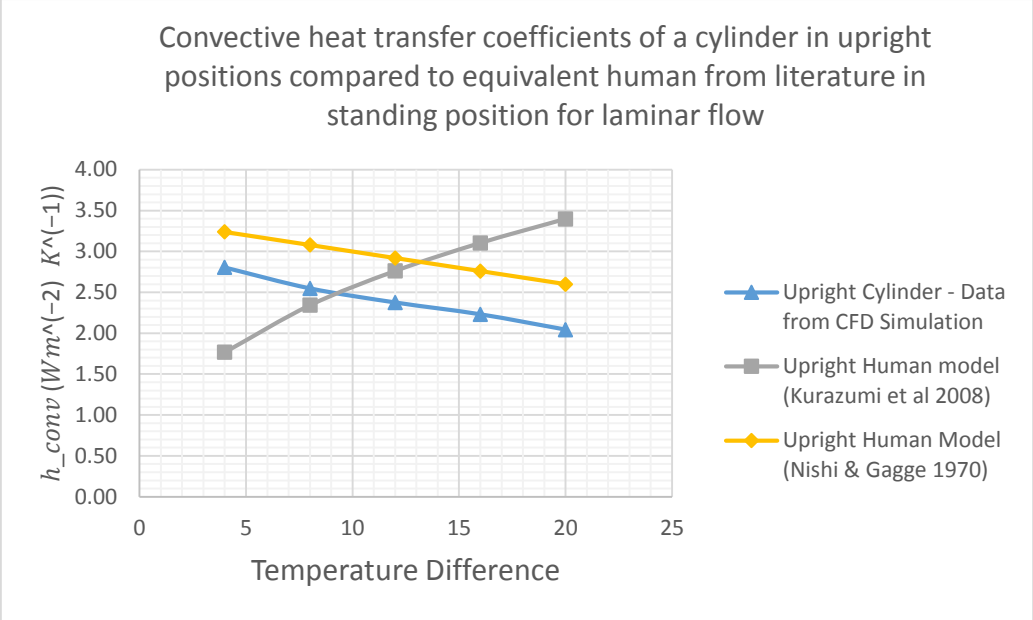

Figure 6.15: Comparison of results gathered from CFD simulations results from literature for Laminar flow

For laminar flow, the correlation between the effective surface area facing the inlet wind flow and h_{conv} is not as observed for turbulent flow. Here, a larger effective surface area facing the inlet flow does not necessarily equate to a lesser h_{conv} as seen in previous sections for turbulent flow. As Figure 6.13 shows, the favourable position for a minimum h_{conv} is the cylinder in the supine position while the cylinder in the upright position displays the maximum h_{conv}. This is in accordance with literature as seen in works by Virgilio *et al* (Virgilio *et al*., 2012), Kurazumi *et al*. (Kurazumi *et al*., 2008b) to mention a few. The cylinder in the inclined position displays values of h_{conv} in between that of the supine and the upright position. These results insinuates that the h_{conv} of the cylinder is not dependent on the effective surface area for laminar flow as it applies for turbulent flow – at least for the velocity (0.1m/s) the simulations were carried out at in this thesis.

6.8 PROPOSED FORMULA FOR DETERMINING THE CONVECTIVE HEAT TRANSFER COEFFICIENT AS A FUNCTION OF WIND VELOCITY FOR LAMINAR FLOW

There exists a sufficient amount of text in literature with proposed equations for the convective heat transfer coefficient of a body especially for laminar flow. For laminar flow which is the focus of this section, most researchers find a correlation between the temperature gradient and h_{conv}. This can easily be seen in the works of Kurazumi *et al*.

(Kurazumi *et al*., 2008b) whose work is widely referenced by other researchers for works on laminar flow. In his work, the proposed equation takes the form of equation 6.4. The form of the prediction formula for the work done in this paper takes a similar form, giving reasonably high R^2 values from the regression analysis as shown in Table 6.4.

$$h = a\Delta T^b \qquad 6.4$$

Where $h = h_{conv}$

ΔT = *temperature difference between the cylinder and the surrounding air*

'a' and 'b' = *coefficients*

The values for coefficients 'a' and 'b' are displayed in Table 6.4 for the cylinder in 3 different positions. Statistical regression analysis between the convective heat transfer coefficient" h_{conv}" and temperature gradient "ΔT" was carried out for the cylinder in 3 different positions.

Table 6.4 Prediction Formula Co-efficient for laminar flow

Cylinder Position	Co-Efficient		R Squared
	a	b	
Upright	3.7040	-0.188	0.9606
Inclined	3.6304	-0.198	0.9507
Supine	3.6753	-0.210	0.9975

Figure 6.16 shows the graphs of h_{conv} plotted using the predictive formula proposed in equation 6.4 along with coefficients 'a' and 'b'.

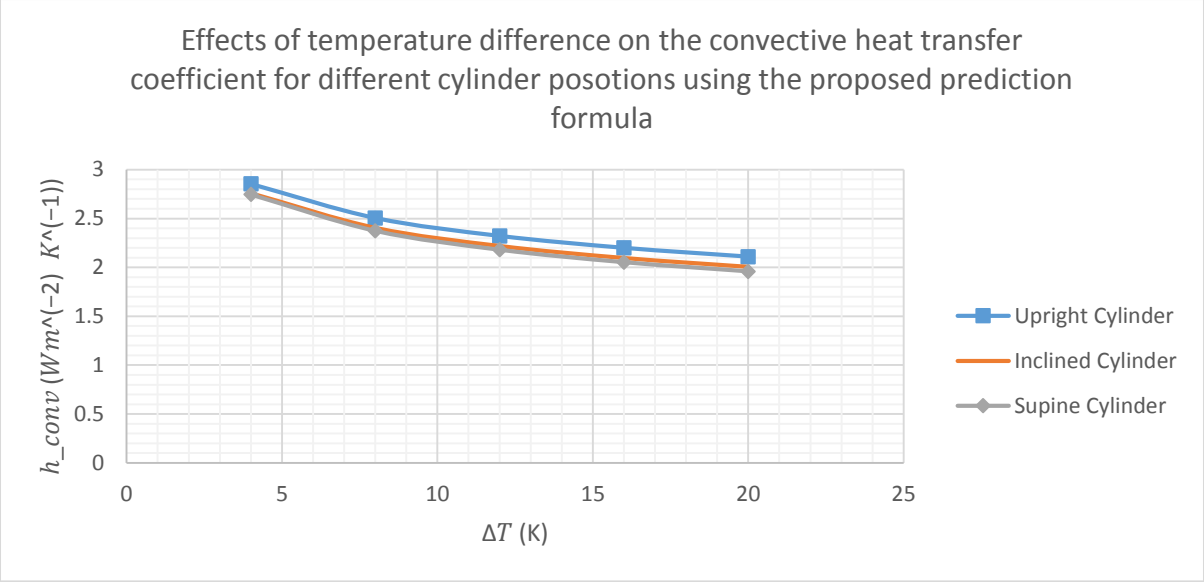

Figure 6.16 Effects of temperature difference on the convective heat transfer coefficient for different cylinder positions using the proposed prediction formula

The general trend of the graphs is in agreement with the data gathered from the CFD simulations as expected seeing that all R^2 values were above 95%. This is seen clearly in the superimposed graphs of the gathered CFD data and the data from the proposed formula for the convective heat transfer coefficient shown in Figure 6.17.

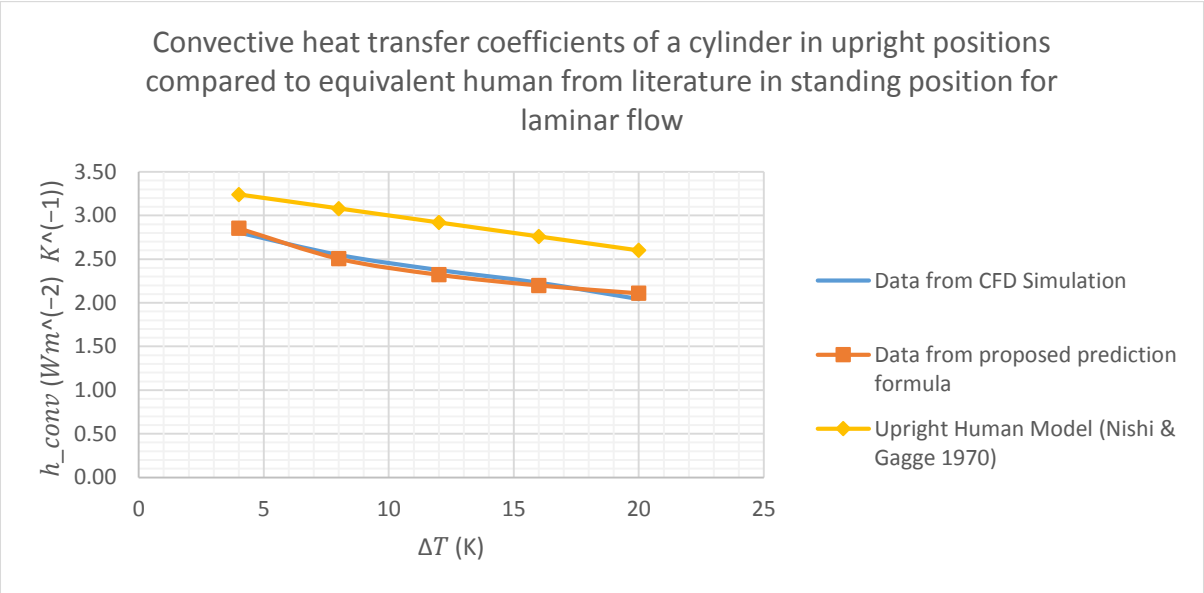

Figure 6.17: Comparison of results gathered from CFD simulations to results from predictive formula to result from literature for Laminar flow

6.9 NUMERICAL ACCURACY ASSESSMENT

Figure 6.18 below shows a c comparison of the work carried out in this paper to that of works by Cong Li *et al*. (Li & Ito, 2014a), who's works was the basis of the numerical model of the representative cylindrical model used in this thesis. In their works, they also made use of similar methodology as well as employed the same Software (ANSYS Fluent) for the CFD computations and simulations of their model. The surface area of the cylindrical model used in this thesis as describe in section 5.1, was based on the human model geometry used in their work.

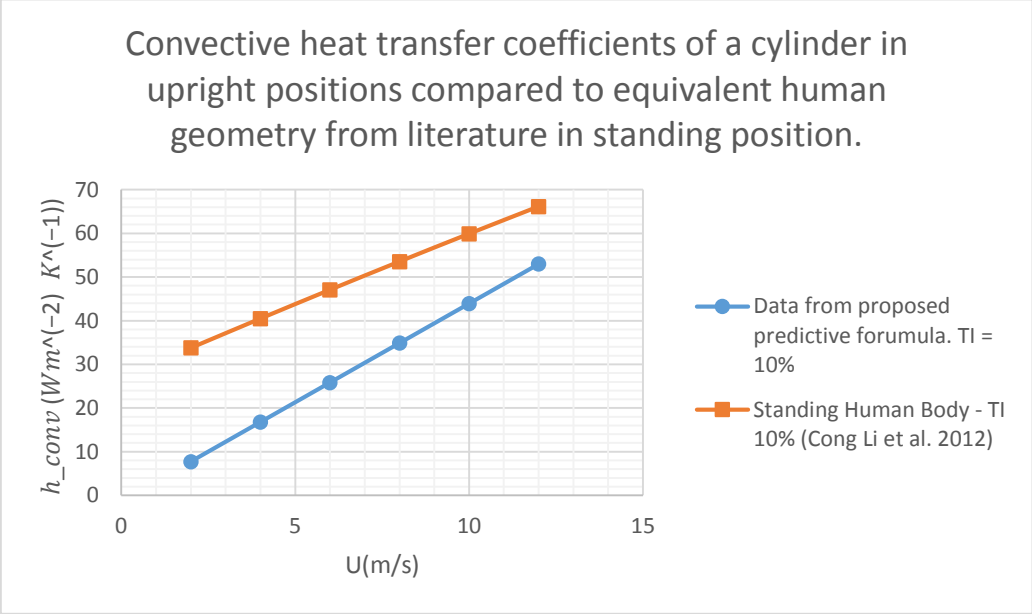

Figure 6.18 Convective heat transfer coefficients of a cylinder in upright positions compared to equivalent human geometry from literature in standing position.

From figure 6.18, there is a considerable difference between the results from their works and works done in this thesis. The deviation is seen to reduce as the velocity increases. This is expected as their works were carried out at high velocities U (U $\geq$ 14m/s). The deviation is also largely due to the direct difference in geometrical model. However, the general trend of the works agree as expected, further confirming the numerical methodology used in this thesis.

Based on guidelines form the ASME editorial on numerical accuracy (ASME, 1994), this comparison of works in this thesis to that of Cong Li et al. (Cong & Kazuhide, 2012), as shown in figure 6.18 and described above provides an acceptable means of numerical accuracy

assessment of results from work in this thesis. This is especially true as Cong Li et al. (Li & Ito, 2014a) have provided a highly accurate approximate analytical solution as well as comparison to experimental data. In their works, they conducted both numerical and experimental estimations of the convective heat transfer coefficient of the human body and made a comparison of both methods where a remarkable similarity of results are seen, with better accuracy seen in the results presented by the works of the numerical simulations. They made use of the commercial fluid flow software package ANSYS/FLUENT which would be employed in works carried out in this paper.

7 SUMMARY, CONCLUSION AND SUGGESTIONS

7.1 SUMMARY

The application of the convective heat transfer coefficient of the human body has been of interest to various industries to analyse the heat exchange between the human body and its thermal environment. The overall objective of this paper was to investigate, develop and verify a framework for determining the convective heat transfer coefficient easily adaptable to more complex geometry.

To do this, a simple cylindrical model representative of the human geometry in height and surface area was chosen based on dimensions from literature. An analysis is carried out for both laminar and turbulent fluid flow scenarios using the numerical simulation approach.

In literature, ample attempts have been made at determining the convective heat transfer coefficients for the human body. At the beginning of this dissertation in chapter 2, relevant results provided by various means in literature for the convective heat transfer coefficient for the human body was provided. This was followed by a look at the relevant theory for the numerical modelling of the fluid flow and heat transfer in chapter 3. In chapter 4, to investigate the framework to be developed, we zoomed into the theory and conducted a mesh generator analysis to better understand and verify the different available upwinding schemes and then an informed decision was made as to what schemes to apply in works carried out in this paper.

Based on the mesh generator analysis conducted, it was verified that the Cubic Upwinding (CUI) scheme produces the most accurate results compared to results seen from other schemes such as the QUICK scheme and the Central Difference Method scheme. However, based on the available options in the chosen CFD software for simulations, the QUICK upwinding scheme was used, being the next available best.

The numerical simulation for both the laminar and the turbulent flow for the representative cylindrical model was modelled using a robust and efficient CFD package, the ANSYS/FLUENT

CFD package. The simulation methodology for this is described in chapter 5 and the results from the simulations were presented and discussed in chapter 6. Comparison of results conducted in this paper are also seen in chapter 6. The result of the attempted framework developed were equations presented in chapter 6 that help define the convective heat transfer coefficient for the laminar and turbulent fluid flow scenarios over the representative geometry.

For the analysis of the convective heat transfer coefficient for laminar flow, a total of 15 cases were analysed varying the cylinder orientation and temperature difference between the cylinder and surrounding temperature. While for the turbulent scenario, a total of 90 cases were analysed, varying cylinder orientation, turbulence intensity and wind velocity.

7.2 CONCLUSION

The works in this paper brings a wealth of previous works in literature on the convective heat transfer coefficient together to have closer look at the behaviour of a body with its thermal environment and what factors affect its convective heat transfer coefficient. The conclusions from the works in this thesis are presented below.

For the convective heat transfer coefficient for the representative cylindrical model, it was seen that for turbulent flow,

- The average convective heat transfer coefficient for the representative cylindrical model increases with increasing wind speed and turbulence intensity. This relationship was seen to be approximately linear based on the proposed equation seen in equation 7.1. Comparison of works in this paper was carried out against similar works in literature and was seen to agree reasonably well.

$$h_{conv} = aU - b \tag{7.1}$$

- The average convective heat transfer coefficient showed a dependence on the orientations of the cylinder based on the direction of the inlet velocity. It was seen that the increase was in relationship to the increase in effective surface area. That is the area directly in contact with the approaching wind. This behaviour was confirmed true for low turbulence intensities while for higher turbulence intensities, the reverse was confirmed.

While, for laminar flow, it was seen that,

- The convective heat transfer coefficient of the representative cylinder was seen to vary with a change in temperature difference between the cylinder surface and the surrounding environment. It was confirmed that a higher temperature difference corresponds to a higher convective heat transfer coefficient. This temperature-dependent behaviours of the convective heat transfer coefficient is confirmed to be exponential and agrees well with previous works in literature. The proposed formula for the works in this paper is presented in equation 7.2 below.

$$h_{conv} = a\Delta T^{b} \qquad 7.2$$

- Also, the effect of the effective surface area of the representative cylinder for the fluid flow on the convective coefficient didn't display a dependent behaviour, where an increase in effective surface area corresponded to an increase in the convective heat transfer coefficient. Thus leaving the cylinder in the supine position to experience the highest convective coefficient for a given temperature difference.
- The convective heat transfer coefficient of the cylinder is not dependent on the effective surface area for laminar flow as it applies for turbulent flow.

The findings in this thesis as described above investigated the convective heat transfer coefficient of the human body provided insights as to the effects of the body configuration on the convective heat transfer coefficient. Formulas for determining the convective heat transfer coefficient were also proposed. These provide an easily adaptable framework for the investigation of the convective heat transfer coefficient, thereby achieving the main objective of the works in this thesis. This framework can easily be adaptable to the human model and would be very beneficial in different industries, the forensic industry being a great example.

7.3 SUGGESTIONS FOR FUTURE WORK

As with most areas in computation today, there is always an area for improvement. This brings about the discussion for optimization. In addition to optimization of the processes already laid out in this paper based on decisions grounded on the physics of the modelling of the fluid flow, possible areas for further research include;

- 3D Human Models; Works with 3D human models with rearrange-able postures mimicking the human body would be an ideal next step to get results better applicable in industry.
- The determinations of the convective heat transfer area for a body; With works in this paper where we employed a relatively simple model, the convective heat transfer area was of little concern as it could safely be assumed that this was the entirety of the cylinder as the model had no hidden surface like gaps between fingers of a human model, the armpits of a human model, contact of the model with the surrounding etc. This is an area very relevant to the development of a framework for the computation of the convective heat transfer coefficient for the human body and literature lacks sufficient texts on this using. Even when works on this are found, questionable approximations are made based on the limitations posed by experimental methods. A study of this using numerical methods would be off great benefit to the works regarding the convective heat transfer coefficient in general.
- The effect of clothing on the convective heat transfer coefficient of the human body; once the numerical simulation processes have been reasonably optimized, a further layer of complexity – clothing – can be added to the modelling of the heat exchange between the human body and its thermal environment. This presents a very complex problem as the materials used for clothing vary considerably and it is futile running simulations for them all. However, a framework can be developed to determine the effect of natural fabrics on the convective heat exchange as their chemical structure is readily available. This framework after rigorous testing and verification can then be applied to fabrics from man-made fibres upon provision of their chemical structure. Such a project would be of topmost benefit to the forensics industry.

8 REFERENCES

Abe, K., Kondoh, T. & Nagano, Y. 1994. *A new turbulence model for predicting fluid flow and heat transfer in separating and reattaching flows—I. Flow field calculations.* Available: http://www.sciencedirect.com/science/article/pii/0017931094901686 .

ANSYS, C. 2003. *Ansys Fluent Theory Guide.* Available: http://jullio.pe.kr/fluent6.1/help/html/ug/main_pre.htm [2017-02-16].

Ansys, I. 2016a. Fluent-Intro. Module 8 - Heat Transfer. (Unpublished).

Ansys, I. 2016b. Mesh Intro - 17.0. M03 Global Mesh Controls. (Unpublished).

Cengel, Y.E. 2007. *Heat and Mass Transfer: a Practical Approach.* Third ed. McGraw-Hill.

Chang, S.K., Arens, E. & Gonzalez, R.R. 1998. Determination of the effect of walking on the forced convective heat transfer coefficient using an articulated manikin. *ASHRAE Transactions. UC Berkeley: Center for the Built Environment.* 94(1):71-82.

Clark, R.P., Mullan, B.J., Pugh, L.G. & Toy, N. 1974. Heat Losses from the Moving Limbs in Running: the 'pendulum' effect. *Journal of Physiol.* Supp: 8p-9p.

Clark, R.P. & Toy, N. 1975. Natural convection around the human head. *Journal of Physiol.* 244:283-293.

Cong, L. & Kazuhide, I. 2012. Numerical Analysis of Convective Heat and Mass Transfer around Human body under Strong Wind. *International Journal of High-Rise Buildings.* 1(2):107-116.

Cong, L. 2013. Heat and Mass Transfer from Human Body Surface in Forced Convective Flow. Ph.D. Thesis. Department of Energy and Environmental Engineering Interdisciplinary Graduate School of Engineering Sciences.

de Dear, R., Arens, E., Hui, Z. & Oguro, M. 1997. Convective and radiative heat transfer coefficients for individual human body segments. *Int J Biometeorol.* 40:141-156.

Du Bois, D. & Du Bois, E.F. 1916. A formula to estimate the approximate surface area if height and weight be known. 1916. *Nutrition (Burbank, Los Angeles County, Calif.).* 5(5):303 - 11-discussion 312-3.

Hardy, J. & Dubois, E. 1937. The Technic of Measuring Radiation and Convection. *Journal of Nutrition.* : 461-475.

Hardy, J. & Soderstrom, G. 1938. Heat loss from the nude body and peripheral blood flow at temperatures of 22°c. To 35°c. *Journal of Nutrition.* 15(5):493-510.

Jiyuan, T., Guan, H.Y. & Chaoqun, L. 2013. *Computational Fluid Dynamics: A Practical Approach.* 2nd Edition ed. U.S.A: Elsevier.

Kondjoyan, A. & Daudin, J.D. 1995. *Effects of free stream turbulence intensity on heat and mass transfers at the surface of a circular cylinder and an elliptical cylinder, axis ratio 4.* Available: http://www.sciencedirect.com/science/article/pii/001793109400338V .

Kurazumi, Y., Tsuchikawa, T., Ishii, J., Fukagawa, K., Yamato, Y. & Matsubara, N. 2008a. Radiative and Convective Heat Transfer Coefficients of the Human Body in Natural Convection. *Building and Environment.* 43:2142-2153.

Kurazumi, Y., Tsuchikawa, T., Matsubara, N. & Horikoshi, T. 2008b. Effect of posture on the heat transfer areas of the human body. *Building and Environment.* 43:1555-1565.

Kurazumi, Y., Yamamoto, Y., Yamamoto, S. & Matsubara, N. 1997. The new weighting coefficients of mean skin temperature calculating formulas in relation to the posture. 34(4):101-112.

Kurazumi, Y., Tsuchikawa, T., Yamato, Y., Kakutani, K., Matsubara, N. & Horikoshi, T. 2003. The posture and effective thermal convective area factor of the human body. *Japanese Journal of Bio-Meteorology.* 40(1):3-13.

Li, C. & Ito, K. 2014a. Numerical and experimental estimation of convective heat transfer coefficient of human body under strong forced convective flow. *Journal of Wind Engineering and Industrial Aerodynamics.* 126(0):107-117. DOI:http://dx.doi.org/10.1016/j.jweia.2014.01.003.

Li, C. & Ito, K. 2014b. Numerical and experimental estimation of convective heat transfer coefficient of human body under strong forced convective flow. *Journal of Wind Engineering and Industrial Aerodynamics.* 126(0):107-117. DOI:http://dx.doi.org/10.1016/j.jweia.2014.01.003.

Menter, F.R., Kuntz, M. & Langtry, R. 2003. Ten Years of Industrial Experience with the SST Turbulence Model. *Turbulence, Heat and Mass Transfer.* 4:625-626,627,628,629,630,631,632,633,634,635.

Menter, R.F. 1993. *Zonal Two Equation k-w Turbulence Models for Aerodynamic Flows.* (AIAA 93-2906). Orlando, Florida: American Institute of Aeronautics and Astronautics.

Murakami, S., Kato, S. & Zeng, J. 1997. Flow and temperature fields' around human body with various room air distribution, Part 1 - . CFD study on computational thermal manikin: part 1. *ASHRAE Transactions.103 (1).* :1-3,4,5,6,7,8,9,1,11,12,13,14,15.

Nielsen, M. & Pedersen, L. 1952. Studies on the Heat Loss by Radiation and Convection from the Clothed Human Body. *Acta Physiologica Scandanavia.* 27:272-294.

Nishi, Y. & Gagge, A., P. 1970. Direct evaluation of convective heat transfer coefficient by naphthalene sublimation. *Journal of Applied Physiology.* 29(6):830-838.

Oguro, M., Arens, E., de Dear, R., Zhang, H. & Katayama, T. 2002. Convective heat transfer coefficients and clothing insulations for parts of the clothed human body under calm conditions. *Journal of Architecture, Planning and Environment.* 561:31-39.

Quintela, D., Gaspar, A. & Borges, C. 2004. Analysis of sensible heat exchanges from a thermal manikin. *Journal of Applied Physiology.* 92:663-668.

Spalart, P.R. & Allmaras, R.S. 1992. *A One-Equation Turbulence Model for Aerodynamic Flows.* (AIAA-92-0439). Washington, D.C. 20024: American Institute of Aeronautics and Astronautics.

Tannehill, J.C., Anderson, D.A. & Pletcher, R.H. 1997. *Computational Fluid Mechanics and Heat Transfer.* 2nd ed. United States of America: Hemisphere Publishing Corporation.

Versteeg, H.K. & Malalasekera, W. 1995. Computational Fluid Dynamics, Finite Volume Method. New York: John Wiley & Sons Inc.

Versteeg, H.K. & Malalasekera, W. 2007. *An Introduction to Computational Fluid Dynamics: The finite Volume Method.* 2nd Edition ed. England: Pearson, Prentice hall.

Virgilio, A., Oliveira, M., Gaspar, A., Francisco, S. & Quintela, D. 2012. Convective heat transfer from a nude body under calm conditions: assessment of the effects of walking with a thermal manikin. *Int J Biometeorol.* 56:319-332. DOI: 10.1007/s00484-011-0436-3.

Virgilio, A., Oliveira, M., Gaspar, A., Francisco, S. & Quintela, D. 2014. Analysis of natural and forced convection heat losses from a thermal manikin: Comparative assessment of the staits dynamic postures. *Journal of Wind Engineering and Industrial Aerodynamics.* 132:66-76.

Winslow, C.E.A., Herrington, L.P. & Gagge, A., P. 1936. The Determination of Radiation and Convection Exchanges by Partitional Calorimetry. *American Journal of Physiology.* 116(3):669-84.

EDITORIAL, 1994, Journal of Heat Transfer Editorial Policy Statement on Numerical Accuracy, ASME J. Heat Transfer, 116, pp. 797–798;

9 APPENDIX A0 – CONVECTION EQUATION DESCRITIZATION

Equation 3.16 from Chapter 3, Section 3.8 is repeated here (equation 9.1), and discretised step by step.

$$-\frac{\partial}{\partial x}(u_x T)|_C \approx \frac{u_x}{l_v}\left[T|_{f_L} + T|_{f_R}\right] \tag{9.1}$$

Where:

$$T|_{f_L} = T|_u + [W_1(T_C - T_u) + W_2(T_u - T_{uu}{}^*)]$$

But

$$T_{uu}{}^* \approx T_c - 2\frac{\partial T}{\partial x}|_U(x_c - x_u)$$

$$= T_C - 2\left[\frac{T_C - T_{uu}}{x_c - x_{uu}}\right](x_c - x_u)$$

$$\therefore T|_{f_L} = T_u + W_1T_C - W_1T_u + W_2T_u - W_2\left[T_C - 2\frac{T_c - T_{uu}}{x_c - x_{uu}}\right](x_c - x_u) \tag{9.2}$$

Also, on the other side,

$$T|_{f_R} = T_c + [W_1(V - T_c) + W_2(T_c - T_u{}^*)]$$

Similarly,

$$T_u{}^* \approx T_D - 2\frac{\partial T}{\partial x}|_C(x_D - x_c)$$

$$= T_D - 2\left[\frac{T_D - T_u}{x_D - x_u}\right](x_D - x_c)$$

$$\therefore T|_{f_R} = T_c + W_1T_D - W_1T_c + W_2T_c - W_2\left[T_D - 2\frac{T_D - T_u}{x_D - x_u}\right](x_D - x_c) \tag{9.3}$$

Substituting the equations 9.2 and 9.3 back into equation 9.1, the discretized convective term thus becomes;

$$\therefore -\frac{\partial}{\partial x}(u_x T)|_C = \frac{u_x}{l_v}\left[T_u + W_1T_C - W_1T_u + W_2T_u - W_2T_C + 2W_2\Delta x_L\left[\frac{T_c - T_{uu}}{x_c - x_{uu}}\right]\right]$$

$$+$$

$$\frac{u_x}{l_v}\left[-T_c - W_1T_D + W_1T_c - W_2T_c + W_2T_D - 2W_2\Delta x_R\left[\frac{T_D - T_u}{x_D - x_u}\right]\right]$$

The above equation cannot be applied to the 2^{nd} node of the mesh. For the second node, the gradient at Node 1 $\left(\frac{\partial T}{\partial x}|_1\right)$ is needed to compute "$T^*{}_{uu}$". We do this by allowing the left face of the control volume of node 1 to be equal to the position of node 1. This then allows computation of the gradient at node 1 as follows;

$$\frac{\partial T}{\partial x}|_1 = \frac{A}{V_1}\left[-T_L + \frac{T_L + T_R}{2}\right]$$
$$\approx \frac{2}{x_2 - x_1}\left[-T_1 + \frac{T_2 + T_1}{2}\right]$$
$$\approx \frac{T_2 - T_1}{x_2 - x_1}$$

Thus;

$$T_{uu}{}^*|_2 \approx T_1 - 2\frac{\partial T}{\partial x}|_U(x_c - x_u)$$
$$\approx T_2 - 2\frac{T_2 - T_1}{x_2 - x_1}(x_2 - x_1)$$
$$\approx 2T_1 - T_2$$
$$2T_c - T_u$$

Thus, a node 2;

$$\therefore -\frac{\partial}{\partial x}(u_x T)|_C = \frac{u_x}{l_v}\left[T_u + W_1 T_C - W_1 T_u + W_2 T_u + W_2 T_u - W_2[2T_c - T_u]\right]$$
$$+$$
$$\frac{u_x}{l_v}\left[-T_c - W_1 T_D + W_1 T_c - W_2 T_c + W_2 T_D - 2W_2 \Delta x_R\left[\frac{T_D - T_u}{x_D - x_u}\right]\right]$$

The combined discretized governing equation for node 3 to 'N-1' is thus;

$$-\frac{\partial u_x T}{\partial x} + \frac{\partial}{\partial x}\left(k\frac{\partial T}{\partial x}\right) = \frac{u_x}{l_v}\left[T_u + W_1 T_C - W_1 T_u + W_2 T_u - W_2 T_C + 2W_2 \Delta x_L\left[\frac{T_c - T_{uu}}{x_c - x_{uu}}\right]\right]$$
$$+$$

$$\frac{u_x}{l_v}\Big[-T_c - W_1T_D + W_1T_c - W_2T_c + W_2T_D - 2W_2\Delta x_R\left[\frac{T_D - T_u}{x_D - x_u}\right]\Big] + \frac{k}{l_v}\left[\frac{1}{\Delta x_L}T_u + \frac{1}{\Delta x_R}T_D - \left(\frac{1}{\Delta x_R} - \frac{1}{\Delta x_R}\right)T_c\right]$$

While for node 2 we have;

$$-\frac{\partial u_x T}{\partial x} + \frac{\partial}{\partial x}\left(k\frac{\partial T}{\partial x}\right) = \frac{u_x}{l_v}\left[T_u + W_1T_C - W_1T_u + W_2T_u + W_2T_u - W_2[2T_c - T_u]\right] + \frac{u_x}{l_v}\Big[-T_c - W_1T_D + W_1T_c - W_2T_c + W_2T_D - 2W_2\Delta x_R\left[\frac{T_D - T_u}{x_D - x_u}\right]\Big] + \frac{k}{l_v}\left[\frac{1}{\Delta x_L}T_u + \frac{1}{\Delta x_R}T_D - \left(\frac{1}{\Delta x_R} - \frac{1}{\Delta x_R}\right)T_c\right]$$

10 APPENDIX A1 – MATLAB CODE USED FOR FIRST ORDER UPWINDING

Equispaced

```
%% 1D Diffusion Convection Equation Using the Upwind Method
%
%  Published By: Daniel Eferemo
%  Student Number: EFRDAN001
%  Mesh Type: Equispaced

%% clear workspace
clc
clear

%% Define variables
N = 1000;

Error_max = zeros(N-1,1);
Node = zeros(N-1,1);
dx_vec = zeros(N,1);

for N = 20 : 1000;

ux = 2.5;
k = 0.2;
x0 = 0;
x1 = 1;
L = x1 - x0;

%% Boundary Conditions
```

```
T0 = 1;
T1 = 0;
dT = T1 - T0;
x = linspace(x0,x1,N);

%% Analytical Solution

a = (x * ux) / k;
v = (L * ux) / k;

T_anal = (dT * ((exp(a) - 1)/(exp(v) - 1))) + T0;


%% Describing the equi - spaced mesh

dx_vec(1) = 0;

dx = (x1 - x0) / (N - 1);

for j = 2:N
    dx_vec(j) = (x1 - x0) / (j - 1);
end

log_dx = log10(dx_vec);



%% Creating the Matrix for the Equi-spaced Mesh

A = zeros(N,N);
b = zeros(N,1);

A(1,1) = 1.0;
b(1) = T0;
```

```
for i = 2 : N - 1

    l_v = (x(i+1) - x(i-1))/2;                          %length of control volume

    dx_L = x(i) - x(i-1);

    dx_R = x(i+1) - x(i);


    A(i,i) =   (-ux/l_v) - ((k/l_v)*((1/dx_L) + (1/dx_R)));       %Matrix diagonals

    A(i,i-1) =  (ux/l_v) + (k/l_v/dx_L);       %Left of Matrix Diagonals

    A(i,i+1) =            + (k/l_v/dx_R);      %Right of Matrix Diagonals
    b(i) = 0.0;
end

A(N,N) = 1.0;
b(N) = T1;
T = A \ b;

%% Percentage Error per Node for the Equi-Spaced Mesh

Error = zeros(N,1);

Error(1) = 0.0;
Error(N) = 0.0;

for i = 2 : N - 1
    Error(i) = ((abs(T_anal(i) - T(i)))/(T_anal(i))) * 100;
end

Error_max(i) = max(Error);
log_Error = log10(Error_max);
```

```
log_Error(1) = 0;
log_Error(N) = 0;

Node(i) = N;
log_Nodes = log10(Node);

%% Absolute Nodal Error

Error_absolute = zeros(N,1);

Error(1) = 0.0;
Error_absolute(N) = 0.0;

for i = 2 : N - 1
    Error_absolute(i) = abs(T_anal(i) - T(i));
end



end
log_Nodes(N) = log10(N);

%% Determining Minimum number of nodes for Maximum Error < 1%
%
% E = 1.1;
% i = 9;
% while E > 1
%     i = i + 1;
%     E = Error_max(i);
% end
%
% fprintf(1, ' Maximum Nodal Error E = %d\n', E);
% fprintf(1, ' At node  = %d\n', i);
% fprintf(1, ' Thus, Minimum number of node to have maximum error < 1 percent is %d\n', i);


%% Plots
```

```
grid on
hold on

% subplot(2,1,1)
% plot ( x, T, 'ro', 'LineWidth', 2);
% plot ( x, T_anal, 'b-', 'LineWidth', 2 );
% ylabel('Temperature (degree celcius)')
% xlabel('Distance along Tube (m)')
% title('Graph of Temeprature Distirbution along Tube (N = 10)')
% legend('T_ Numerical','T_ analytical','Location','SouthWest')



% plot(x, Error,'r-');
% xlabel('Distance along pipe (m)')
% ylabel('% Error')
% title('%Error vs Distance Along Tube using 1000 nodes')


% subplot(2,1,2)
% plot(x(10:end), Error_absolute(10:end),'r-');
% xlabel('Distance along pipe (m)')
% ylabel('Absolute Error')
% title('Absolute Error vs Distance Along Tube (100 Nodes)')


% plot(log_Nodes(10:end),log_Error(10:end),  'co');
% xlabel('Log(number of Nodes Used)')
% ylabel('Log(max error)')
% title('Log Graph of Max Error Vs Number of Nodes Used')



% plot(log_dx,log_Error,  'r-');
% xlabel('Log(Mesh Spacing)')
% ylabel('Log(Error)')
% title('Log Graph of Max Nodal Error Vs Mesh Spacing "Dx"')
```

Stretched

```
%% 1D Diffusion Convection Equation Using the Upwind Method
%
%
%  Published By: Daniel Eferemo
%  Student Number: EFRDAN001
%  Mesh Type: Stretched

%% clear workspace
clc
clear

%% Define variables
N = 87;

beta = 0.95;

Error_max = zeros(N-1,1);
Node = zeros(N-1,1);

for N = 20 : 87;


ux = 2.5;
k = 0.2;
x0 = 0;
x1 = 1;
L = 1.0;

%% Boundary Conditions

T0 = 1;
T1 = 0;
dT = T1 - T0;
```

```
% x = linspace(x0,x1,N);           % different for a stretched mesh. NOTE!!

%% Creating the Stretched Mesh
%
sum_beta = 1.0;

for i = 1 : N - 2
    sum_beta = sum_beta + (beta^i);
end

dx_stretched = L /sum_beta;

%% Spacing the stretched mesh into N nodes

x_stretched  = zeros(N,1);

x_stretched(1) = x0;

for i = 2 : N-1
    x_stretched(i) = x_stretched(i-1) + (dx_stretched * (beta^(i - 2)));
end

x_stretched(N) = x1;

dx_stretched_vector = zeros(N-1,1);
dx_stretched_vector(N) = 0;

for i = 1 : N - 1

    dx_stretched_vector(i) = x_stretched(i+1) - x_stretched(i);

end

log_dx_stretched = log(dx_stretched_vector);
%% Analytical Solution
```

```
a = (x_stretched * ux) / k;
v = (L * ux) / k;

T_anal = (dT * ((exp(a) - 1)/(exp(v) - 1))) + T0;

%% Creating the Matrix for the Stretched Mesh

A_stretched = zeros(N,N);
b = zeros(N,1);

A_stretched(1,1) = 1.0;
b(1) = T0;


for i = 2 : N - 1

    l_v = (x_stretched(i+1) - x_stretched(i-1))/2;                          %length of control volume

    dx_L = x_stretched(i) - x_stretched(i-1);

    dx_R = x_stretched(i+1) - x_stretched(i);



    A_stretched(i,i) =  (-ux/l_v) - ((k/l_v)*((1/dx_L) + (1/dx_R)));       %Matrix diagonals

    A_stretched(i,i-1) = (ux/l_v) + (k/l_v/dx_L);                          %Left of Matrix Diagonals

    A_stretched(i,i+1) =            (k/l_v/dx_R);                          %Right of Matrix Diagonals

    b(i) = 0.0;

end

A_stretched(N,N) = 1.0;
```

```
b(N) = T1;
T_stretched = A_stretched \ b;

%% Percentage Error per Node for the Stretched Mesh

Error = zeros(N,1);

Error(1) = 0.0;
Error(N) = 0.0;

for i = 2 : N - 1
    Error(i) = ((abs(T_anal(i) - T_stretched(i)))/(T_anal(i))) * 100;
end

Error_max(N) = max(Error);
log_Error = log10(Error_max);

Node(N) = N;
log_Nodes = log10(Node);

%% Absolute Nodal Error

Error_absolute = zeros(N,1);

Error_absolute(1) = 0.0;
Error_absolute(N) = 0.0;

for i = 2 : N - 1
    Error_absolute(i) = abs(T_anal(i) - T_stretched(i));
end


end

Error_max(1) = 0;
Error_max(N+1) = 0;
```

```
%% Determining Minimum number of nodes for Maximum Error < 1%

E = 1.1;
i = 9;
while E > 1
    i = i + 1;
    E = Error_max(i);
end

fprintf(1, ' Maximum Error E = %d\n', E);
fprintf(1, ' At node  = %d\n', i);
fprintf(1, ' Thus, Minimum number of node to have maximum error < 1 percent is %d\n', i);

%% Plots

grid on
hold on
%
% plot ( x_stretched, T_stretched, 'go', 'LineWidth', 2, 'Markersize', 10 );
% plot ( x_stretched, T_anal, 'b-', 'LineWidth', 2 );
% ylabel('Temperature (degree celcius)')
% xlabel('Distance along Tube (m)')
% title('Graph of Temeprature Distribution along Tube (N = 100)')
% legend('T_ Numerical','T_ analytical','Location','SouthWest')

% %
% plot(x_stretched, Error,'r-');
% xlabel('Distance along pipe (m)')
% ylabel('% Error')
% title('%Error vs Distance Along Tube for a Stretched Mesh with "beta" = 0.9, N = 100')

% plot(x_stretched, Error_absolute,'r-');
% xlabel('Distance along pipe (m)')
% ylabel('Absolute Error')
% title('Absolute Error Distribution along Tube (ß = 0.95, N = 100)')
```

```
plot(log_dx_stretched,log_Error,  'r-');
xlabel('Log(Mesh Spacing)')
ylabel('Log(Max error)')
title('Log Graph of Max Nodal Error Vs Mesh Spacing "Dx"')
```

11 APPENDIX A2 – MATLAB CODE USED FOR HIGHER ORDER UPWINDING

Equispaced and Stretched

```
%% 1D Diffusion Convection Equation Using Higher Upwind Methods
%
%  Published By: Daniel Eferemo
%  Student Number: EFRDAN001
%  Mesh Type: Equi-Spaced and Stretched
%  Set "beta" = 1 for an equispaced mesh
%  Set "kappa" = 1,1/2 or 1/3 for Central Difference Scheme, QUICK Scheme
%  or CUI Scheme respectively
%
%  Set "W_1" and "W_2" = 0 for first order upwind analysis if required

%% clear workspace
clc
clear

%% Define variables
M = 100;
kappa = 1/3;
beta = 0.85;

W_1 = (1+kappa)/4;
W_2 = (1-kappa)/4;

% W_1 = 0;
% W_2 = 0;
```

```
Error_max = zeros(M-1,1);
Node = zeros(M-1,1);
Error_max_abs = zeros(M-1, 1);
dx_stretched_vector = zeros(M-1,1);

for N = 3 : 30;


ux = 2.5;
k = 0.2;
x0 = 0;
x1 = 1;
L = 1.0;

%% Boundary Conditions

T0 = 1;
T1 = 0;
dT = T1 - T0;

%% Creating the Mesh and Spacing the Mesh into N nodes
%
sum_beta = 1.0;

for i = 1 : N - 2
    sum_beta = sum_beta + (beta^i);
end

dx_stretched = L /sum_beta;

x_stretched  = zeros(N,1);
x_stretched(1) = x0;
for i = 2 : N-1
    x_stretched(i) = x_stretched(i-1) + (dx_stretched * (beta^(i - 2)));
end
x_stretched(N) = x1;
```

```
dx_stretched_vector(i) = x_stretched(i+1) - x_stretched(i);

dx_stretched_vector(N) = 0;


%% Analytical Solution

a = (x_stretched * ux) / k;
v = (L * ux) / k;

T_anal = (dT * ((exp(a) - 1)/(exp(v) - 1))) + T0;

%% Creating the Matrix for the Mesh

A_stretched = zeros(N,N);
b = zeros(N,1);

A_stretched(1,1) = 1.0;
b(1) = T0;


x_U = x_stretched(1);
x_C = x_stretched(2);
x_D = x_stretched(3);

l_v = (x_D - x_U) / 2;
dx_L = x_C - x_U;
dx_R = x_D - x_C;

A_stretched(2,1) =   (((ux/l_v)) * (1 - W_1 - W_2 + ((2*W_2*dx_R)/(x_D - x_U)) ))        + ((k/l_v)*(1/dx_L));

A_stretched(2,2) =   ((ux/l_v) * ((2*W_1) - 1))                                    - ((k/l_v)*((1/dx_L) + (1/dx_R)));

A_stretched(2,3) =   ((ux/l_v) * (W_2 - W_1 - ((2*W_2*dx_R)/(x_D - x_U))))                 + ((k/l_v)*(1/dx_R));
```

```
for i = 3 : N - 1

    x_UU = x_stretched(i - 2);
    x_U = x_stretched(i - 1);
    x_C = x_stretched(i);
    x_D = x_stretched(i + 1);

    l_v = (x_D - x_U) / 2;
    dx_L = x_C - x_U;
    dx_R = x_D - x_C;

    A_stretched(i,i - 2) =   (-((2*W_2*dx_L)/(x_C - x_UU)) * (ux/l_v));

    A_stretched(i,i - 1) =   (((ux/l_v)) * (1 - W_1 + W_2 + ((2*W_2*dx_R)/(x_D - x_U))))  + ((k/l_v)*(1/dx_L));

    A_stretched(i,i) =   ((ux/l_v) * (W_1 - W_2 + ((2*W_2*dx_L)/(x_C - x_UU)) - 1 + W_1 - W_2))  - ((k/l_v)*((1/dx_L)
+ (1/dx_R)));

    A_stretched(i, i + 1) =     ((ux/l_v) * (W_2 - W_1 - ((2*W_2*dx_R)/(x_D - x_U))))     + ((k/l_v)*(1/dx_R));

    b(i) = 0.0;

end

A_stretched(N,N) = 1.0;
b(N) = T1;
T_stretched = A_stretched \ b;

%% Percentage Error per Node for the Mesh

Error = zeros(N,1);

Error(1) = 0.0;
Error(N) = 0.0;

for i = 2 : N - 1
```

```
    Error(i) = ((abs(T_anal(i) - T_stretched(i)))/(T_anal(i))) * 100;
end

Error_max(N) = max(Error);
log_Error = log10(Error_max);

Node(N) = N;

%% Absolute Nodal Error

Error_absolute = zeros(N,1);

Error_absolute(1) = 0.0;
Error_absolute(N) = 0.0;

for i = 2 : N - 1
    Error_absolute(i,1) = abs(T_anal(i) - T_stretched(i));
end


Error_max_abs(N,1) = max(Error_absolute);

end %end of major for loop

log_Nodes = log10(Node);
log_Error_abs = log10(Error_max_abs);
log_dx_stretched = log(dx_stretched_vector);


Error_max(1,1) = 0;
Error_max(N+1) = 0;

%% Determining Minimum number of nodes for Maximum Error < 1%

E = 1.1;  %random integer to initiate while loop
i = 5;
```

```
while E > 1
    i = i + 1;
    E = Error_max(i);
end

fprintf(1, ' Maximum Error E = %d\n', E);
fprintf(1, ' At node  = %d\n', i);
fprintf(1, ' Thus, Minimum number of node to have maximum error < 1 percent is %d\n', i);


%% Plots

grid on
hold on

% plot(x,T,'ro');
% plot(x,T_anal);

% subplot(2,1,1)
% hold on
plot ( x_stretched, T_stretched, 'ro', 'LineWidth', 1);
plot ( x_stretched, T_anal, 'b-', 'LineWidth', 1 );
ylabel('Temperature (degree celcius)')
xlabel('Distance along Tube (m)')
title('Graph of Temeprature Distirbution along Tube (N = 6, kappa = 1/3 beta = 0.85)')
legend('T_ Numerical','T_ analytical','Location','SouthWest')

% subplot(2,1,2)
% plot(x_stretched, Error_absolute,'r-');
% xlabel('Distance along pipe (m)')
% ylabel('Absolute Error')
% title('Absolute Error vs Distance Along Tube (N = 10, kappa = 1/3, beta = 1)')

% plot(log_dx_stretched,log_Error_abs,  'r-');
% xlabel('Log(Mesh Spacing)')
% ylabel('Log(Max error)')
% title('Log Graph of Max Nodal Error Vs Mesh Spacing "Dx" (kappa = 1/2, beta = 0.85)')
```

12 APPENDIX B1 – RESULTS OF CFD SIMULATIONS FOR THE UPRIGHT CYLINDER – TURBULENT FLOW

TI = 2 %						
Wind velocity	k	w	Total Surface Heat Flux average	Radiative Heat Flux	Convective Heat Flux	Convective Heat Transfer Co-Eff
2	0.0024	0.001469694	27.63	18.43158404	9.198415961	3.066138654
4	0.0096	0.002939388	42.46	18.43158404	24.02841596	8.009471987
6	0.0216	0.004409082	57.35	18.43158404	38.91841596	12.97280532
8	0.0384	0.005878775	70.53	18.43158404	52.09841596	17.36613865
10	0.06	0.007348469	83.53	18.43158404	65.09841596	21.69947199
12	0.0864	0.008818163	95	18.43158404	76.56841596	25.52280532

TI = 4 %						
Wind velocity	k	w	Total Surface Heat Flux average	Radiative Heat Flux	Convective Heat Flux	Convective Heat Transfer Co-Eff
2	0.0096	0.00293939	30.8	18.43158404	12.36841596	4.12280532
4	0.0384	0.00587878	48.66	18.43158404	30.22841596	10.07613865
6	0.0864	0.00881816	67.23	18.43158404	48.79841596	16.26613865
8	0.1536	0.01175755	84.27	18.43158404	65.83841596	21.94613865
10	0.24	0.01469694	100.4	18.43158404	81.96841596	27.32280532
12	0.3456	0.01763633	116.6	18.43158404	98.16841596	32.72280532

TI = 6 %						
Wind velocity	k	w	Total Surface Heat Flux average	Radiative Heat Flux	Convective Heat Flux	Convective Heat Transfer Co-Eff
2	0.0216	0.004409082	32.68	18.43158404	14.24841596	4.749471987
4	0.0864	0.008818163	55.82	18.43158404	37.38841596	12.46280532
6	0.1944	0.013227245	77.85	18.43158404	59.41841596	19.80613865
8	0.3456	0.017636326	98.23	18.43158404	79.79841596	26.59947199
10	0.54	0.022045408	118.16	18.43158404	99.72841596	33.24280532
12	0.7776	0.026454489	137.48	18.43158404	119.048416	39.68280532

TI = 8 %						
Wind velocity	k	w	Total Surface Heat Flux average	Radiative Heat Flux	Convective Heat Flux	Convective Heat Transfer Co-Eff
2	0.0384	0.00587878	35.85	18.43158404	17.41841596	5.806138654
4	0.1536	0.01175755	62.52	18.43158404	44.08841596	14.69613865
6	0.3456	0.01763633	88.2	18.43158404	69.76841596	23.25613865
8	0.6144	0.0235151	111.92	18.43158404	93.48841596	31.16280532
10	0.96	0.02939388	136.99	18.43158404	118.558416	39.51947199
12	1.3824	0.03527265	157.6	18.43158404	139.168416	46.38947199

TI = 10 %						
Wind velocity	k	w	Total Surface Heat Flux average	Radiative Heat Flux	Convective Heat Flux	Convective Heat Transfer Co-Eff
2	0.06	0.007348469	39.57	18.43158404	21.13841596	7.046138654
4	0.24	0.014696938	69.26	18.43158404	50.82841596	16.94280532
6	0.54	0.022045408	97.74	18.43158404	79.30841596	26.43613865
8	0.96	0.029393877	124.52	18.43158404	106.088416	35.36280532
10	1.5	0.036742346	150.5	18.43158404	132.068416	44.02280532
12	2.16	0.044090815	175.63	18.43158404	157.198416	52.39947199

13 APPENDIX B2 – RESULTS OF CFD SIMULATIONS FOR THE INCLINED CYLINDER (45 DEGREE TO THE VERTICAL) – TURBULENT FLOW

TI = 2 %						
Wind velocity	k	w	Total Surface Heat Flux average	Radiative Heat Flux	Convective Heat Flux	Convective Heat Transfer Co-Eff
2	0.0024	0.001469694	25.76	18.43158404	7.328415961	2.44280532
4	0.0096	0.002939388	40.55	18.43158404	22.11841596	7.37280532
6	0.0216	0.004409082	53.83	18.43158404	35.39841596	11.79947199
8	0.0384	0.005878775	66.49	18.43158404	48.05841596	16.01947199
10	0.06	0.007348469	78.31	18.43158404	59.87841596	19.95947199
12	0.0864	0.008818163	90.05	18.43158404	71.61841596	23.87280532

TI = 4 %						
Wind velocity	k	w	Total Surface Heat Flux average	Radiative Heat Flux	Convective Heat Flux	Convective Heat Transfer Co-Eff
2	0.0096	0.00293939	28.4	18.43158404	9.968415961	3.32280532
4	0.0384	0.00587878	46.38	18.43158404	27.94841596	9.316138654
6	0.0864	0.00881816	63.62	18.43158404	45.18841596	15.06280532
8	0.1536	0.01175755	79.36	18.43158404	60.92841596	20.30947199
10	0.24	0.01469694	94.92	18.43158404	76.48841596	25.49613865
12	0.3456	0.01763633	110.17	18.43158404	91.73841596	30.57947199

TI = 6 %						
Wind velocity	k	w	Total Surface Heat Flux average	Radiative Heat Flux	Convective Heat Flux	Convective Heat Transfer Co-Eff
2	0.0216	0.004409082	30.99	18.43158404	12.55841596	4.186138654
4	0.0864	0.008818163	53.14	18.43158404	34.70841596	11.56947199
6	0.1944	0.013227245	73.26	18.43158404	54.82841596	18.27613865
8	0.3456	0.017636326	92.84	18.43158404	74.40841596	24.80280532
10	0.54	0.022045408	112.16	18.43158404	93.72841596	31.24280532
12	0.7776	0.026454489	130.41	18.43158404	111.978416	37.32613865

TI = 8 %						
Wind velocity	k	w	Total Surface Heat Flux average	Radiative Heat Flux	Convective Heat Flux	Convective Heat Transfer Co-Eff
2	0.0384	0.00587878	34.08	18.43158404	15.64841596	5.216138654
4	0.1536	0.01175755	59.37	18.43158404	40.93841596	13.64613865
6	0.3456	0.01763633	82.55	18.43158404	64.11841596	21.37280532
8	0.6144	0.0235151	105.77	18.43158404	87.33841596	29.11280532
10	0.96	0.02939388	127.44	18.43158404	109.008416	36.33613865
12	1.3824	0.03527265	149.01	18.43158404	130.578416	43.52613865

TI = 10 %						
Wind velocity	k	w	Total Surface Heat Flux average	Radiative Heat Flux	Convective Heat Flux	Convective Heat Transfer Co-Eff
2	0.06	0.007348469	37.09	18.43158404	18.65841596	6.219471987
4	0.24	0.014696938	65.26	18.43158404	46.82841596	15.60947199
6	0.54	0.022045408	92.04	18.43158404	73.60841596	24.53613865
8	0.96	0.029393877	117.11	18.43158404	98.67841596	32.89280532
10	1.5	0.036742346	141.94	18.43158404	123.508416	41.16947199
12	2.16	0.044090815	165.83	18.43158404	147.398416	49.13280532

14 APPENDIX B3 – RESULTS OF CFD SIMULATIONS FOR THE SUPINE CYLINDER – TURBULENT FLOW

TI = 2 %						
Wind velocity	k	w	Total Surface Heat Flux average	Radiative Heat Flux	Convective Heat Flux	Convective Heat Transfer Co-Eff
2	0.0024	0.001469694	26.86	18.43158404	8.428415961	2.809471987
4	0.0096	0.002939388	46.21	18.43158404	27.77841596	9.259471987
6	0.0216	0.004409082	65.23	18.43158404	46.79841596	15.59947199
8	0.0384	0.005878775	83.51	18.43158404	65.07841596	21.69280532
10	0.06	0.007348469	101.71	18.43158404	83.27841596	27.75947199
12	0.0864	0.008818163	118.88	18.43158404	100.448416	33.48280532

TI = 4 %						
Wind velocity	k	w	Total Surface Heat Flux average	Radiative Heat Flux	Convective Heat Flux	Convective Heat Transfer Co-Eff
2	0.0096	0.00293939	28.22	18.43158404	9.788415961	3.26280532
4	0.0384	0.00587878	48.01	18.43158404	29.57841596	9.859471987
6	0.0864	0.00881816	67.53	18.43158404	49.09841596	16.36613865
8	0.1536	0.01175755	86.21	18.43158404	67.77841596	22.59280532
10	0.24	0.01469694	105.07	18.43158404	86.63841596	28.87947199
12	0.3456	0.01763633	123.2	18.43158404	104.768416	34.92280532

TI = 6 %						
Wind velocity	k	w	Total Surface Heat Flux average	Radiative Heat Flux	Convective Heat Flux	Convective Heat Transfer Co-Eff
2	0.0216	0.004409082	30.62	18.43158404	12.18841596	4.06280532
4	0.0864	0.008818163	50.93	18.43158404	32.49841596	10.83280532
6	0.1944	0.013227245	70.62	18.43158404	52.18841596	17.39613865
8	0.3456	0.017636326	90.09	18.43158404	71.65841596	23.88613865
10	0.54	0.022045408	109.41	18.43158404	90.97841596	30.32613865
12	0.7776	0.026454489	127.94	18.43158404	109.508416	36.50280532

TI = 8 %						
Wind velocity	k	w	Total Surface Heat Flux average	Radiative Heat Flux	Convective Heat Flux	Convective Heat Transfer Co-Eff
2	0.0384	0.00587878	31.31	18.43158404	12.87841596	4.29280532
4	0.1536	0.01175755	53.47	18.43158404	35.03841596	11.67947199
6	0.3456	0.01763633	72.72	18.43158404	54.28841596	18.09613865
8	0.6144	0.0235151	94.93	18.43158404	76.49841596	25.49947199
10	0.96	0.02939388	114.59	18.43158404	96.15841596	32.05280532
12	1.3824	0.03527265	134.28	18.43158404	115.848416	38.61613865

TI = 10 %						
Wind velocity	k	w	Total Surface Heat Flux average	Radiative Heat Flux	Convective Heat Flux	Convective Heat Transfer Co-Eff
2	0.06	0.007348469	38.61	18.43158404	20.17841596	6.726138654
4	0.24	0.014696938	53.89	18.43158404	35.45841596	11.81947199
6	0.54	0.022045408	76.29	18.43158404	57.85841596	19.28613865
8	0.96	0.029393877	97.29	18.43158404	78.85841596	26.28613865
10	1.5	0.036742346	120.67	18.43158404	102.238416	34.07947199
12	2.16	0.044090815	140.89	18.43158404	122.458416	40.81947199

15 APPENDIX C1 – RESULTS OF CFD SIMULATIONS FOR LAMINAR FLOW

Upright Cylinder					
Cylinder Temperature (K)	Temperature Difference	Total Surface Heat Flux_average	Radiative Heat Flux_average	Convective Heat Flux	Convective Heat Transfer Co-Eff
291	4	46.3	35.08	11.22	2.81
295	8	79.25	58.86	20.39	2.55
299	12	112.72	84.21	28.51	2.38
303	16	144.21	108.52	35.69	2.23
307	20	173.79	132.93	40.86	2.04

Inclined Cylinder					
Cylinder Temperature (K)	Temperature Difference	Total Surface Heat Flux_average	Radiative Heat Flux_average	Convective Heat Flux	Convective Heat Transfer Co-Eff
291	4	47.3	36.56	10.74	2.69
295	8	79.36	59.33	20.03	2.50
299	12	111.25	84.11	27.14	2.26
303	16	141.03	107.68	33.35	2.08
307	20	171.32	132.12	39.2	1.96

Supine Cylinder					
Cylinder Temperature (K)	Temperature Difference	Total Surface Heat Flux_average	Radiative Heat Flux_average	Convective Heat Flux	Convective Heat Transfer Co-Eff
291	4	47.05	36.1	10.95	2.74
295	8	76.02	56.86	19.16	2.40
299	12	106.6	80.56	26.04	2.17
303	16	138.36	105.28	33.08	2.07
307	20	169.87	130.87	39	1.95

16 ETHICS FORM

EBE Faculty: Assessment of Ethics in Research Projects (Rev2)

Any person planning to undertake research in the Faculty of Engineering and the Built Environment at the University of Cape Town is required to complete this form before collecting or analysing data. When completed it should be submitted to the supervisor (where applicable) and from there to the Head of Department. If any of the questions below have been answered YES, and the applicant is NOT a fourth year student, the Head should forward this form for approval by the Faculty EIR committee: submit to Ms Zulpha Geyer (Zulpha.Geyer@uct.ac.za; Chem Eng Building, Ph 021 650 4791).
NB: A copy of this signed form must be included with the thesis/dissertation/report when it is submitted for examination

This form must only be completed once the most recent revision EBE EiR Handbook has been read.

Name of Principal Researcher/Student: Daniel Eferemo Department: Mechanical Engineering

Preferred email address of the applicant: danieleferemo@yahoo.com

If a Student: Degree: M.Sc. Mechanical Engineering Supervisor: Prof. Tunde Bello-Ochende

If a Research Contract indicate source of funding/sponsorship:

Research Project Title:
Numerical Investigation of the Convective Heat Transfer Coefficient of the Human Body Using a Representative Cylindrical Model.

Overview of ethics issues in your research project:

Question 1: Is there a possibility that your research could cause harm to a third party (i.e. a person not involved in your project)?	YES	(NO)
Question 2: Is your research making use of human subjects as sources of data? If your answer is YES, please complete Addendum 2.	YES	(NO)
Question 3: Does your research involve the participation of or provision of services to communities? If your answer is YES, please complete Addendum 3.	YES	(NO)
Question 4: If your research is sponsored, is there any potential for conflicts of interest? If your answer is YES, please complete Addendum 4.	YES	(NO)

If you have answered YES to any of the above questions, please append a copy of your research proposal, as well as any interview schedules or questionnaires (Addendum 1) and please complete further addenda as appropriate. Ensure that you refer to the EiR Handbook to assist you in completing the documentation requirements for this form.

I hereby undertake to carry out my research in such a way that

- there is no apparent legal objection to the nature or the method of research; and
- the research will not compromise staff or students or the other responsibilities of the University;
- the stated objective will be achieved, and the findings will have a high degree of validity;
- limitations and alternative interpretations will be considered;
- the findings could be subject to peer review and publicly available; and
- I will comply with the conventions of copyright and avoid any practice that would constitute plagiarism.

Signed by:

	Full name and signature	Date
Principal Researcher/Student:	Daniel Eferemo signature removed	5/5/2017
This application is approved by:		
Supervisor (if applicable):	Prof. Tunde Bello-Ochende signature removed	5/5/2017
HOD (or delegated nominee): *Final authority for all assessments with NO to all questions and for all undergraduate research.*	Prof. Tunde Bello-Ochende signature removed	5/5/2017
Chair : Faculty EIR Committee For applicants other than undergraduate students who have answered YES to any of the above questions.		